# SUPEREXCHANGE-COUPLED ELECTRON-SPIN PAIRS IN IRON TETRAPHENYLPORPHINE CHLORIDE AT LOW TEMPERATURES

A Dissertation
for the Degree of Ph. D.
MICHIGAN STATE UNIVERSITY
Gary L. Neiheisel
1975

This is to certify that the

thesis entitled

Superexchange-coupled Electron-spin Pairs in Iron Tetraphenylporphine Chloride at Low Temperatures

presented by

GARY L. NEIHEISEL

has been accepted towards fulfillment
of the requirements for

Ph.D. degree in Physics

William P. Pratt Jr.

Major professor

Date June 11, 1975

ABSTRACT

SUPEREXCHANGE-COUPLED ELECTRON-SPIN PAIRS IN
IRON TETRAPHENYLPORPHYRIN CHLORIDE AT LOW TEMPERATURES

By

Gary L. Neiheisel

Iron tetraphenylporphine chloride (FeTPPCl) has a unique crystal structure which allows approximately 50% of the molecules in the crystal to form isolated superexchange pairs. The remaining 50% of the FeTPPCl molecules act as isolated paramagnetic molecules (neglecting the weak classical dipole-dipole coupling). The spin-pairing occurs in a low temperature region (0.1 K - 1.0 K). Magnetic susceptibility measurements on a small aligned single crystal of FeTPPCl have been made using a Superconducting Quantum Interference Device (SQUID) magnetometer mounted in a $^3He$-$^4He$ dilution refrigerator. The spin-lattice heat capacity of a powdered sample of FeTPPCl has also been measured using the dilution refrigerator. In addition, electron spin resonance measurements on a small aligned single crystal and on powdered samples of FeTPPCl yielded direct spin transitions between the superexchange spin energy levels. A simple highly anisotropic Heisenberg model has been shown to characterize the superexchange coupling. The theoretical results are in good agreement with the experimental data.

ABSTRACT

SUPEREXCHANGE-COUPLED ELECTRON-SPIN PAIRS IN
IRON TETRAPHENYLPORPHINE CHLORIDE AT LOW TEMPERATURES

By

Gary L. Neiheisel

Iron tetraphenylporphine chloride (FeTPPCl) has a unique crystal structure which allows approximately 50% of the molecules in the crystal to form isolated superexchange pairs. The remaining 50% of the FeTPPCl molecules act as isolated paramagnetic molecules (neglecting the weak classical dipole-dipole coupling). The spin-pairing occurs in a low temperature region (0.1 K - 1.0 K). Magnetic susceptibility measurements on a small aligned single crystal of FeTPPCl have been made using a Superconducting Quantum Interference Device (SQUID) magnetometer mounted in a $^{3}He$-$^{4}He$ dilution refrigerator. The zero-field heat capacity of a powdered sample of FeTPPCl has also been measured using the dilution refrigerator. In addition, electron spin resonance measurements on a small aligned single crystal and on powdered samples of FeTPPCl exhibit direct ESR transitions between the superexchange-split energy levels. A simple highly anisotropic Heisenberg exchange term was chosen to characterize the superexchange coupling. The theoretical results are in good agreement with the experimental data.

# SUPEREXCHANGE-COUPLED ELECTRON-SPIN PAIRS IN IRON TETRAPHENYLPORPHINE CHLORIDE AT LOW TEMPERATURES

By

Gary L. Neiheisel

A DISSERTATION

Submitted to
Michigan State University
in partial fulfillment of the requirements
for the degree

DOCTOR OF PHILOSOPHY

Department of Physics

1975

## DEDICATION

This thesis is dedicated to my wife, Carol, who braved the frozen north so that I could become a physicist, and to my parents, who encouraged me to develop my academic talents.

## ACKNOWLEDGMENTS

I would like to express my deepest gratitude to Dr. William P. Pratt, Jr. for his suggestions and encouragement in the completion of this thesis. A special thanks is owed to Dr. Jeffrey L. Imes and Paul R. Newman for their help in the collection of the experimental data. I would also like to thank Dr. Jerry A. Cowen for the use of his electron spin resonance spectrometer and for his assistance in several of the ESR runs. I am also very grateful to Dr. R. D. Spence, Dr. S. D. Mahanti, Dr. M. Barma, and Dr. T. A. Kaplan for their advice regarding various aspects of this thesis. I would also like to extend my thanks to the people in the Machine Shop and Electronics Shop for their help in the construction of the apparatus.

TABLE OF CONTENTS

LIST OF FIGURES

Figure Page

Figure Page

## LIST OF TABLES

# INTRODUCTION

The metalloporphyrins are a group of organic molecules which have been extensively studied because of their inclusion in certain biological molecules such as myoglobin, hemoglobin, chlorophyll, etc.[1] The porphyrin skeleton is a planar molecule of four pyrrole rings each contributing a nitrogen atom in a square arrangement with respect to the center of the molecule.[2] In the metalloporphyrins a metal atom is bonded to the center of the porphyrin plane. The magnetic properties associated with the unpaired spins present on this metal atom are of particular interest. Both high and low-spin metalloporphyrins containing a variety of metal atoms (e.g. Fe, Cu, Ag, Mn) are available.

Since the metalloporphyrins form large molecules, the crystal structures give rise to rather large separations between adjacent metal atoms. This magnetic dilution results in rather weak inter-molecular magnetic coupling, characteristic of a classical dipole-dipole system. A consequence of this dipolar coupling in the low-spin metalloporphyrins are their low magnetic ordering temperatures. This particular property is of current interest in the search for an ultra-low temperature thermometer in the millikelvin range to replace cerium magnesium nitrate (CMN). Also, a low ordering temperature presents the possibility of using one

of the metalloporphyrins as a refrigerant by the technique of adiabatic demagnetization for achieving very low temperatures. An interesting feature of the high-spin porphyrins is that the relatively strong classical dipolar coupling should bring about magnetic ordering in the middle temperature ranges available to a dilution refrigerator (e.g. 50 - 100 millikelvin). Susceptibility measurements might then yield valuable information on the ground state of such a dipole system. The direct hyperfine interaction of the $Cu^{2+}$ unpaired electron with the Cu nucleus in copper tetraphenylporphine (CuTPP) has been observed from magnetic susceptibility measurements in our laboratory.[3] The ultralow temperature behavior of this low-spin compound indicates that magnetic dipole-dipole coupling dominates the interaction between the $Cu^{2+}$ ions.

A possible application of the high-spin metalloporphyrins is in the study of the surface interaction with liquid $^3He$. Unusually good thermal contact between CMN and pure $^3He$ has been observed by Bishop et al.[4] This is believed to be due to magnetic coupling between the CMN unpaired electronic spins and the $^3He$ nuclear spin. The high-spin metalloporphyrins would be especially suited for this kind of study due to their large magnetic moment. Also, their large planar molecular shape causes the porphyrins to be strongly adsorbed at surfaces, thus forming rather stable films.[2]

Of particular interest to this thesis is a less obvious physical phenomenon which happens to be perfectly suited to one of the metalloporphyrin complexes. This is the isolated superexchange-coupled pair. The exchange interaction takes place only among the members of a pair of nearest-neighbor paramagnetic sites and does not allow for a similar interaction with any other neighboring sites. This type of system should be valuable from the theoretical standpoint since it allows for a first-principles calculation of the relevant exchange parameters without the added complications of long range correlations. The crystal structure of Iron ($Fe^{3+}$) Tetraphenylporphine Chloride (FeTPPCl) exhibits such properties. The unusual structure of FeTPPCl allows the formation of isolated superexchange pairs where the iron electrons couple via Fe-Cl--Cl-Fe orbital overlap along the crystalline c-axis. Approximately 50% of the high-spin $Fe^{3+}$ ions form electron-spin pairs - a significant addition to the small list of undiluted compounds in which isolated spin-pairs occur.[5] An additional factor which makes the FeTPPCl system truly unique concerns the intra-molecular crystalline electric field experienced by the unpaired iron electrons. This crystal field affects the iron 3d orbitals and the spin via the spin-orbit interaction. This gives rise to an effective crystal-field interaction term in the spin Hamiltonian which, for FeTPPCl, is much larger than the superexchange energy. At sufficiently low temperatures this large crystal-field term enables a simple

calculation of the exchange-split ground state energies.

Because of the weak superexchange coupling, the pairing takes place in a low temperature region (0.1 K - 1.0 K). A dilution refrigerator has been used in our laboratory[6] to make measurements in this low temperature region. Due to the flexible design of our machine, both the magnetic susceptibility and the heat capacity of the FeTPPCl system have been measured. A Superconducting Quantum Interference Device (SQUID) magnetometer was used to obtain the susceptibility of a small aligned single crystal along two mutually perpendicular crystalline axes. The zero field heat capacity of a powder sample was measured using a specially designed tail mounted in the dilution refrigerator.

The fact that the crystal-field term is much larger than the exchange term in the spin Hamiltonian allows for a straight-forward theoretical solution in terms of an anisotropic Heisenberg superexchange. Using the energy levels predicted by this model, it became evident that electron spin resonance (ESR) should provide a direct verification of these levels. Spin resonance studies were undertaken at 1 - 4 K in both X and K-band frequency ranges. A very small aligned single crystal was measured at 9.3 GHz, and a powder sample was studied over a wide spectrum of frequencies (8.7 - 24 GHz). The results of these observations yield the transitions consistent with the energy levels predicted by the theoretical formulation.

# CHAPTER I

## THE EXPERIMENTAL APPARATUS

### A. Dilution Refrigerator

A dilution refrigerator was initially constructed by this research group to make low temperature magnetic susceptibility measurements.[6] The design was sufficiently flexible that it has also been used to make heat capacity measurements.

The operation of a $^3He$-$^4He$ dilution refrigerator is based on the phase separation of a mixture of $^3He$ and $^4He$ into a $^3He$ concentrated region and a $^3He$ diluted region.[7] Since the entropy of a $^3He$ atom is larger in the $^4He$-rich layer than in the $^3He$-rich layer, a cooling of the surroundings is made possible when $^3He$ atoms pass from the $^3He$ concentrated region across the phase boundary into the $^3He$ dilute region. The entropy per $^3He$ atom has increased with a corresponding absorption of heat from the dilute solution. This represents a cooling process.

The design of a dilution refrigerator combines the phase separation process with a means of achieving the low temperatures at which the dilution occurs and a means of allowing continuous circulation of the $^3He$ atoms. In practice $^3He$ atoms enter the refrigerator as a gas and pass through a condensing capillary thermally anchored to a 1° Pot. This 1° Pot acts as a small evaporation refrigerator

in which $^4$He liquid is pumped on causing the temperature of the liquid to be lowered to approximately 1 K. Immediately following the condensing capillary is a large flow impedance which results in a high enough pressure to ensure liquification of the incoming $^3$He gas. The liquid $^3$He then passes through one capillary and three sintered copper heat exchangers for further cooling. The concentrated $^3$He then enters the mixing chamber where the actual phase separation occurs. From here the dilute $^3$He returns via the heat exchangers to the still. At the still temperature (approximately .65 K), the $^3$He atoms have a higher vapor pressure than the $^4$He atoms. With proper suppression of the $^4$He superfluid film flow, the vapor pressure difference allows the $^3$He atoms to be selectively pumped from the still to the room temperature part of the system. The retrieved $^3$He gas is then compressed and returned to the refrigerator as input to the condensing capillary. This results in a closed continuous cycle dilution refrigerator.

Of particular interest to this work is the dual tail mixing chamber designed for our apparatus.[6] This design is shown in Figure 1. Tail #2 contains a pill of cerium magnesium nitrate (CMN) or 10% cerium magnesium nitrate and 90% lanthanum magnesium nitrate (LCMN) for thermometry. (These materials have a linear dependence of magnetic susceptibility on inverse temperature into the millikelvin range, making them excellent thermometers.) Tail #1 normally contains the sample whose susceptibility is to be measured as

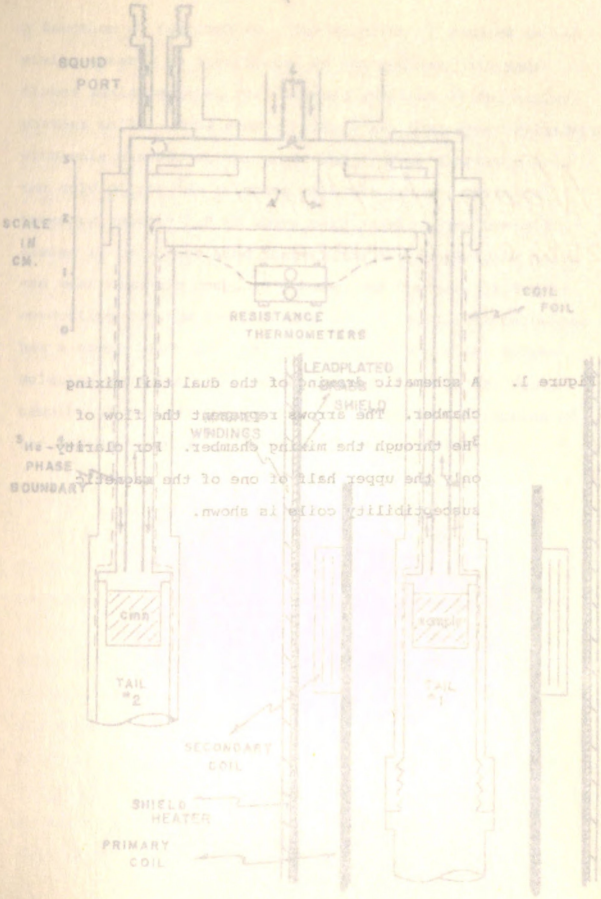
SQUID PORT
SCALE IN CM.
RESISTANCE THERMOMETERS
COIL FOIL
LEADPLATED SHIELD
WINDINGS
PHASE BOUNDARY
TAIL #2
TAIL #1
SECONDARY COIL
SHIELD HEATER
PRIMARY COIL

Figure 1. A schematic drawing of the dual tail mixing chamber. The arrows represent the flow of $^3$He through the mixing chamber. For clarity only the upper half of one of the magnetic susceptibility coils is shown.

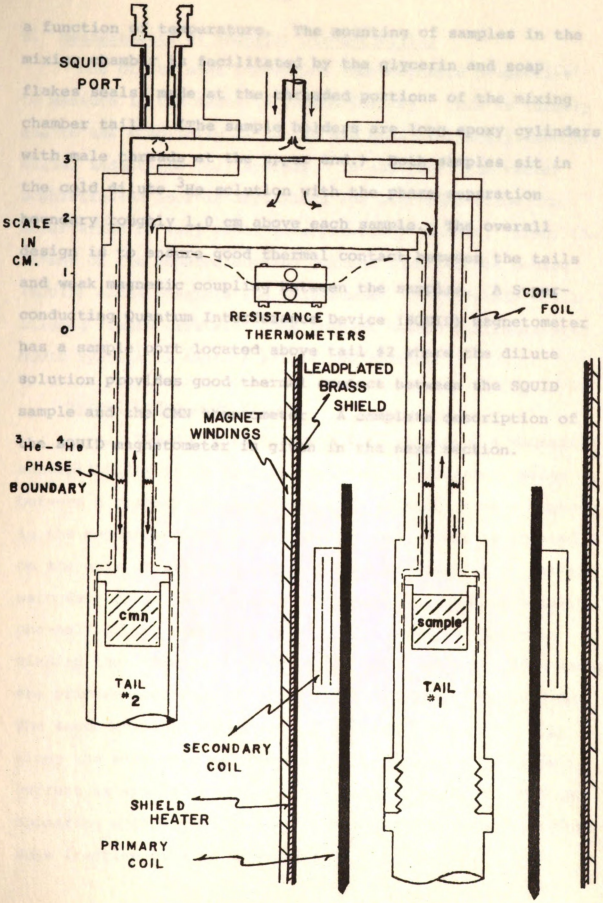
SQUID PORT
SCALE IN CM.
3
2
1
0
RESISTANCE THERMOMETERS
COIL FOIL
LEADPLATED BRASS SHIELD
MAGNET WINDINGS
$^3He - ^4He$ PHASE BOUNDARY
cmn
sample
TAIL #2
TAIL #1
SECONDARY COIL
SHIELD HEATER
PRIMARY COIL

a function of temperature. The mounting of samples in the mixing chamber is facilitated by the glycerin and soap flakes seals[8] made at the threaded portions of the mixing chamber tails. (The sample holders are long epoxy cylinders with male threads at the upper end.) Both samples sit in the cold dilute $^3$He solution with the phase separation boundary roughly 1.0 cm above each sample. The overall design is to ensure good thermal contact between the tails and weak magnetic coupling between the samples. A Superconducting Quantum Interferance Device (SQUID) magnetometer has a sample port located above tail #2 where the dilute solution provides good thermal contact between the SQUID sample and the CMN thermometer. A complete description of the SQUID magnetometer is given in the next section.

B. Measurements of Magnetic Susceptibility

One of the most convenient thermodynamic properties to measure is the magnetic susceptibility. This is largely due to the simplicity of design and ease of installation of mutual inductance coil systems. In addition, the rather sophisticated lock-in amplifiers now available allow the observation of very small susceptibility changes. Also, the advent of the Superconducting Quantum Interferance Device (SQUID) makes possible the measurement of extremely small aligned single crystals. The compact design available with SQUID systems is another attractive feature.

Mutual Inductance Bridge

The conventional method of obtaining a magnetic susceptibility is to measure the mutual inductance change between a primary and secondary coil brought on by a change in the magnetization of the sample. The sample is located on the axis of the coil system within one-half of an astatic secondary coil. The astatic arrangement is made by winding one-half of the secondary coil in one direction and then winding the other half in the opposite direction. This makes the primary-secondary mutual inductance zero to first order. The secondary coil halves are wound over the primary coil along the same axis as illustrated in Figure 1. A 17 Hz current is applied to the primary coil, and the induced emf appearing across the secondary is balanced against an adjustable fraction of a 17 Hz reference voltage. This makes

possible a very accurate null measurement which can be enhanced by the use of a lock-in amplifier tuned to a very narrow band of frequencies centered about the AC driving frequency. As the temperature of the sample is changed, the magnetization of the sample changes causing a measurable output voltage to appear at the lock-in. This voltage is then nulled by adjusting the reference ratio transformer. This AC bridge is patterned after one reported by A. C. Anderson et.al.[9] with detailed descriptions available in the Ph.D. thesis of J. L. Imes.[6]

Because of the dual tail arrangement, it is necessary to magnetically isolate the two coil systems from each other. This is done by rigidly connecting each coil to a superconducting shield made from a brass tube of 4.76 cm i.d. and .079 cm wall thickness, the inside of which is electroplated with a .003 cm layer of lead. The coil #1 shield also has a heater and superconducting solenoid wrapped around its outside to allow for the application and trapping of DC magnetic fields as large as 200 gauss. This is also shown in Figure 1. The shield #1 heater consists of approximately 1 m of .01 cm diameter manganin wire having a resistance per unit length of 105 Ω/m. It is wrapped in a snakelike fashion up and down over the cylindrical outer area of the shield. It is held in place with a thin layer of GE7031 varnish. The magnet consists of 487 turns of .023 cm diameter Kryoconductor superconducting wire[10] wrapped in one layer on a hollow mylar tube. The tube was slightly oversized so that it would easily

slide over the shield and heater. It rested on pieces of string wrapped around the perimeter of the shield cylinder and over the heater. The string provides some thermal isolation of the superconducting solenoid windings from the heater. The solenoid was 5.08 cm in diameter and 11.1 cm long, having a field capability of 50 gauss/amp.

SQUID Magnetometer

The Superconducting Quantum Interference Device (SQUID) is an extremely sensitive flux measuring device. Its operation is based on the Josephson theory[11] of tunneling currents between two superconducting materials. The Josephson junction, superconducting weak link, and point contact are used interchangeably to mean any low critical current connection between two pieces of superconductor. The relevant equation resulting from the Josephson theory[12] is

$$I_s = I_c \sin \theta \qquad (1)$$

where $I_s$ is the supercurrent through the junction, $\theta$ is the quantum-mechanical phase difference across the junction, and $I_c$ is the critical current, a characteristic parameter for a particular junction. A niobium cylinder, containing two holes situated symmetrically about a slot down the axis of the cylinder, has a weak link made by causing the tips of two 000-120 niobium screws to touch across the slot. This two-hole symmetric SQUID is shown in Figure 2. Now the total flux trapped within one of these holes as a

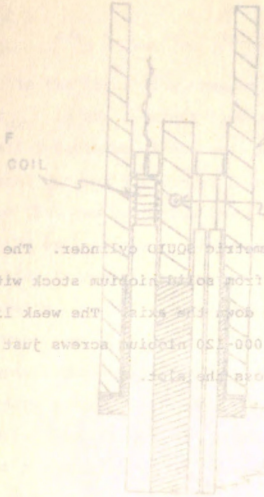
NIOBIUM
SQUID
CYLINDER
RF
COIL
POINT
CONTACT


POINT
CONTACT

Figure 2. Two-hole symmetric SQUID cylinder. The cylinder is machined from solid niobium stock with a slot running down the axis. The weak link is made by two 000-120 niobium screws just touching across the slot.

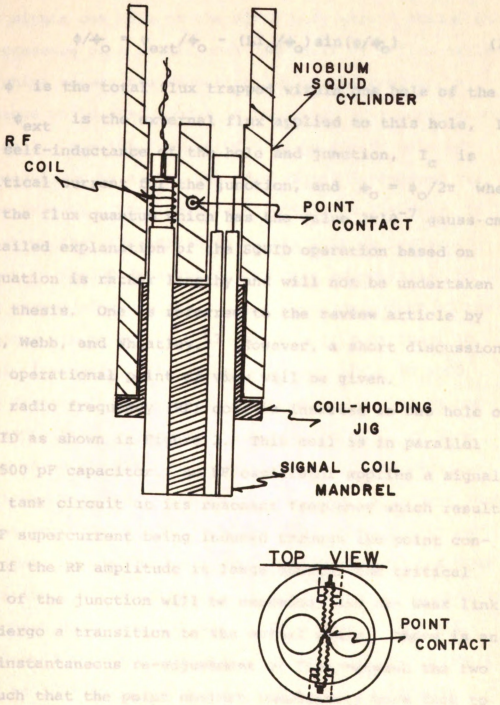
NIOBIUM
SQUID
CYLINDER
RF
COIL
POINT
CONTACT
COIL-HOLDING
JIG
SIGNAL COIL
MANDREL
TOP VIEW
POINT
CONTACT
RF

function of an applied external flux when the cylinder is superconducting gives rise to a step-like dependence which is used to explain the details of the SQUID operation. This relation has the form:

$$\phi/\Phi_o = \phi_{ext}/\Phi_o - (LI_c/\Phi_o)\sin(\phi/\Phi_o) \qquad (2)$$

where $\phi$ is the total flux trapped within one hole of the SQUID, $\phi_{ext}$ is the external flux applied to this hole, L is the self-inductance of the hole and junction, $I_c$ is the critical current for the junction, and $\Phi_o = \phi_o/2\pi$ where $\phi_o$ is the flux quantum which has the value $2\times10^{-7}$ gauss·cm$^2$. The detailed explanation of the SQUID operation based on this equation is rather lengthy and will not be undertaken in this thesis. One is referred to the review article by Giffard, Webb, and Wheatley.[13] However, a short discussion from an operational point of view will be given.

A radio frequency (RF) coil is inserted in one hole of the SQUID as shown in Figure 2. This coil is in parallel with a 500 pF capacitor. An RF oscillator applies a signal to this tank circuit at its resonant frequency which results in an RF supercurrent being induced through the point contact. If the RF amplitude is large enough, the critical current of the junction will be exceeded, and the weak link will undergo a transition to the normal state. There is an almost instantaneous re-adjustment of flux between the two holes such that the point contact immediately goes back to the superconducting state. This RF induced transition takes

place about the average DC flux in the SQUID cylinder. Since the rest of the niobium cylinder is always in a superconducting state, the average DC flux trapped within the entire SQUID body is a constant. Thus, if the average DC flux within one hole of the SQUID body should change due to the presence of a signal coil (one-half of a flux transformer which senses the magnetization of the sample), a flux change would also appear in the other hole containing the RF coil. Now the average DC flux in the RF hole is slowly modulated by a 1000 Hz audio signal introduced via the same RF coil. Through a rather detailed analysis, it can be shown that the amplitude of the 1000 Hz frequency component at the RF detector is directly proportional to the DC flux change of the signal coil. Thus the output of the RF detector can be fed into a lock-in amplifier tuned to the audio frequency. The output of the lock-in is a DC voltage directly proportional to any small DC flux change in the SQUID body. To ensure that the change in DC flux experienced by the RF coil is small (a condition necessary for a linear response), a feedback resistor sends back just the right amount of DC flux to the RF coil to balance out the original change in flux. This is the flux-locked mode of operation. A digital voltmeter (DVM) is used to measure the feedback voltage which now varies linearly with the flux change due to the signal coil. Flux changes as small as $10^{-2}$ to $10^{-4}$ of $\phi_o$ can be detected, the ultimate sensitivity being limited by noise in the SQUID body and in

the amplifiers.

A flux transformer is used to couple the flux change due to the sample magnetization into the SQUID sensor body. This consists of a superconducting sample coil having two halves wound in series opposition (astatic) to mimimize the effect of external magnetic field changes. The sample of interest is placed within one-half of the sample coil. This coil is connected via a tightly twisted pair of superconducting leads to another coil, the signal coil, which is inserted into one of the holes in the niobium SQUID cylinder. The complete SQUID circuit is shown in Figure 3. The RF coil resides in the other hole. The flux coupled into the SQUID body is given by:

$$\phi = M\ I \tag{3}$$

where $M$ is the mutual inductance between the signal coil and the SQUID body, and $I$ is the current in the signal coil due to the change in magnetization of the sample. Now the current due to the sample is obtained from

$$N\ \Phi_{sample} = L\ I \tag{4}$$

where $N$ is the number of turns in one-half of the sample coil, $\Phi_{sample}$ is the flux due to the sample magnetization, and $L$ is the total self-inductance of the flux transformer.

$$L = L_{signal} + L_{sample} + L_{leads} \tag{5}$$

If the sample is small compared to the coil diameter, the equation for a uniformly magnetized sample may be used:

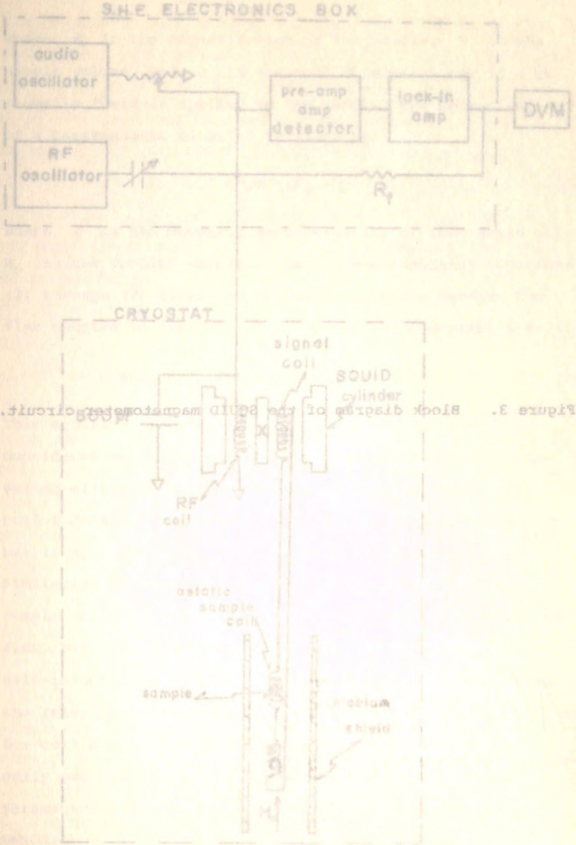
S.H.E. ELECTRONICS BOX
audio oscillator
RF oscillator
pre-amp amp detector
lock-in amp
DVM
$R_f$
CRYOSTAT
signal coil
SQUID
cylinder
RF coil
sample
$H_s$

Figure 3. Block diagram of the SQUID magnetometer circuit.

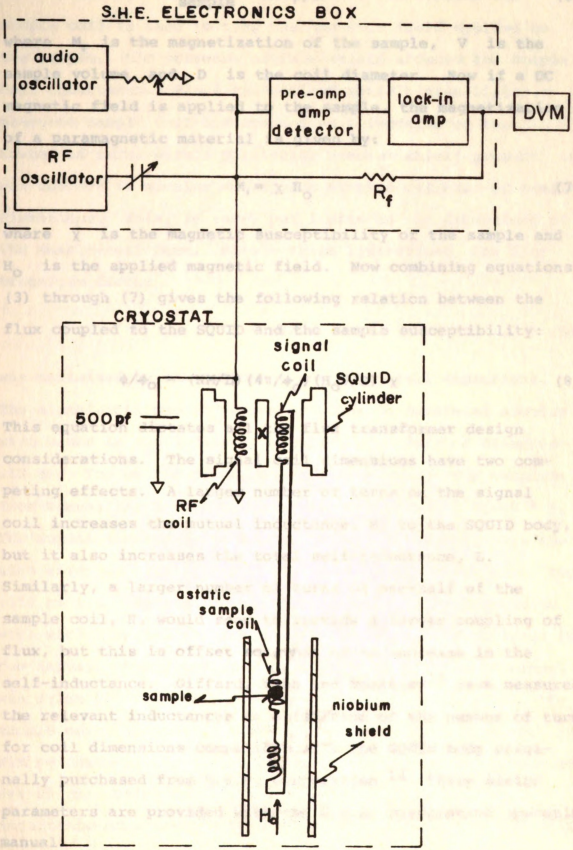
S.H.E. ELECTRONICS BOX
audio oscillator
RF oscillator
pre-amp amp detector
lock-in amp
DVM
$R_f$
CRYOSTAT
signal coil
SQUID cylinder
500pf
RF coil
astatic sample coil
sample
niobium shield
$H_o$

$$\Phi_{sample} = 4\pi M_1 V/D \qquad (6)$$

where $M_1$ is the magnetization of the sample, V is the sample volume, and D is the coil diameter. Now if a DC magnetic field is applied to the sample, the magnetization of a paramagnetic material is given by:

$$M_1 = \chi H_o \qquad (7)$$

where $\chi$ is the magnetic susceptibility of the sample and $H_o$ is the applied magnetic field. Now combining equations (3) through (7) gives the following relation between the flux coupled to the SQUID and the sample susceptibility:

$$\phi/\Phi_o = (NM/L)(4\pi/\Phi_o)(H_o V/D)\ \chi \qquad (8)$$

This equation dictates all the flux transformer design considerations. The signal coil dimensions have two competing effects. A larger number of turns on the signal coil increases the mutual inductance, M, to the SQUID body, but it also increases the total self-inductance, L. Similarly, a larger number of turns on one-half of the sample coil, N, would seem to provide a larger coupling of flux, but this is offset somewhat by an increase in the self-inductance. Giffard, Webb and Wheatley[13] have measured the relevant inductances as a function of the number of turns for coil dimensions compatible with the SQUID body originally purchased from S.H.E. corporation.[14] These design parameters are provided with the S.H.E. corporation operating manual.

A hollow niobium shield-cylinder surrounding the sample coil is used to trap the magnetic field applied to the sample. The presence of this shield affects the sample coil inductance. Since the Giffard article also lists measured sample coil inductances as a function of the number of turns with a particular niobium shield present, it was decided to machine a trapping niobium cylinder of similar dimensions. This, in turn, put limits on the dimensions of the sample-coil form. Within these limitations, the flux transform factor

$$f = NM/L \qquad (9)$$

was maximized by the following choice of coil dimensions. The signal coil was 117 turns of .0096 cm insulated niobium wire wound in two layers on a Delron coil form of diameter .13 cm. The self-inductance obtained from the SHE corporation manual for a coil of these dimensions was $4.75 \times 10^{-6}$ H. The mutual inductance to the SQUID body for such a coil was also given as $1.43 \times 10^{-8}$ H. The sample coil consisted of two .356 cm i.d. sections of 21 turns each of .0096 cm niobium wire with a center to center separation of .64 cm between the two halves. The self-inductance given by the S.H.E. manual was $2.15 \times 10^{-6}$ H. The length of leads necessary to join the sample coil, located in the SQUID chamber mounted on the mixing chamber, to the signal coil, located in the SQUID body, was 89 cm. Using the figure of $3 \times 10^{-7}$ H/m for the lead inductance of a tightly twisted pair[13], the flux transformer

lead inductance, $L_{leads}$, was calculated to be $.3 \times 10^{-6}$ H. Thus the flux transform factor, f , was calculated to be .032 which is very near to the optimum value suggested by the S.H.E. corporation manual. The hollow niobium shield mounted around the sample coil is .51 cm i.d. with a length of 1.59 cm and .063 cm wall thickness. The SQUID sample coil, niobium shield, sample chamber, and other relevant features are shown in Figure 4. It should be noted that the first successful SQUID run was done using a .0048 $cm^3$ sample of 100% CMN with a mass of 6.4 mgm in a field of 0.25 gauss. CMN has a Curie-law dependence of susceptibility on temperature

$$\chi = C/T \tag{10}$$

where C is the Curie constant, and T is the absolute temperature. The measured value gave a dependence of $\phi/\phi_o$ = (2.32 K)/T as compared to the calculated value of (2.5 K)/T based on the design parameters applied to equation (8). The agreement is considered quite good.

In order to apply a stable DC magnetic field to the sample, a number of design considerations are necessary. To minimize the effect of external magnetic fields (notably, the earth's), a lead shield within another shield of high permeability (mu-metal) is placed on the outer wall of a vacuum can which surrounds the refrigerator. In addition there is the shield consisting of the niobium cylinder around the sample coil. The magnetic field is applied parallel to the axis of the sample coil by a superconducting

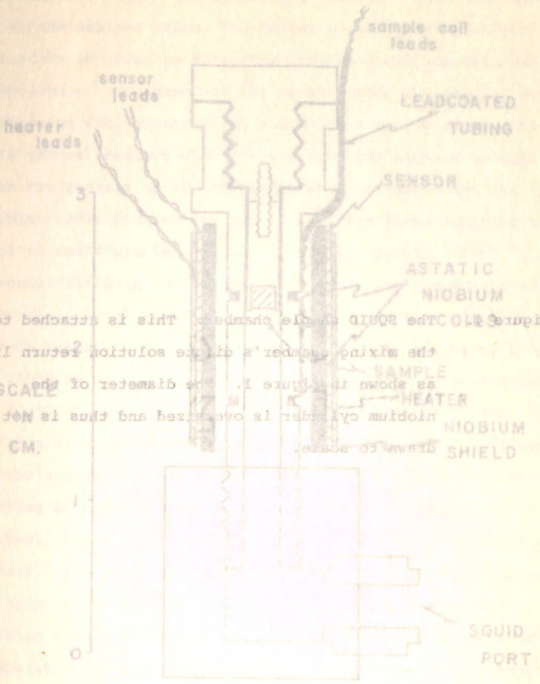
sample coil leads
sensor leads
heater leads
LEADCOATED TUBING
SENSOR
ASTATIC NIOBIUM
SAMPLE
HEATER
NIOBIUM SHIELD
SQUID PORT
SCALE
CM.
3
2
1
0

Figure 4. The SQUID sample chamber. This is attached to the mixing chamber's dilute solution return line as shown in Figure 1. The diameter of the niobium cylinder is oversized and thus is not drawn to scale.

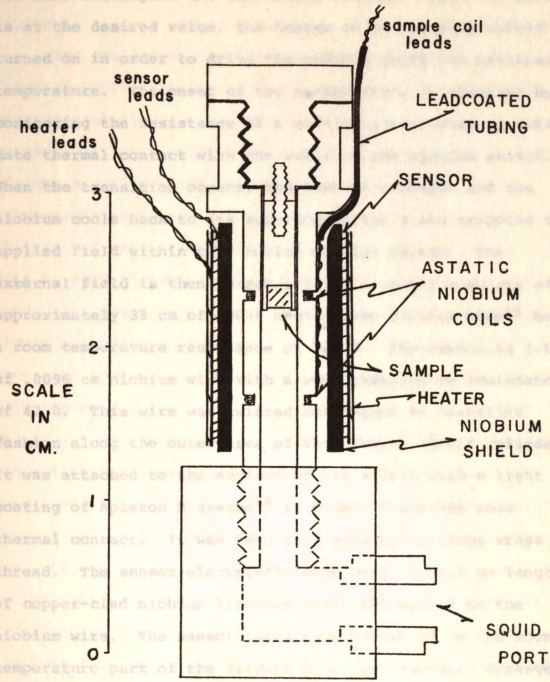
sample coil leads
sensor leads
heater leads
LEADCOATED TUBING
SENSOR
ASTATIC NIOBIUM COILS
SAMPLE
HEATER
NIOBIUM SHIELD
SQUID PORT
SCALE IN CM.
3
2
1
0

solenoid wound on an inner vacuum can which surrounds only the heat exchangers and the mixing chamber. When the field is at the desired value, the heater on the niobium shield is turned on in order to drive the niobium above its critical temperature. The onset of the normal state is observed by monitoring the resistance of a niobium sensor wire in intimate thermal contact with the walls of the niobium shield. When the transition occurs, the heat is removed; and the niobium cools back to its superconducting state trapping the applied field within this hollow niobium shield. The external field is then turned off. The heater consists of approximately 33 cm of .0036 cm diameter Evanohm wire[15] having a room temperature resistance of 320 Ω. The sensor is 1.05 m of .0096 cm niobium wire with a room temperature resistance of 42 Ω. This wire was twisted and lagged in snakelike fashion along the outer area of the niobium shield cylinder. It was attached to the surface of the shield with a light coating of Apiezon N grease[16] in order to provide good thermal contact. It was then tied down by numerous wraps of thread. The sensor electrical leads were two 1.3 cm lengths of copper-clad niobium-titanium wire spot-welded to the niobium wire. The sensor leads were connected to the room temperature part of the circuit by a four-terminal arrangement. This was to ensure a true current-voltage measurement of the sensor resistance, thereby minimizing lead resistance effects. The heater is well lagged to a piece of cigarette paper glued in place over the sensor and cylinder with GE 7031

varnish. Numerous wraps of thread are also used to hold the heater in place. The heater and sensor are also shown in Figure 4.

The small flux changes observable by the flux transformer - SQUID combination require careful shielding from any external fields, even the small fields produced by nearby current-carrying leads. The flux transformer leads connecting the signal coil to the sample coil were placed in a cupro-nickel tube of length 74 cm with an inner diameter of .061 cm and wall thickness of .0075 cm. This tube was coated with a .0025 cm layer of lead-tin solder to provide a superconducting magnetic shield around the leads when used at liquid helium temperatures. The leads from the sample coil were also encased in a lead-coated cupro-nickel tube specially designed to fit under the niobium shield as shown in Figure 4. The leads from this point to the longer interconnecting leads mentioned above were shielded with a 15 cm length of indium foil. The foil was rolled out to a thickness of .01 cm and width .5 cm and folded over the leads. The foil was sealed shut with a warm soldering gun. The indium foil was very flexible and was easily lagged to the upper copper flange on the mixing chamber so as to minimize the heat flow to the magnetometer from the higher temperature parts of the refrigerator. At the signal coil end of the flux transformer, the entire SQUID cylinder including signal coil, RF coil, and 500 pF capacitor were all encased in a lead-foil shield, mounted in the vacuum space, and thermally

anchored to the 4 K bath.

Due to the weak nature of the Josephson junction, it is essential to shield this point contact from any type of electrical discharges which might change the critical current of the junction. This necessitates a complete electrostatic shield extending upwards from the lead-foil shield mentioned above to the room temperature part of the system where the SQUID electronics are located. This shield is a stainless steel tube, 1.27 cm outer diameter with a .041 cm wall thickness. It contains the leads which bring the RF signal from the room temperature electronics to the RF coil. This shield is carefully grounded to the top of the cryostat at the point where the RF signal is fed into the cryogenic part of the system. The ground is made completely around the outer circumference of the tube by a tight press fit into a 1.27 cm hole drilled in the top of the cryostat. This is the only ground point for the entire SQUID system, so as to avoid any ground-loop currents which might affect the SQUID operation.

Since the operation of the SQUID is dependent on the RF signal, it is essential to prevent any external radio frequency energy from entering the cryostat. For this reason, all the SQUID heater and sensor leads pass through RF filters consisting of 22 μH inductors in series and 1000 pF capacitors to ground.

C. Heat Capacity Measurements

In order to make heat capacity measurements in the temperature range of interest, it was necessary to design a special addition to the refrigerator. The heat capacity addition is a modification of epoxy sample holder #1. Figure 5 shows the relevant details of this addition. A sintered copper cylinder approximately 1 cm high sits in the dilute $^3$He of the mixing chamber where a paramagnetic sample would normally be located. There is a .318 cm diameter, OFHC copper "stem" extending from the sintered copper down through the center of the epoxy piece containing the threads. The large surface area of contact presented by the sintered copper to the dilute $^3$He solution provides good thermal contact via the copper stem for cooling the sample mounted below. The leak tight seal through the epoxy is made by a special "housekeeper's seal" to allow for the differential thermal contraction of the epoxy and copper. (The copper stem and the copper piece for completing the housekeeper's seal are soldered together with Wood's metal.) At the bottom of the copper stem is a flattened tab where a superconducting heat switch is attached via spot welds to platinum tabs. The heat switch consists of a piece of 99.9999% pure zinc of mass .03 gm shaped into a thin strip 8.3 cm long, .091 cm wide, and .0076 cm thick. This gives a length to cross-sectional area ratio of $1.2 \times 10^4$ cm$^{-1}$. The large $\ell/A$ ratio is to ensure a minimal heat flow due to a temperature gradient across the zinc. The critical

Figure 5. A schematic diagram of the heat capacity tail. This unit is joined to the refrigerator via a glycerin and soap flakes seal at the epoxy threads. The threads are machined so that the unit screws into the place in the mixing chamber occupied by tail #1 as illustrated in Figure 1.

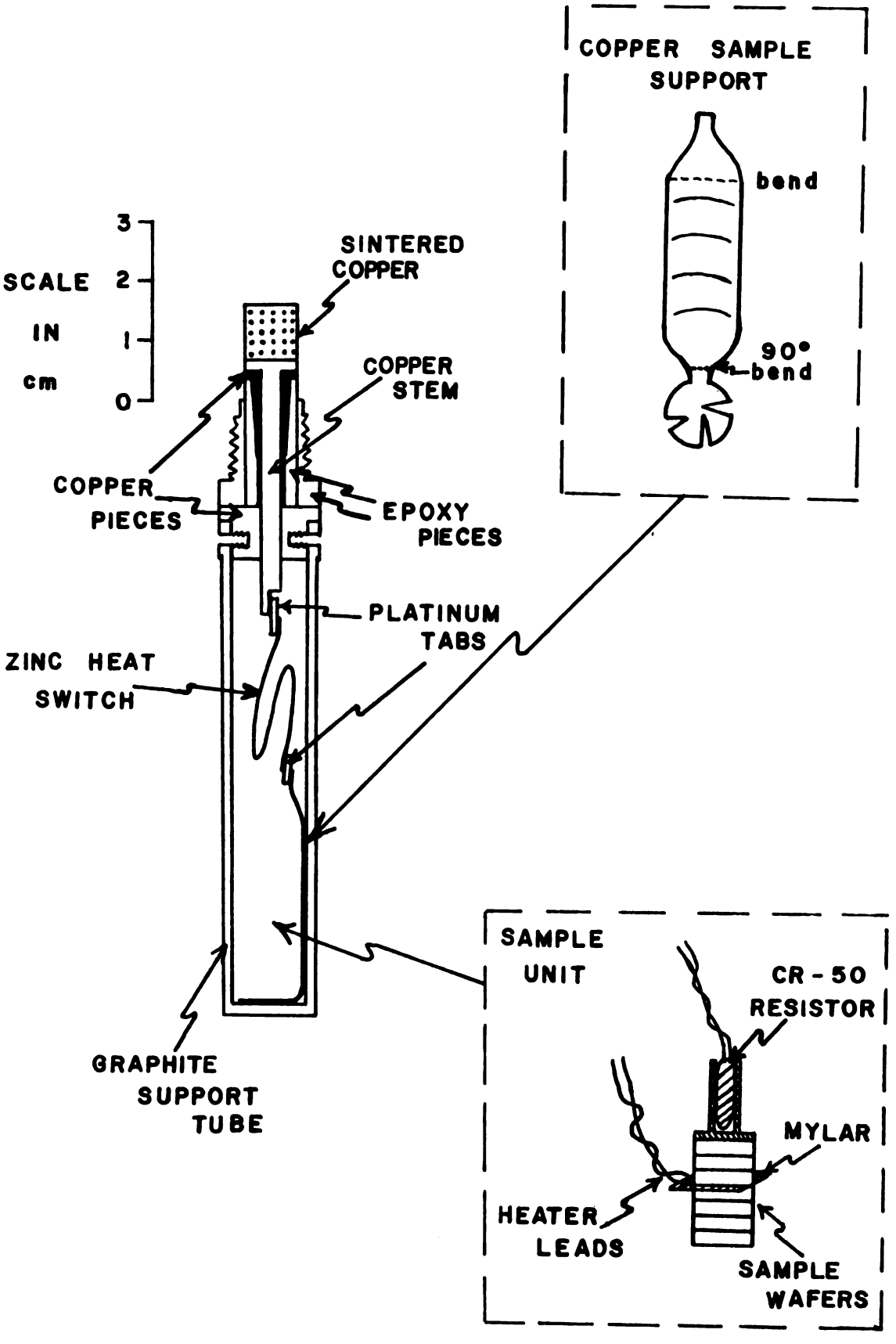
COPPER SAMPLE SUPPORT
bend
90°
bend
SCALE IN cm
3
2
1
0
SINTERED COPPER
COPPER STEM
COPPER PIECES
EPOXY PIECES
PLATINUM TABS
ZINC HEAT SWITCH
GRAPHITE SUPPORT TUBE
SAMPLE UNIT
CR-50 RESISTOR
MYLAR
HEATER LEADS
SAMPLE WAFERS

temperature of zinc is 0.85 K, and the critical field is 52 Gauss.[17] These superconducting properties are the basis for the operation of the heat switch. The thermal conductivity of a superconductor is phonon limited and varies as $T^3$. At temperatures above the transition, the conductivity is primarily due to electrons and varies as T. Thus to cool the sample the switch must be closed (i.e. in its conducting state) requiring the superconducting metal to be in its normal state. A way this can be done when the absolute temperature is below the transition temperature of the metal is by the application of a sufficiently large magnetic field (i.e. larger than the critical field) to drive the material into its normal state. (A magnetic field of 150 gauss was used in the experiment.) The magnet wound around the coil #1 shield (Figure 1) is used to produce this field. When the lowest temperature is reached, the magnetic field is removed; and the zinc goes back to its superconducting state of low thermal conductivity. The heat switch is now open, and the sample is thermally isolated from the rest of the refrigerator.

To make the heat capacity measurements a heat pulse is applied to the sample through a heater sandwiched between two of the sample wafers (see Figure 5). The resistance of a calibrated germanium resistor mounted on the sample is read before and after the heat pulse to obtain the temperature change produced in the sample by the pulse. As the sample temperature is increased toward the zinc transition

temperature, it becomes more necessary to minimize the temperature gradient between the refrigerator and the sample. Thus the refrigerator temperature determined by the LCMN thermometer in tail #2 was paced with the sample temperature. As mentioned earlier, the large length to cross-sectional area ratio ($\ell/A$) for the heat switch also helps minimize the thermal leakage in the 1 K temperature range. (This is the upper limit of the temperature range investigated.) It should also be noted that too large an $\ell/A$ ratio would have resulted in an unacceptably long cool down time for the sample.

The heater used to supply the heat pulse was made of approximately 15 cm of Evanohm wire.[15] This wire was .0036 cm in diameter and had no insulation. It has a resistance of 1346 Ω/m. This length of wire was lagged down in snake-like fashion to a .00064 cm thick piece of mylar using a thin layer of GE 7031 varnish. The mylar was a square of side .9 cm, and the heater wire was centered so that it would be completely covered by the area of one of the sample wafers. The room temperature resistance of the heater was measured to be 205 Ω. During the actual experiment the heat pulse was delivered and monitored by a 4-terminal current-voltage arrangement to eliminate to first-order lead resistance effects. The only 2-terminal section of the circuit was the length of leads right at the sample, and these were made with niobium superconducting wire. The mylar square containing the heater was greased on both sides

using Apiezon N grease[16] and placed between the fourth and fifth sample wafers. The sample consisted of seven wafers, each press-fitted into a rugged free-standing form using a brass die and plunger. This die was 6.6 cm long with a .98 cm inner diameter and a 1.9 cm outer diameter. It was machined to accept a solid brass seat .84 cm in height with the same diameter as the die. A solid brass plunger 6.1 cm long and .98 cm in diameter was also made. Approximately .21 gm of FeTPPCl powder was placed in the die with the brass seat in place. The seat was covered with a thin layer of teflon tape to prevent the sample from sticking to the seat. A light layer of silicone grease was placed around the inside of the die to prevent the powder from sticking to the sides. Two or three drops of chloroform were added to the sample powder in hopes of dissolving some of the powder. The brass die was then warmed with a heat gun to drive off the chloroform, hoping to leave behind polycrystalline globs that were adhering well to each other. After cooling, the plunger, with teflon tape covering, was inserted and the sample pill was pressed to approximately 84% of the crystalline density using a hydraulic press. Then the sample pill was removed by pushing the plunger all the way through the die. Seven sample pills, approximately .26 cm thick by .98 cm diameter with a mass of approximately .21 gm each, were fabricated in this manner. The pills were then placed on the bottom of a glass dish and set on a hot plate at a temperature of about 100°C. Apiezon N grease was heated in a separate beaker to the point that it melted. Then a drop of the hot liquid

grease was placed on each sample pill and allowed to soak in. The pills were then allowed to cool. The result was a rather rugged free-standing sample in which the individual grains were hopefully in good thermal contact with each other due to the impregnation of grease. The grease also acts as a filler to give mechanical strength to the pills. The sample pills were then placed one on top of the other with a thin layer of Apiezon N grease between each wafer. The sample mass without grease was 1.509 gm. The total mass of grease impregnated in the seven wafers was .067 gm. The total sample formed a cylinder 1.9 cm high of diameter .98 cm with the heater sandwiched within. The temperature of the sample was measured using a Cryocal CR-50 germanium resistor[18] calibrated down to .04 K. This resistor was mounted in a copper resistor-well of mass .54 gm with a grooved base of diameter .98 cm. It was held in place on top of the sample with a thin layer of Apiezon N grease. The copper leads of the CR-50 were well lagged to this resistor mount. The low temperature part of the circuit was completed using niobium superconducting wire up to the 4 K bath region of the refrigerator. The connection from the zinc heat switch to the sample is made via a thin copper foil support. This is also shown in Figure 5. This support has a curved back to conform to the sample shape. A circular base for the sample to rest on is perpendicular to the support back. This foil was .015 cm thick with a mass of 0.6 gm. The top of the foil has a small copper tab which was

spot-welded to a platinum tab of mass .02 gm. The platinum tab was then spot-welded to the zinc heat switch. The base of the foil support is notched to reduce eddy current heating when the magnetic field is removed to open the heat switch. The base of the support was well scored with a razor knife and then coated with grease to provide good thermal contact to the sample. The sample and copper support were placed inside a thin graphite support tube attached to the epoxy piece at the top. The purpose here is to provide mechanical strength without sacrificing thermal isolation. Half of this tube was machined away to provide access for insertion of the sample and support piece. This tube is 7.6 cm long, 1.52 cm in diameter, and .08 cm in wall thickness. Graphite was chosen because of its poor thermal conductivity and good mechanical rigidity. The space in the cryostat occupied by the sample unit is normally at a high vacuum. However, in the initial stages of refrigeration, $^3$He exchange gas is allowed to enter this region to cool the refrigerator to 4 K during the transfer of liquid $^4$He into the main bath. Then the exchange gas is pumped away, and the dilution refrigerator is started up. However, $^3$He is highly adsorbed inside graphite and is almost impossible to completely pump away at 4 K. This could lead to problems when the sample is heated since some remnant $^3$He gas could boil off the graphite providing a thermal short to the refrigerator and modifying the apparent heat capacity of the sample. To avoid this adsorption, a light coating of GE 7031 varnish was applied over the entire

surface of the graphite. Also, a copper can, .013 cm thick, was placed over the graphite support tube to minimize the $^3$He exchange gas entering the sample region and to provide a shield against thermal radiation, RF interference, and relatively hot $^3$He atoms coming off the walls of the inner vacuum can.

D. Thermometry

The low temperatures attained in our system are measured by the Curie law extrapolation of the susceptibility of cerium magnesium nitrate (CMN) or 10% cerium magnesium nitrate and 90% lanthanum magnesium nitrate (LCMN). These materials are characterized solely by their weak magnetic dipole-dipole interactions. Thus they are accurately described as a system of non-interacting spins down to the millikelvin temperature range (about 6 mK for CMN). The magnetic susceptibility of such a system is described by the relation

$$\chi = C/T^* \tag{11}$$

where $C$ is the Curie constant and $T^*$ is the magnetic temperature of the spin system which is assumed to be in good thermal equilibrium with the lattice. The susceptibility of a CMN powder sample is measured from 4 K to .3 K using the mutual inductance bridge mentioned earlier with the temperature obtained from a calibrated germanium resistor (CR-100).[19] A least-squares fit is applied to this data to yield a best slope and intercept for a linear extrapolation of the CMN susceptibility to lower temperatures. The CMN susceptibility is then measured, and from the fit a temperature is determined. The CR-100 germanium resistor was calibrated against the vapor pressure of $^3$He in a previous run.[6]

For the heat capacity measurements, the temperature was measured using a calibrated CR-50 germanium resistor as mentioned earlier. This resistor was calibrated against the CR-100 resistor in the .3 K-4 K range and then against the extrapolated LCMN Curie law down to .04 K in a separate run. The calibration data are given in Table A1 of the Appendix. To obtain the fine interpolation necessary for the heat capacity measurements, the CR-50 calibration data were fitted in six different temperature ranges using the relation

$$\ell n\ R_{CR-50} = A_i\ T^{-\frac{1}{2}} + B_i \qquad (12)$$

where $T$ is the temperature determined by the CR-100 and LCMN corresponding to the resistance $R_{CR-50}$. $A_i$ and $B_i$ are the desired fitting parameters for the temperature range of interest ($i = 1, 6$). The fit for these regions was excellent with less than 1% deviation of any calculated value from a measured value. The heat capacity reduced data given in Table A5 are based on the $\ell n\ R_{CR-50}$ vs $T^{-\frac{1}{2}}$ fit.

## E. Electron Spin Resonance Apparatus

The electron spin resonance (ESR) measurements were made on a spectrometer in the lab of Professor J. A. Cowen with the help of Dr. Cowen and Paul R. Newman. These measurements were made in the 1-4 K temperature range at various frequencies. The temperature was determined from the $^4$He vapor pressure using mercury and oil manometers. X-band measurements were made in the frequency range of 8.7 - 10 GHz. Ku-band measurements were made from 10 - 17 GHz and one K-band run was made at 23.7 GHz. Single crystal measurements were made in a cylindrical cavity at X-band frequencies. Some powder measurements were made in a special variable-frequency tunable cavity designed by Paul R. Newman. The ESR spectra were displayed on an X-Y recorder where the X-axis is driven by the output voltage from a Hall probe measuring the magnetic field. The Y-axis is driven by the output voltage from a crystal detector which can be amplified to give a direct absorption signal. For derivative detection the magnetic field is modulated slightly at 280 Hz, and the output of the crystal detector is fed into a lock-in amplifier operating at the modulation frequency. The lock-in output is then used to drive the Y-axis of the recorder. Several ESR traces will be shown later. A small amount of diphenyl picryl hydrazyl (DPPH) was placed in each sample holder as a reference. DPPH has a very narrow resonance line and a well known isotropic g value of 2.004. This material acts as a convenient marker for that field corresponding to a g=2 transition. It is also a valuable

diagnostic for spectrometer operation.

## CHAPTER II

## THE STRUCTURE OF IRON TETRAPHENYLPORPHINE CHLORIDE

### A. General Information on Metallo-porphyrins

The metallo-porphyrins are a group of organic molecules containing a porphyrin plane with a metal atom in the center. The porphyrin plane consists of four pyrrole rings bonded together via methene bridge carbon-atoms (the meso-positions $\alpha,\beta,\gamma,\delta$) as shown in Figure 6. The pyrrole ring is a pentagon containing 4 carbon atoms and a nitrogen atom. The porphyrin molecule is essentially planar with a diameter of approximately 8.5 Å and a thickness of 4.7 Å.[2] The classification of the various metallo-porphyrins is based on the substitution of some or all of the hydrogen atoms bonded to positions 1-8 and to the methene bridge carbon atoms. The tetraphenylporphines are produced synthetically by attaching the six-sided phenyl rings at the $\alpha,\beta,\gamma,\delta$ positions. These phenyl rings bond in such a way that their plane is perpendicular to the porphyrin base plane in FeTPPCl. Protoporphyrin IX iron chloride (hemin) is a similar compound to FeTPPCl in that it has an iron atom at the center of the porphyrin plane with a chloride ion bonded above the iron. It has methyl groups at the 1,3,5,8 positions, vinyl groups at the 2,4 positions, propionic acid chains at the 6,7 positions, and hydrogen atoms at the

Figure 6. The upper diagram shows the structure of a metalloporphyrin molecule. The 1-8 positions, as well as the $\alpha,\beta,\gamma,\delta$ positions, are normally occupied by hydrogen ions. The site labelled M represents the metal atom.
The lower diagram shows the tetraphenyl structure, where the $\alpha,\beta,\gamma,\delta$ positions are now occupied by phenyl rings oriented approximately perpendicular to the porphyrin plane.

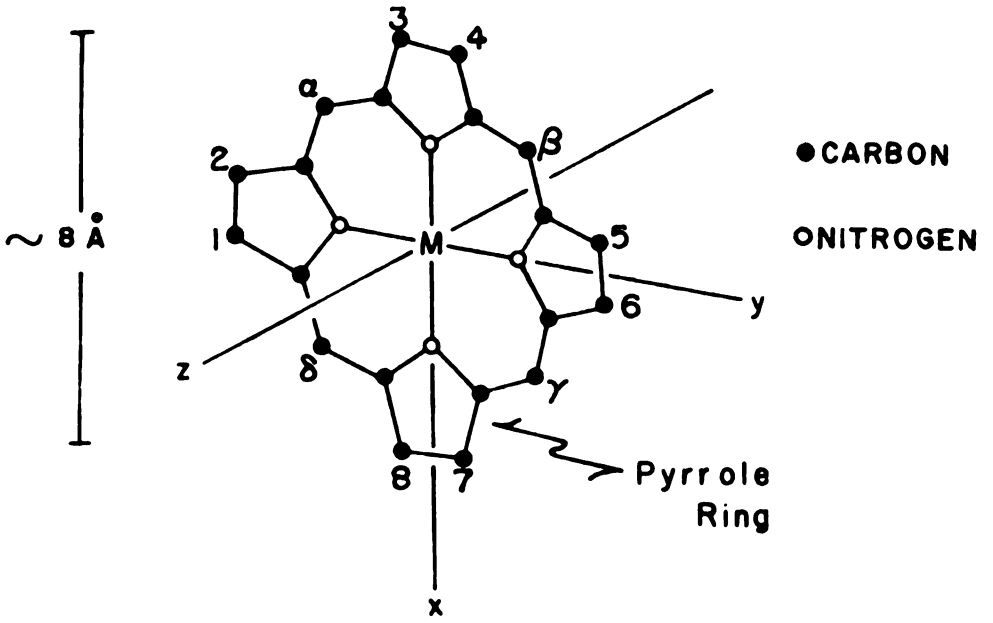


METALLOPORPHYRIN

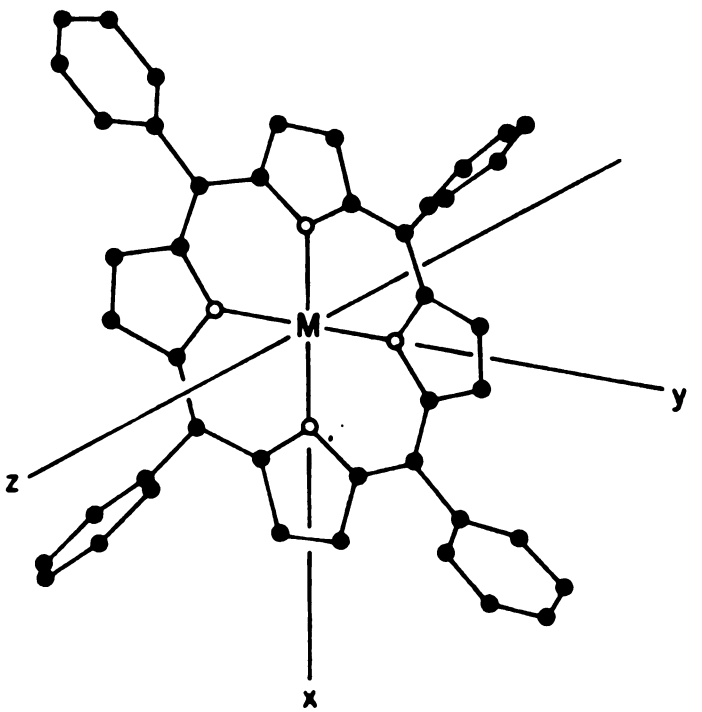


METALLO-TETRAPHENYLPORPHYRIN

$\alpha, \beta, \gamma, \delta$ meso-positions. Deuterporphyrin IX iron chloride has the same structure as hemin except that the 2,4 positions have hydrogen atoms instead of vinyl groups. The crystal-field parameter for these high-spin compounds has been measured and will be referred to later in the thesis.

The iron-porphyrins are of biological interest because they form the basic structure for the proteins myoglobin and haemoglobin. There are also several physical properties which make the metallo-porphyrins interesting. The presence of the unpaired electrons on the metal atom is attractive from a magnetic standpoint. In addition, the rather large molecular weight (greater than 400) allows for a magnetically dilute system. This magnetic dilution can be easily altered by the attachment of various ligands at the 1-8 positions and the meso positions. Also, the spin state of the metal atom can be changed by the bonding of various axial ligands. The lack of waters of hydration eliminates some of the storage and handling problems encountered with other dilute magnetic salts. In addition, the metallo-porphyrins are quite stable so that they can be heated to as much as 300°C without danger of decomposition of the individual molecules.

## B. Iron ($Fe^{3+}$) Tetraphenylporphine Chloride

### Molecular Structure

The structure of iron tetraphenylporphine chloride (FeTPPCl) is shown in Figure 7. The interesting features of this molecule stem from the iron and chlorine positions. The iron atom is out of the porphyrin plane with the chlorine atom bonded on the side of the iron away from this plane. The iron-chlorine bond is coincident with the c-axis of the crystal which is normal to the porphyrin plane. The FeTPPCl molecule has a molecular weight of 704 atomic units and has no waters of hydration.

To appreciate the magnetic behavior of FeTPPCl, it is essential to consider the bonding characteristics of the iron atom when placed in this molecule. Iron loses two 4s electrons and one of its 3d electrons as it becomes ionized in the bonding process. Two of these three electrons can be pictured as shared by the four porphyrin plane nitrogen atoms. The third electron is taken up by the chlorine atom. The remaining five 3d valence electrons give rise to the interesting magnetic properties. The crystalline electric field experienced by these electrons is axial. The two electrons shared by the nitrogens can be thought of as smeared out in a doughnut-like bonding arrangement in the x-y plane (porphyrin plane) with the largest electron density at the nitrogen sites. The chlorine atom provides a third negative charge above the iron ion on the z-axis. The electric field at the iron is thus very similar to that at the center of a

Figure 7. The molecular structure of iron tetraphenylporphine chloride. The iron ion is displaced out of the porphyrin plane by .383 Å. The chlorine ion is bonded above the iron ion along the z-axis away from the porphyrin plane.

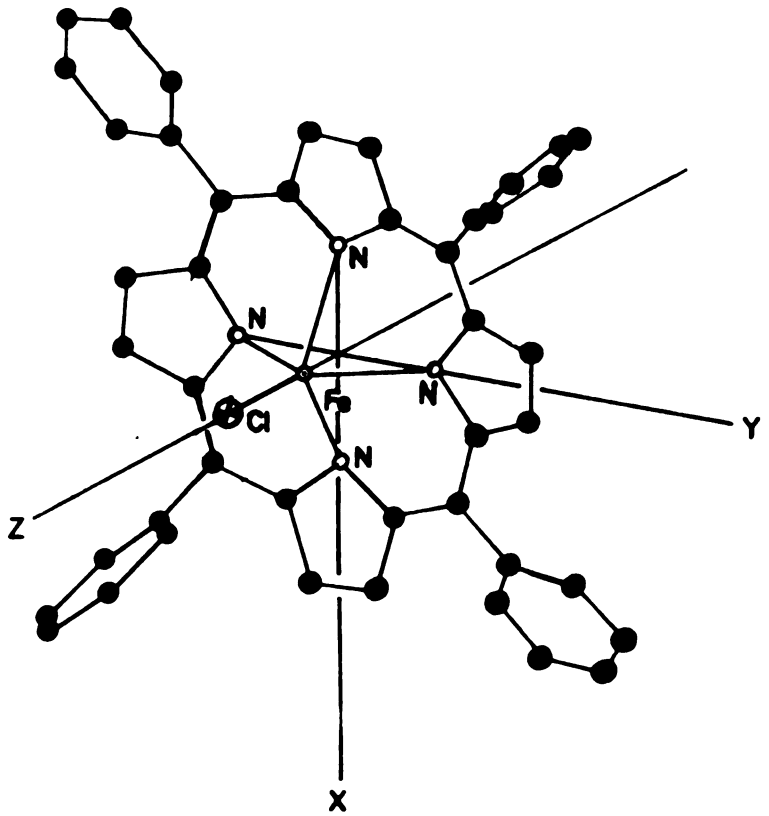


IRON-TETRAPHENYLPORPHYRIN CHLORIDE

square-based pyramid with 1/2 negative charges at the four corners of the base and one negative charge at the top. A consideration of the 3d orbitals will lead to a splitting in energy of these levels when placed in this environment. The angular dependence of the five orthogonal 3d wave functions (orbitals) is shown in Figure 8. The response of these orbitals to a crystal field of this symmetry is shown in Figure 9. The orbitals are classified into two groups based on the splitting caused by the presence of an octahedral crystal electric field. The $t_{2g}$ (sometimes called $d_\varepsilon$) group contains the $d_{xy}$, $d_{xz}$, $d_{yz}$ orbitals. The $e_g$ (or $d_\gamma$) group contains the $d_{z^2}$ and $d_{x^2-y^2}$ orbitals. This splitting is obvious since the $t_{2g}$ elements avoid the corners of an octahedron where the negatively charged ions would reside in an octahedral structure. Thus the $e_g$ group would have a larger energy due to the higher Coulomb repulsion experienced by the $d_{z^2}$ and $d_{x^2-y^2}$ lobes which point straight at the negative charges. The presence of a tetragonal distortion along the z-axis acts to split the $d_{xz}$ and $d_{yz}$ in energy from the $d_{xy}$ of the $t_{2g}$ set. Similarly $d_{z^2}$ will be split to a lower or higher energy than $d_{x^2-y^2}$ depending upon whether the distortion is an expansion or contraction along the z-axis. A rhombic distortion which destroys the four-fold symmetry in the x-y plane will further split the remaining $d_{xz}$ and $d_{yz}$ degeneracy.

The relative separation of the 3d orbitals is important in determining the spin state of the iron atom. In the free

Figure 8. The angular dependence of the d orbitals.

Figure 9. The splitting of the 3d orbital energies in crystalline field environments of different symmetry.

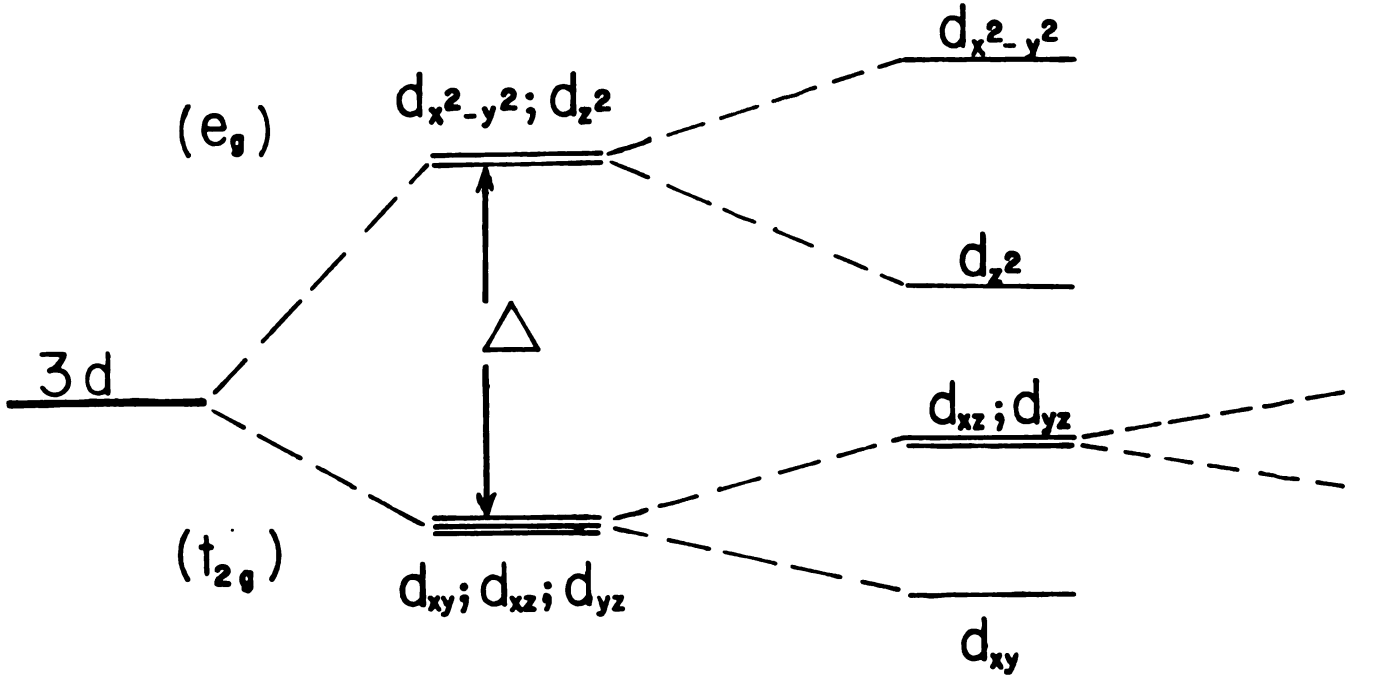
$d_{x^2-y^2}$
$d_{x^2-y^2}; d_{z^2}$
$(e_g)$
$d_{z^2}$
3d
$d_{xz}; d_{yz}$
$(t_{2g})$
$d_{xy}; d_{xz}; d_{yz}$
$d_{xy}$
FREE ION
OCTAHEDRAL
TETRAGONAL
RHOMBIC

ion Hund's rule dictates putting one electron in each orbital so as to overcome the repulsive interaction of two electrons occupying the same orbital. However, in the octahedral crystal environment, the energy difference $\Delta$ between the $t_{2g}$ and $e_g$ orbitals may be so large that the energy necessary to put a fourth electron into the $e_g$ orbital may be larger than the Coulomb repulsion experienced by placing another electron in one of the three singly occupied $t_{2g}$ orbitals. If this were the case, a "high-field" or low-spin material would result. The FeTPPCl system is a "low-field" or high-spin compound because the octahedral splitting, $\Delta$, is not so large. It is still energetically advantageous to put one electron into each of the five orbitals so as to have five unpaired spins. This results in a high-spin compound. The tetragonal distortion and slight rhombic distortion of FeTPPCl thus give rise to five orbitals all of slightly different energy which can be treated as an effective spin-5/2 system. Because each of the five orbitals contains an electron, the electron distribution looks spherical and the orbital angular momentum has a value of zero for the $Fe^{3+}$ ion. The orbital ground state ($^6A_1$) is thus regarded as an S state ($\ell$=0) spin sextet. (Since S = 5/2, the spin multiplicity is 2S+1 = 6.)

The presence of the higher orbital excited states is particularly important to the magnetic properties of the iron 3d electrons in FeTPPCl. This comes about through a consideration of the spin-orbit coupling between the

intrinsic spins of the 3d electrons and their own orbital angular momentum. As just mentioned, the ground state orbital angular momentum is zero, and this might suggest zero coupling. However, the excited orbital states give rise to an important contribution to the spin-orbit coupling when second-order perturbation theory is applied. For the tetragonal distortion of the square pyramidal FeTPPCl molecule, the excited orbital quartet states are important. A quartet state has a spin of 3/2 (spin multiplicity 2S+1 = 4) such that two of the five 3d spins have paired up leaving only 3 unpaired spins. There are actually three different quartet states which provide non-zero matrix elements of the orbital angular momentum to the ground state. One has the $d_{xy}$ orbital filled ($^4A_2$), one has the $d_{xz}$ orbital filled ($^4E_{xz}$), and the other has the $d_{yz}$ orbital filled ($^4E_{yz}$).[20] (The $^4A_2$ state lies closest to the $^6A_1$ ground state, being only .26 eV higher in energy.[20]) The presence of these quartets give rise to a non-zero spin-orbit coupling when second-order perturbation theory is applied with the spin-orbit term as the perturbation. The resultant spin Hamiltonian for the axial symmetry displayed by FeTPPCl is[21]:

$$H = D_c \left[S_z^2 - \tfrac{1}{3} S(S+1)\right] \qquad (13)$$

where $D_c$ is the crystal-field parameter which is proportional to the orbital angular momentum matrix elements between the sextet ground state and the quartet excited states. $S$ is the total spin quantum number ($S = 5/2$ for FeTPPCl) and $S_z$ is the z-component operator of the total

spin. The z-axis is defined by the normal to the porphyrin plane. When rhombic distortion is present, there is an additional term in the spin Hamiltonian $E_c(S_x^2 - S_y^2)$ which is believed to be quite small ($E_c < .01\ D_c$) for similar metalloporphyrin complexes.[22]

The crystal-field parameter, $D_c$, has been measured by Richards and co-workers[23] for a number of Fe-Cl porphyrins (Protoporphyrin IX iron chloride and Deuteroporphyrin IX iron chloride among others) using infra-red absorption techniques. They found $D_c$ to be in the range 7 $cm^{-1}$ (10 K) to 9 $cm^{-1}$ (13 K). The value for $D_c$ to be used in this thesis is 13 K (9 $cm^{-1}$), which is within the range of accepted values for iron-chloride porphyrins. The exact value of $D_c$ within a range from 10 K (7 $cm^{-1}$) to 17 K (11.8 $cm^{-1}$) has very little effect on the results to be presented. The important point to be stressed is that this crystal-field parameter is much larger than the exchange interaction to be presented later. Hence the effect of $D_c$ comes in only to higher order in the exchange-split ground state energies.

The effect of the crystal-field parameter, $D_c$, is to cause a zero field splitting of the spin-5/2 sextet. For positive $D_c$ (as measured for the iron-chloride porphyrins) the $\pm$ 1/2 state is lowest at an energy 2 $D_c$ below the $\pm$ 3/2 state. The $\pm$ 5/2 state is the highest at an energy of $4D_c$ above the $\pm$ 3/2 state. When a magnetic field is applied, each of these doublets is split in energy. The

spin Hamiltonian then takes the form

$$H = D_c[S_z^2 - \tfrac{1}{3} S(S+1)] + g_{||}\ \mu_B\ H_o \cos\theta\ S_z$$

$$+ g_{\perp}\ \mu_B\ H_o \sin\theta\ S_x \qquad (14)$$

where $H_o$ is the magnetic field applied in the x-z plane at an angle $\theta$ to the crystalline c-axis; $S_x$ and $S_z$ are the x and z component spin-5/2 operators; $g_{||}$ relates the z-component of magnetic moment to the z-component of the angular momentum (in this case spin only); $g_{\perp}$ relates the component of magnetic moment in the x-y plane to the x-y component of angular momentum; and $g_{||} = g_{\perp} = 2.00$, the free-electron g value. For FeTPPCl, $D_c/k_B \approx 13$ K, and the largest ESR fields employed are 10 kG ($\approx$ 1 K). Thus, since $2D_c >> \mu_B H_o$, one chooses $|+1/2>$, $|-1/2>$, $|+3/2>$, $|-3/2>$, $|+5/2>$, $|-5/2>$ as the basis states, where the c-axis (i.e. the normal to the porphyrin plane when the molecules stack in the crystal) represents the z-axis of spin quantization. Now if one solves the Hamiltonian in equation 14 for the energy eigenvalues using this basis set, the degenerate ground state of $|\pm 1/2>$ is split by the magnetic field. The result of this calculation can be expressed in terms of an anisotropic g factor of the form:

$$g_{eff} = [g_{||}^2 + (9g_{\perp}^2 - g_{||}^2)\sin^2\theta]^{\frac{1}{2}}\ [1 + 2\left(\frac{g_{\perp}\mu_B H_o}{2\ D_c}\right)^2\ F(\theta)] \qquad (15)$$

$$F(\theta) = 4\sin^2\theta\ \left(\frac{g_{||}^2 + (9g_{\perp}^2/4 - g_{||}^2)\sin^2\theta}{g_{||}^2 + (9g_{\perp}^2 - g_{||}^2)\sin^2\theta}\right) \qquad (16)$$

Thus, for the case when $2D_c >> \mu_B H_o$ , the g factor varies from $g_{eff\ ||} = g_{||} = 2.00$ for $\theta = 0°$ to $g_{eff\ \perp} = 3g_{\perp} = 6.00$ for $\theta = 90°$. This is the result of a perturbation calculation on the 2x2 ground state subspace of $|+1/2>$, $|-1/2>$ ; and thus is good at low temperatures where $k_B T << D_c$ . Hence, the iron ion in FeTPPCl may be treated at low temperatures as having an effective spin of 1/2 with a highly anisotropic g value. At high temperatures ($k_B T >> D_c$) , the iron ion acts like a normal spin of 5/2 with an isotropic g factor of 2.00. These low temperature $g_{eff}$ values are consistent with the single crystal and powder ESR measurements to be presented at the end of this chapter for FeTPPCl.

This summarizes the most important terms in the spin Hamiltonian for an isolated FeTPPCl molecule.

Crystal Structure

The original X-ray diffraction work on the structure of FeTPPCl was done by Fleischer et al.[24] and was re-interpreted by Hoard, Cohen, and Glick.[25] These results yield a body-centered tetragonal unit cell with dimensions a=b= 13.53 Å and c=9.82 Å . There are two molecules per unit cell. The density is 1.31 gm/cm$^3$, and the space group for the statistically averaged molecule is I 4/m - $C_{4h}$ . Of particular interest is the result that the iron ion lies either above or below the porphyrin plane by .383 Å with an apparent equal probability. The chlorine is always bonded on that side of the iron which is away from the

porphyrin plane. The FeTPPCl molecule shown in Figure 7 is based on this X-ray work.

To appreciate the existence of superexchange pairs, it becomes necessary to consider the ionic radii of the $Fe^{3+}$ ion and the $Cl^-$ ion when present in the FeTPPCl crystal lattice. The $Fe^{3+}$ ionic radius is 0.64 Å and the $Cl^-$ radius is 1.81 Å.[26] Two primitive cells are shown in Figure 10 with all the relevant distances. The porphyrin planes are represented by small squares drawn around each lattice point and are not drawn to scale. The phenyl rings are also not shown. They point neither along the crystalline axes nor along the diagonals but are oriented so as to avoid overlap with phenyl rings from adjacent molecules. The Fe-Cl bond lengths and other vertical dimensions are drawn to scale to emphasize the existence of pairs. It is easily seen that if two chlorine ions from adjacent molecules are at their closest possible approach to each other, then no other chlorine neighbor can be this close. The exchange path now becomes obvious. The iron 3d orbitals overlap with the chlorine 3p orbitals within the FeTPPCl molecule. (The exact mixing of the Fe-Cl orbitals is not clear and would provide for an interesting theoretical calculation. It is felt that the iron $3d_z^2$ and chlorine $3p_z$ orbitals contribute strongly to the intra-molecular exchange.) In addition, these chloride ions provide an electronic superexchange path via weak overlap of $Cl^-$ $3p_z$ orbitals. Hence, there is a superexchange pairing of the iron unpaired electronic spins on one FeTPPCl molecule with those on an adjacent molecule

Figure 10. Diagram of two body-centered tetragonal unit cells of the FeTPPCl crystal structure. The unit cells are drawn to scale only along the c-axis. The spheres representing the ionic radii are drawn to scale.

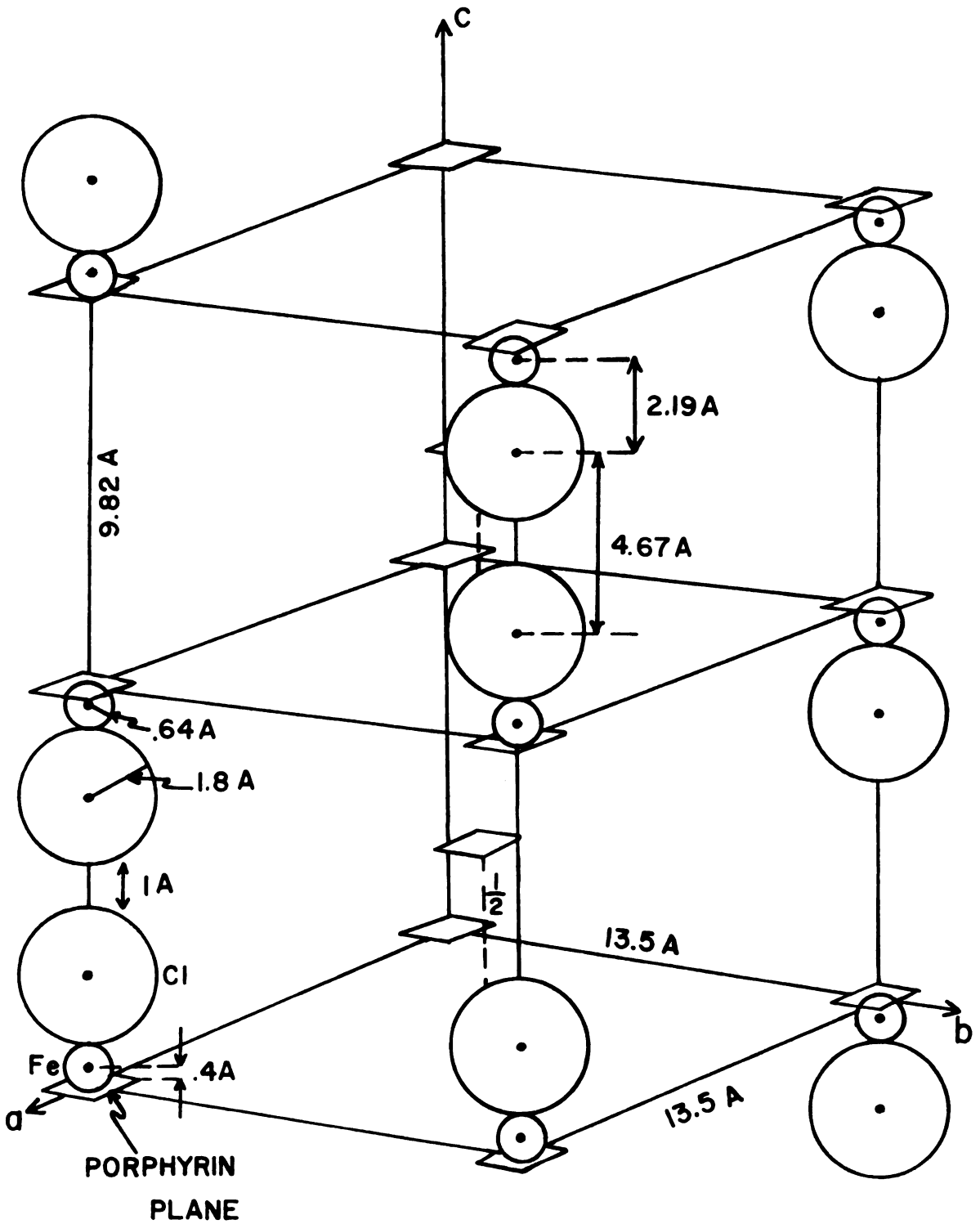
C
9.82 A
2.19 A
4.67 A
.64 A
1.8 A
1 A
Cl
Fe
.4A
a
PORPHYRIN
PLANE
1/2
13.5 A
13.5 A
b

through the chloride ions: Fe-Cl---Cl-Fe. The chlorine $3p_z$ orbital extends quite far into space with an exponential decrease allowing for a small overlap between the neighboring chlorines. (Based on theoretical calculations of Butterfield and Carlson[27], the charge density 1 Å out from the ionic radius of the $Cl^-$ ion is approximately 2% of the value at the ionic radius. The ionic radius for chlorine is so defined that one electron charge lies outside a sphere of such radius.) Whenever two chlorines of adjacent molecules are not at the closest approach, there is no superexchange path, and these FeTPPCl molecules act as isolated magnetic molecules in the lattice. (They are isolated to the extent that the classical dipole-dipole coupling can be ignored.) Thus there is a unique dual system in which there is a combination of isolated exchange pairs and isolated individual magnetic molecules.

Crystal Growth

The study of FeTPPCl necessitated the growing of a single crystal. This turned out to be a difficult undertaking, eventually yielding only one usable crystal. The crystal growth technique employed was to dissolve some FeTPPCl powder obtained from the Strem Chemical Company[28] into a solvent in which it was soluble. Then a second solvent, in which the FeTPPCl was rather insoluble, was added. The soluble solvent was chosen such that it had a higher evaporation rate than the insoluble one. The resultant solution was allowed to sit until enough of the more

volatile solvent evaporated to cause a precipitation of the FeTPPCl.

Approximately 30 mgm of FeTPPCl powder was added to 150 ml of chloroform in which the FeTPPCl dissolved quite easily. Methyl alcohol was then added in quantities ranging from 10 ml to 150 ml depending on the desired ratio of chloroform to methyl alcohol. The FeTPPCl was rather insoluble in the methanol which had a much lower evaporation rate than the chloroform. This solution was then filtered through a sintered glass funnel containing 200 mesh activated alumina. The alumina had been previously heated at 150°C for several hours to drive off any water which may have been present. The filtered solution was then poured into several small beakers and wide-mouthed bottles and covered with parafilm. The parafilm is somewhat permeable to organic vapors and thus it allows a slow evaporation of the chloroform leaving behind a methanol rich solution. Tiny holes were poked in the parafilm covers of some solutions to increase the evaporation rate. The FeTPPCl eventually precipitated out of the solution. The result was generally a mass of small micro-crystals or polycrystalline chunks. The evaporation rate seems to be the critical factor and should be made as small as possible. This method gave several regularly shaped micro-crystals, but none had an external morphology that would have allowed a simple alignment for X-ray verification. Several of these small crystals were used as seed crystals in other

chloroform-methanol-FeTPPCl solutions, but no usable crystals ever resulted.

A second set of solvents were dichloromethane and hexane. 30 mgm of FeTPPCl powder was placed in a beaker with 150 ml of dichloromethane in which the FeTPPCl was very soluble. 300 ml of hexane was added and the resultant solution was stirred with a glass rod. The FeTPPCl is insoluble in the hexane. This solution was then filtered and approximately 50 ml was placed in a small wide-mouthed bottle. The plastic cap for this bottle had a single .034 cm diameter hole drilled through it. The cap was placed on the bottle, and the solution was set aside at room temperature. One month later several small micro-crystals were observed. Upon observation under an 8X microscope one small crystal had a very regular cubic shape with a somewhat mis-shapen top. The top was believed to have broken off when the crystal was removed from the side of the growth bottle. This micro-crystal was approximately cubic of side .04 cm as measured with a travelling microscope. The mass was measured with a Mettler balance to be .00010 gm. These values are compatible with the reported density of 1.31 $gm/cm^3$. It was handled using the tip of a syringe while viewed under a microscope. A diagram of the crystal is shown in Figure 11.

It was decided to mount this crystal and perform the X-ray diffraction to check its single-crystal character. The X-ray work was done using a GE XRD-5 X-ray diffractometer with a Molybdenum source tube. The lattice dimensions of

Figure 11. Diagram of 0.1 mgm FeTPPCl single crystal.

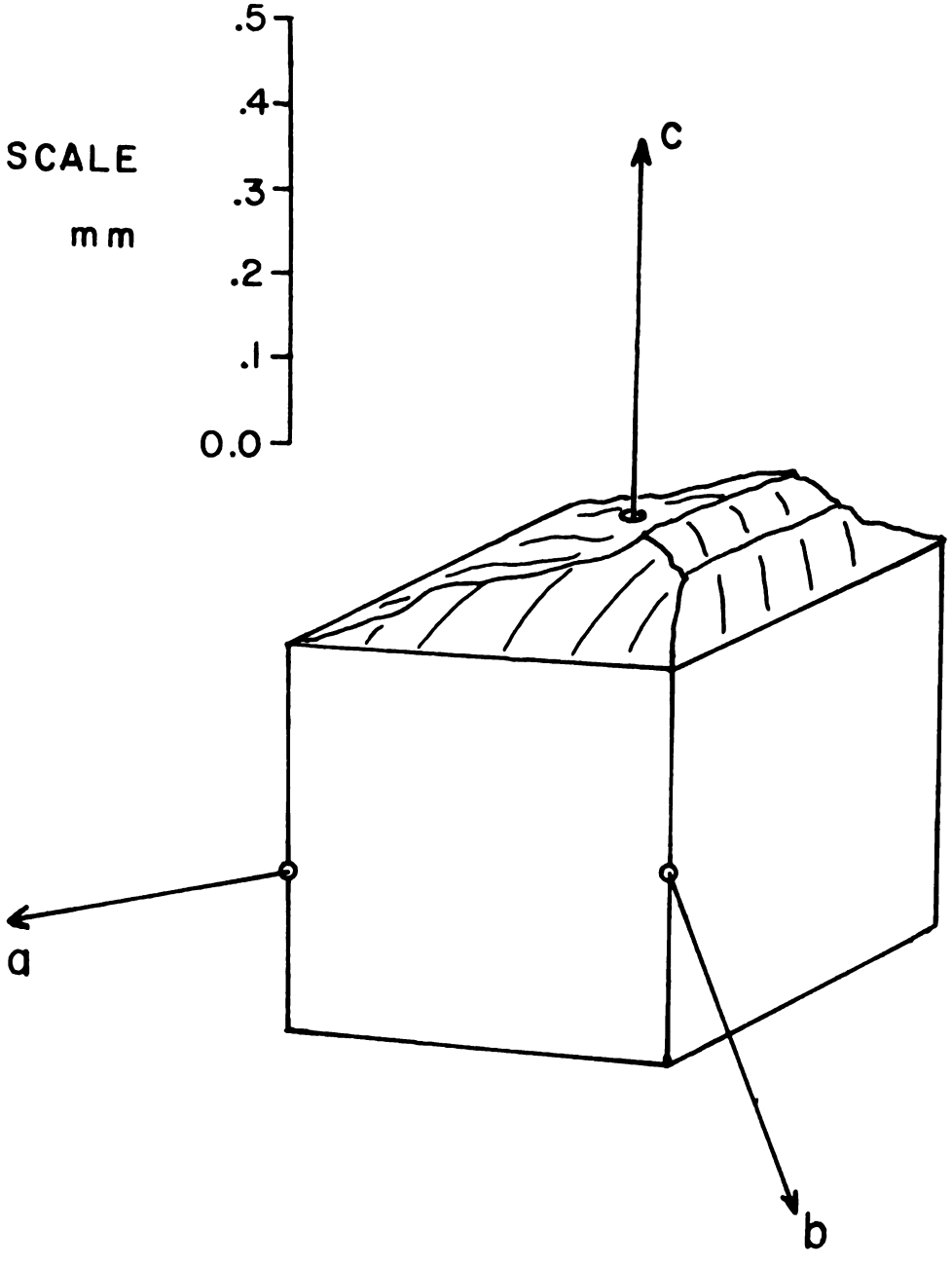
SCALE
mm
.5
.4
.3
.2
.1
0.0
c
a
b

a=b= 13.5 Å and c= 9.8 Å were verified. The I 4/m symmetry was also verified using No. 87 of the International Tables of crystal structures. The crystal was oriented via a goniometer situated in the center of the diffractometer so that sweeps through three mutually perpendicular crystal directions were easily made. The reciprocal space plot of the diffracted intensity maxima yielded the above information thus confirming the single crystal character of the micro-crystal.

The electron spin resonance (ESR) of this small crystal was now undertaken. The crystal was mounted in an epoxy holder of dimensions such that it could eventually be placed directly into the SQUID sample chamber on the dilution refrigerator. The crystal and holder were then placed in a cylindrical X-band ESR cavity and aligned so that the external DC magnetic field could be rotated in the a-c crystal plane. The cavity was placed in a Helium-4 cryostat, and an ESR spectrum was obtained at a temperature of 4.2 K. The frequency was measured to be 9.22 GHz which correlated with the position of the DPPH line. The derivative detection signal was recorded as the magnetic field was swept from 0 to the 5 kilogauss range. The field was rotated from 0° to 90° at 10° intervals with respect to the aligned crystalline c-axis, and an intensity vs field trace was obtained at each angle. The result was a single absorption line which "moved" in field as the angle between the field and the c-axis of the crystal was varied. The minimum

g value obtained from this rotation was $g_{||} = 2.25 \pm 1\%$ and the maximum value was $g_{\perp} = 6.04 \pm 2\%$. The rather large deviation of the $g_{||}$ value from 2.00 was due to misalignment of the crystalline c-axis in the ESR cavity. The c-axis happens to pass through the mis-shapen top of the crystal which makes alignment along this axis difficult.

The purpose of this ESR run was to provide further confirmation of the single crystal nature of the sample crystal as well as to verify the $g_{||} = 2$ , $g_{eff\perp} = 6$ axial behavior of this high-spin metallo-porphyrin. At the time of this run, the existence of pairs was not suspected. Thus only measurements at 4.2 K were taken, since they gave the expected information concerning the g values for such a high-spin system. No pair structure for this small crystal was observed since the pair transitions are much weaker. Later, after the single crystal magnetic susceptibility measurements were made, it became evident that exchange pairing might be occurring; and more detailed ESR investigations at 1 K were undertaken to verify this. (The signals are much larger at 1 K due to the larger number of spins being in the ground state.) The ESR pair results will be discussed later.

Two other ESR runs were undertaken to observe the $g_{||} \simeq 2.00$ signal. A single crystal run gave a $g_{||} = 2.10$ which indicated only a 6.5° misalignment from the c-axis. However, it became obvious that, without an adjustable goniometer mounted in the ESR cavity, an exact alignment

along the c-axis would be impossible. Hence a powder run was done. (The later powder run was completed after the susceptibility and heat capacity measurements. Even at 4.2 K, the larger mass powder sample gave evidence of the pairing.) Because of the averaging over all possible crystallite orientations in a powder, the $g_{\perp}$ powder peak was shifted away from the 6.0 value as was the $g_{||}$ value step shifted from the 2.0 value. To interpret this data the line shape analysis of Ibers and Swallen[29] was used. This analysis applies to an axially symmetric system and assumes a Lorentzian line shape. A computer program was written to apply the expressions given in this article. Since the actual line shapes are more Gaussian than Lorentzian, it was necessary to use smaller values for the line width in the computer calculation than were measured from the single crystal runs. This is because a Lorentzian distribution function falls off less rapidly as one goes away from the center of the peak. The Gaussian function is, in general, more sharply peaked. For a good comparison of the two distribution functions one is referred to the book by Bevington.[30] The results for a Lorentzian line width of 50 gauss, $g_{||} = 2.00$, and $g_{eff\perp} = 6.00$ gave a powder intensity curve very similar to that observed experimentally. From this analysis it was concluded that a $g_{||}$ value of 2.00 was consistent with our powder data.

The single crystal rotation diagram for the isolated single FeTPPCl molecules is given in Figure 12. This curve

Figure 12. Angular dependence of the $g_{eff}$ value for the non-interacting (neglecting dipolar coupling) single FeTPPCl molecules. The abscissa gives the angle at which the magnetic field was oriented from the lab z-axis. The effect of a 10° misalignment between the crystalline c-axis and the lab z-axis is also included. The crosses, + , represent the experimental data, and the smooth curve represents the theoretical expression given in equation 18.

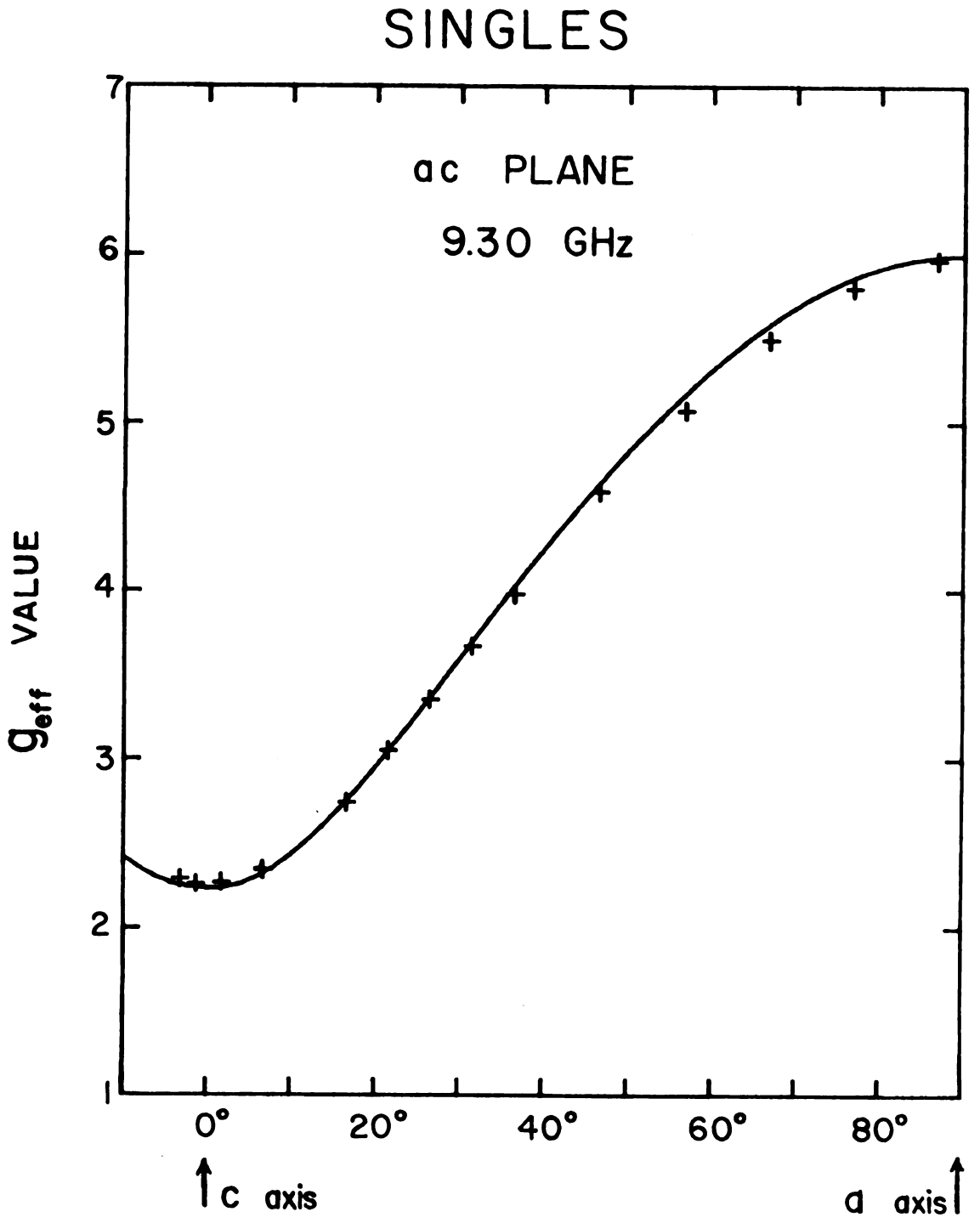
SINGLES
ac PLANE
9.30 GHz
$g_{eff}$ VALUE
7
6
5
4
3
2
1
0°
20°
40°
60°
80°
c axis
a axis

was obtained at a later data when investigating the pair structure at 1 K. It is presented here as evidence for the isolated singles because the magnetic field values for this run were the most accurately measured. The field sweep was stopped at the center of each derivative line, and the field was measured using a rotating coil gaussmeter. A theoretical calculation of the ground state energy splitting of the $S_z = \pm 1/2$ state was done as a function of angle, $\theta$, from the crystalline c-axis using the spin Hamiltonian given earlier in equation 14. Now, however, the fact that the lab frame z-axis could be misaligned from the crystalline c-axis by an arbitrary angle, $\delta$, was included. The calculated splitting is related to the $g$ value for an effective spin-1/2 system by the formula:

$$\Delta E = E_{+\frac{1}{2}} - E_{-\frac{1}{2}} = g_{eff}\, \mu_B\, H_o \tag{17}$$

The resultant $g$ factor, including misorientation, is given by:

$$g_{eff} = [g_{||}^2 \Phi^2 + 9 g_{\perp}^2 \Psi^2]^{\frac{1}{2}} \left[1+2\left(\frac{g_{\perp}\mu_B H_o}{2 D_c}\right)^2 \Psi^2 \times \left(\frac{4\Phi^2 + 9\Psi^2}{\Phi^2 + 9\Psi^2}\right)\right] \tag{18}$$

$$\Phi = \cos\delta \cos\theta \tag{19}$$

$$\Psi = [\sin^2\theta + \sin^2\delta \cos^2\theta]^{\frac{1}{2}} \tag{20}$$

where $g_{||} = g_{\perp} = 2$, the free electron g value; $\theta$ is the angle between the magnetic field, $H_o$, and the z-axis in the lab frame; $\delta$ is the misalignment angle between the crystalline c-axis and the lab frame z-axis; $D_c$ is the crystal electric field parameter; and $\mu_B$ is the Bohr magneton. The computed theoretical curve, based on equation 18 with a misalignment of 10° ($\delta$=10°), is shown superimposed on the experimental data in Figure 12. The existence of a system of isolated spin-5/2 molecules with axial symmetry is thus readily confirmed.

# CHAPTER III

## THE MAGNETIC SUSCEPTIBILITY OF IRON TETRAPHENYLPORPHINE CHLORIDE

As was pointed out in Chapter II, the dominant term in the spin Hamiltonian for the $Fe^{3+}$ ions in FeTPPCl is the second-order spin-orbit coupling to the higher energy crystal-field-split orbitals. As mentioned before, the net effect of such a crystal-field spin-orbit term at low temperatures ($T << D_c/k_B$) is to reduce the spin-5/2 system to an effective spin-1/2 system with a $g_{||} = 2$ and a $g_{eff\ \perp} = 6$. Thus, at these temperatures, the Hamiltonian can be characterized by a Zeeman term (when a magnetic field is present) with a highly anisotropic g factor, plus other small energy terms. These other terms are a result of such interactions as hyperfine, superhyperfine (transferred hyperfine), classical dipole-dipole, and very weak superexchange.

The Hamiltonian containing the relevant interactions which might govern the low temperature magnetic behavior of FeTPPCl is given by:

$$\mathcal{H} = \sum_i \Big\{ \underset{\sim}{S}_i \cdot \underset{\approx}{g} \cdot \underset{\sim}{H} + \underset{\sim}{S}_i \cdot \underset{\approx}{A}_{Fe} \cdot \underset{\sim}{I}_{Fe} + \sum_j{}' \underset{\sim}{S}_i \cdot \underset{\approx}{J}_{ij} \cdot \underset{\sim}{S}_j$$

$$+ \sum_j{}' (1/r_{ij}^3)[\underset{\sim}{\mu}_i \cdot \underset{\sim}{\mu}_j - 3(\underset{\sim}{\mu}_i \cdot \hat{\underset{\sim}{r}}_{ij})(\underset{\sim}{\mu}_j \cdot \hat{\underset{\sim}{r}}_{ij})] + \sum_{j=1,4} \underset{\sim}{S}_i \cdot \underset{\approx}{A}_N^{(j)} \cdot \underset{\sim}{I}_N^{(j)}$$

$$+ \underset{\sim}{S}_i \cdot \underset{\approx}{A}_{Cl} \cdot \underset{\sim}{I}_{Cl} \Big\} \qquad (21)$$

The first term on the right represents the Zeeman term where $\underset{\approx}{g}$ is the anisotropic g tensor. The second term is the hyperfine interaction between the spin $\underset{\sim}{S}_i$ on the $^{57}Fe$ atom and the nuclear spin of the $^{57}Fe$ nucleus. (The more abundant $^{56}Fe$ isotope has a zero nuclear spin.) Since only 2% of the naturally occurring iron is $^{57}Fe$, this term can be neglected. The third term is the exchange term written in the Heisenberg formulation. In practice, only nearest neighbor exchange is important, and in FeTPPCl only isolated superexchange pairs contribute, so that this term will become greatly simplified. The fourth term represents the classical dipole-dipole coupling between two magnetic moments $\underset{\sim}{\mu}_i$ and $\underset{\sim}{\mu}_j$ separated by a distance $r_{ij}$. The fifth and sixth terms represent the superhyperfine coupling between the unpaired iron electrons and the nuclei of the surrounding intra-molecular neighbors. In the case of FeTPPCl, there are the 4 nitrogen nuclei ($I_N=1$) of the porphyrin plane and the chlorine nucleus ($I_{Cl}=3/2$) above the iron. The superhyperfine coupling to the nitrogen nuclei has been measured to be only .4 mK for the related material hemin.[22] The iron-fluorine superhyperfine coupling was measured by Morimoti and Kotani[31] for myoglobin fluoride to be as large as 6 mK. Since the halogen-iron-porphyrin plane structure is the same, the iron-chlorine transferred hyperfine interaction is assumed to be of the same order. For a high-spin material with such a highly anisotropic g factor, the largest classical dipolar coupling is in the perpendicular

direction. It can be approximated by

$$D_d \simeq g^2_{eff\perp} \mu_B^2 / r_{ij}^3 \qquad (22)$$

where $g_{eff\perp} = 6$ , $\mu_B$ is the Bohr magneton, and $r_{ij}$ is nearest neighbor distance. For FeTPPCl, the coupling constant has the value: $D_d/k_B \simeq 24$ mK. Thus for the Hamiltonian in equation 21, we are left with only three significant terms: Zeeman, superexchange, and classical dipole-dipole. The superexchange term will be shown to clearly dominate the classical dipolar coupling.

A convenient way to observe the low temperature behavior of such weak systems is to measure the temperature dependence of the zero-field magnetic susceptibility. In its tensor form, the zero-field susceptibility is given by:

$$\underset{\approx}{\chi}(T) = \lim_{H \to 0} \frac{\partial \underset{\sim}{M}}{\partial \underset{\sim}{H}} \qquad (23)$$

The magnetization, $\underset{\sim}{M}$ , is obtained from the statistical mechanical partition function according to the relation:

$$\langle M_i \rangle = \left(\frac{1}{V}\right) k_B T \frac{\partial}{\partial H_i} (\ln Z) \qquad (24)$$

where $Z$ is the partition function, $H_i$ is the ith component of the applied field, $T$ is the absolute temperature, $V$ is the volume of the material, $k_B$ is the Boltzmann constant, and $\langle M_i \rangle$ is the thermal average of the ith component of the

magnetization. The partition function is given by:

$$Z = \text{trace } e^{-H/k_B T} = \sum_i e^{-\varepsilon_i/k_B T} \tag{25}$$

where $H$ is the Hamiltonian, and $\varepsilon_i$ are the energy eigenvalues. Thus, the partition function can be obtained, in principle, once the energy levels are obtained by a diagonalization of the Hamiltonian. Of course, if all the terms in the Hamiltonian of equation 21 are very small compared to $k_B T$, then the susceptibility has a simple Curie behavior:

$$\chi_i = C_i/T \tag{26}$$

where $C_i$ is the Curie constant along the ith crystalline direction.

For comparison purposes as to what $\chi$ would do if only the Zeeman and dipole-dipole terms of equation 21 were important, Van Vleck[32] treated the case of a system of magnetic dipoles in a perturbation expansion. He showed that the magnetization should have the form:

$$M_i = (C_i H_i/T)\ (1 - \frac{C_i}{T}\ \Phi_i)^{-1} \tag{27}$$

where $C_i$ is the Curie constant; $H_i$, the applied field; and $\Phi_i$, the lattice sum along the ith crystalline direction. The susceptibility for an axially symmetric system follows and is given by Daniels[33] in the Curie-Weiss formulation as:

$$\chi_{||} = \frac{C_{||}}{T-\Delta_{||}} \tag{28}$$

$$\chi_{\perp} = \frac{C_{\perp}}{T-\Delta_{\perp}} \tag{29}$$

$$\Delta_{||} = -(C_{||}/N) \sum_{j}{}' (1/r_{ij}^5)(r_{ij}^2 - 3\, z_{ij}^2) \tag{30}$$

$$\Delta_{\perp} = -(C_{\perp}/N) \sum_{j}{}' (1/r_{ij}^5)(r_{ij}^2 - 3\, x_{ij}^2) \tag{31}$$

where $N$ is Avogadro's number; $r_{ij}$ is the distance from the point at which the sum is being evaluated to the jth lattice site; $x_{ij}$ and $z_{ij}$ are the x and z-components of this distance; and $T$ is the absolute temperature. For the FeTPPCl system, the Curie constants are given by:

$$C_{||} = N\, g_{||}^2\, \mu_B^2/(4k_B) = .375\ \frac{\text{emu}}{\text{mole}\cdot\text{K}} \tag{32}$$

$$C_{\perp} = N(g_{\text{eff}\perp})^2\ \mu_B^2/(4k_B) = 3.38\ \frac{\text{emu}}{\text{mole}\cdot\text{K}} \tag{33}$$

The lattice sums in equations 30 and 31 were evaluated for the FeTPPCl system using a computer generated lattice. The out-of-planarity of the iron ion was taken into account by using a random number generator to put the iron ion on one side or the other of the lattice site by .383 Å. Then the distances from the origin to all the nearest neighbors were evaluated using a convergence factor proposed by J. R. Peverley.[34] This was done for 10 random lattices, and the average parallel and perpendicular sums were obtained to yield the following values for the Curie-Weiss constants:

$$\Delta_{||} = - 0.8 \quad mK$$

$$\Delta_{\perp} = +3.6 \quad mK$$

Based on these sums, it was determined that the perpendicular susceptibility should start to show a few percent deviation from a Curie law relationship at a temperature of about .125 K. The fact that the FeTPPCl powder susceptibility exhibits a marked deviation from Curie's law even at 1 K indicates that a spin-spin interaction larger than the classical dipole coupling is needed.

At this point, the single crystal of FeTPPCl was grown, and its susceptibility was measured both parallel and perpendicular to the crystalline c-axis in two separate runs. The ESR had been done on this single crystal mounted in the same epoxy holder that was inserted in the SQUID port for obtaining the susceptibility. As mentioned earlier, it was impossible to align the c-axis exactly so that the 10° misalignment from the c-axis indicated by the ESR data was also present in this parallel susceptibility run. The powder and single crystal measurements were made to as low as 5 mK. These data are given in Tables A2-A4 in the Appendix. The high temperature (i.e. T > .1 K) single crystal data are shown in Figure 13 along with the best-fit theoretical curves to be discussed shortly.

The high temperature behavior of $\chi_{||}$ and $\chi_{\perp}$ provided additional evidence to the powder data for the presence of an interaction much stronger than the classical dipolar

Figure 13. Temperature dependence of the molar susceptibility from a single crystal of FeTPPCl. The susceptibilities $\chi_{\parallel}$ and $\chi_{\perp}$ were measured, respectively, with the magnetic field at 10° and 90° with respect to the c-axis of the crystal. The smooth curves represent the theoretical fit to the data.

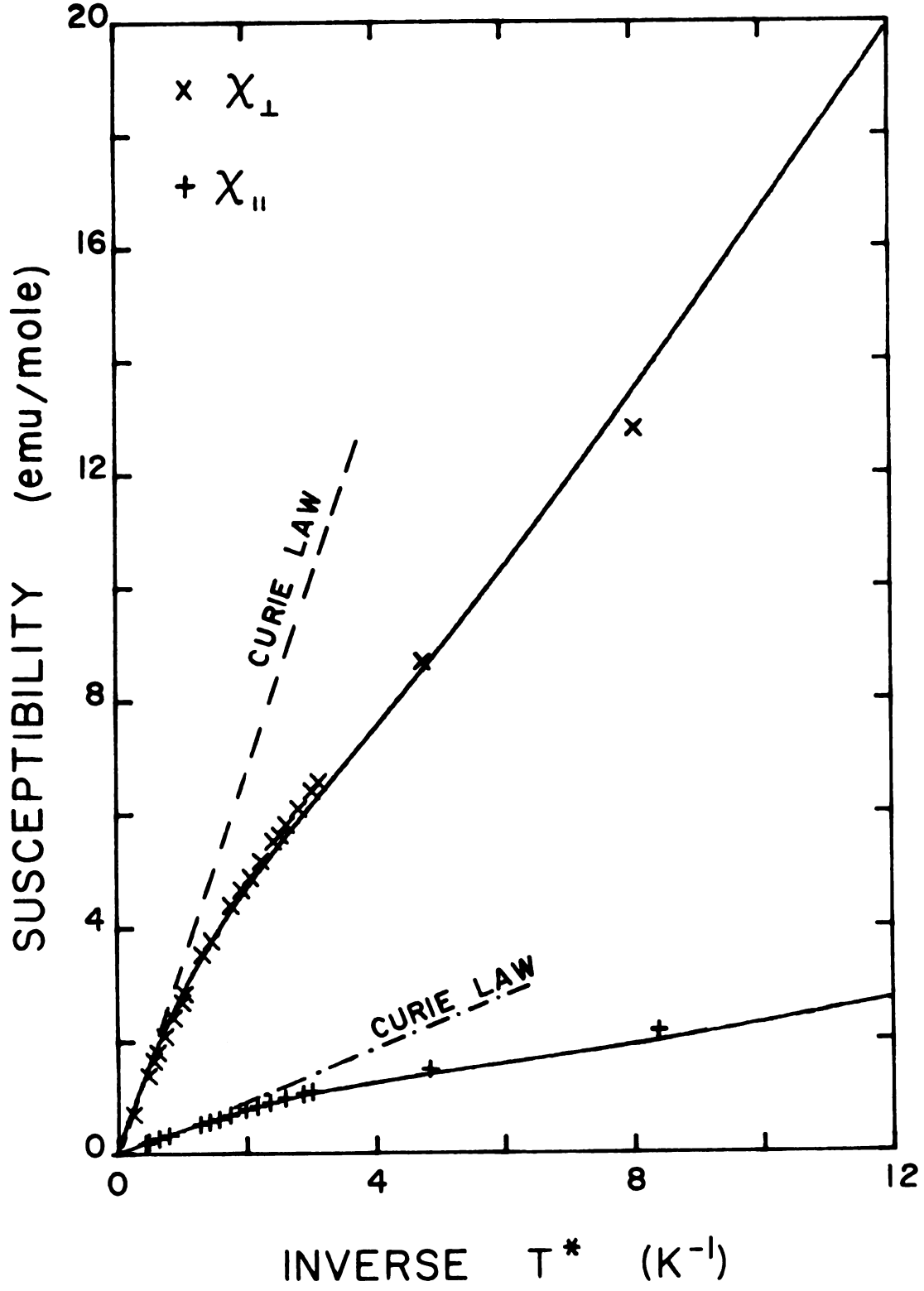
20
16
12
8
4
0
0
4
8
12
× $\chi_\perp$
+ $\chi_\parallel$
CURIE LAW
CURIE LAW
SUSCEPTIBILITY (emu/mole)
INVERSE T* ($K^{-1}$)

coupling. When the ionic radii of the iron and chloride ions are considered in conjunction with the Fe displacement from the porphyrin plane, the possibility of superexchange pairing becomes quite evident as shown in Chapter II.

The Superexchange-pair Hamiltonian

The superexchange pairing has been represented by an anisotropic Heisenberg model chosen to reflect the single ion axial symmetry. The exchange Hamiltonian for consideration is then:

$$H_{pair} = -J_{||} (S_{1z}S_{2z}) - J_{\perp} (S_{1x}S_{2x} + S_{1y}S_{2y}) \quad (34)$$

where $J_{||}$ is the superexchange parameter governing the z component spin coupling between the members of the pair, and $J_{\perp}$ is the superexchange parameter for the x and y component spin-coupling. $\underset{\sim}{S}_1$ and $\underset{\sim}{S}_2$ are true spin-5/2 operators. At the low temperatures of interest ($kT<<D_c$), the superexchange coupling represents a perturbation on the $S_z = \pm 1/2$ ground state of the spin-orbit crystal-field term. Thus one could treat $\underset{\sim}{S}_1$ and $\underset{\sim}{S}_2$ as effective spin-1/2 operators. The result is only a re-definition of $J_{\perp}$:

$$J_{\perp}^{(1/2)} = 9J_{\perp}^{(5/2)} \quad (35)$$

For the perturbation calculation to be mentioned, $\underset{\sim}{S}_1$ and $\underset{\sim}{S}_2$ are treated exactly as spin-5/2 operators.

For the sake of completeness, two other higher order exchange terms have been investigated. The biquadratic

exchange term[35] $-j(\vec{S}_1 \cdot \vec{S}_2)^2$ allows for magnetic striction and/or a combination of $\sigma$ and $\pi$ electron transfer in the superexchange mechanism. Since the exact exchange mechanism is beyond the scope of this thesis, this term has been investigated only insofar as the best fit to the data is concerned. It has no significant effect on the fit and so its relevance to the FeTPPCl system awaits an adequate theoretical treatment of the exact superexchange mechanism. The antisymmetric exchange term $\vec{C} \cdot (\vec{S}_1 x \vec{S}_2)$ of Dzialoshinsky[36] and Moriya[37] is a result of a higher order spin-orbit-exchange contribution. This contribution requires a lack of inversion symmetry about the midway point between the chloride ions of the pair. The effect of this term on the best fit parameters is negligible. Since some of the ESR pair results relate to this term, it will be discussed again in Chapter V.

The total Hamiltonian for the system (neglecting the classical dipolar coupling) may be written as:

$$H = \sum_{i=1}^{N-2\alpha} H_i^{(\text{Singles})} + \sum_{j=1}^{\alpha} H_j^{(\text{Pairs})} \qquad (36)$$

$$H^{(\text{Singles})} = D_c[S_z^2 - \tfrac{1}{3} S(S+1)] + g_{||} \mu_B H_o S_z \cos\theta$$

$$+ \tfrac{1}{2} g_{\perp} \mu_B H_o (S_1^+ + S_1^-) \sin\theta \qquad (37)$$

$$H^{(Pairs)} = D_c[S_{1z}^2+S_{2z}^2 - \frac{1}{3} S_1(S_1+1)-\frac{1}{3} S_2(S_2+1)]-J_{||} S_{1z}S_{2z}$$

$$- \frac{1}{2} J_{\perp}(S_1^+S_2^-+S_1^-S_2^+)+g_{||} \mu_B H_o \cos\theta(S_{1z}+S_{2z}) \qquad (38)$$

$$+ \frac{1}{2} g_{\perp} \mu_B H_o \sin\theta(S_1^++S_1^- + S_2^++S_2^-)$$

where $S^+ = S_x + i S_y$ (39)

$S^- = S_x - i S_y$ (40)

are the spin raising and lowering operators for a spin-5/2 system. The crystal field effect term has been included, as well as the Zeeman term for a magnetic field, $H_o$, applied in the a-c plane at an angle $\theta$ with respect to the c-axis. The number of pairs is given by $\alpha$, and the total number of paired molecules is $2\alpha$. The solution to the singles problem yields an effective spin-1/2 system with an anisotropic g factor ranging from $g_{||} = 2$ to $g_{eff\perp} = 6$, as described in Chapter II. The susceptibility of the singles follows a Curie law with only $(N-2\alpha)$ effective-spin-1/2 ions contributing rather than N spins.

The pair problem can be approached from two directions. The first deals with an exact solution of the problem involving the diagonalization of the full 36x36 Hamiltonian including all the crystal field states. The basis states to be used are combinations of the single ion states for a spin-5/2 system:

$$|+\tfrac{1}{2}\rangle,\ |-\tfrac{1}{2}\rangle,\ |+\tfrac{3}{2}\rangle,\ |-\tfrac{3}{2}\rangle,\ |+\tfrac{5}{2}\rangle,\ |-\tfrac{5}{2}\rangle \quad .$$

For a pair system in which there are two spin 5/2 ions interacting, there are 36 possible combination basis states based on the 6-fold spin multiplicity of each ion alone. These combination states are of the form:

$$|\tfrac{1}{2},\tfrac{1}{2}\rangle, |\tfrac{1}{2},-\tfrac{1}{2}\rangle, |-\tfrac{1}{2},\tfrac{1}{2}\rangle, |-\tfrac{1}{2},-\tfrac{1}{2}\rangle, |\tfrac{1}{2},\tfrac{3}{2}\rangle \quad , |\tfrac{1}{2},\tfrac{5}{2}\rangle \quad , \text{ etc.}$$

The exact solution involves calculating the matrix elements for the Hamiltonian in equation 38 using this basis set, and then diagonalizing this 36x36 matrix to obtain the energy eigenvalues. Then all the appropriate thermodynamic quantities of interest can be calculated by a direct application of equilibrium statistical mechanics. This is a straightforward problem, but it must be done on a computer in numerical form. Thus no analytic expressions result.

A second approach is a perturbation method. Since the temperature range investigated in our laboratory is below 4 K, it is obvious that a calculation on the $S_z = \pm 1/2$ crystal-field ground state should yield acceptable results. Thus the exchange and Zeeman terms were treated as perturbations on the $D_c(S_{1z}^2 + S_{2z}^2)$ crystal-field term. This calculation was carried out to third order for the 4 lowest exchange-split ground state energies. The next set of exchange-split energy levels are $2D_c$ higher in energy. From this calculation analytic expressions were obtained for

the energies, eigenvectors, partition function, and the resulting thermodynamic quantities for the parallel ($\theta=0°$) and perpendicular ($\theta=90°$) cases. For intermediate angles, the diagonalization of the 4x4 ground state subspace was not possible in a reasonable analytic form so the exact computer solution was used instead. The agreement between the exact computer calculation and the third order perturbation calculation for the $\theta=0°$ and $90°$ cases is excellent. (The difference between the computer and perturbation calculations for the $\theta=0°$ zero field energy levels is .005%.)

Theoretical Expressions for the Magnetic Susceptibility

From the energy levels, the susceptibility can be obtained by a straightforward application of statistical mechanics. The results for the combination pairs and singles system are:

$$\chi_{\parallel} = 4(\alpha/N)\left(\frac{Ng_{\parallel}^2\mu_B^2}{4k_BT}\right)\left[1 + q\, e^{-\beta J_{\parallel}/2}\cosh(9J_{\perp}\beta/2)\right]^{-1} + (1-2\alpha/N)\left(\frac{Ng_{\parallel}^2\mu_B^2}{4k_BT}\right) \tag{41}$$

$$\chi_{\perp} = 4(\alpha/N)\left(\frac{Ng_{eff\perp}^2\mu_B^2}{4k_BT}\right)\left[e^{\frac{\beta}{2}\left(\frac{J_{\parallel}-9J_{\perp}}{2}\right)} - q\, e^{-\frac{\beta}{2}\left(\frac{J_{\parallel}-9J_{\perp}}{2}\right)}\right] \times \left[\frac{1}{2}\beta\left(\frac{J_{\parallel}-9J_{\perp}}{2}\right)\right]^{-1}\left[p+e^{+\frac{\beta}{2}\left(\frac{J_{\parallel}-9J_{\perp}}{2}\right)} + q\, e^{-\frac{\beta}{2}\left(\frac{J_{\parallel}-9J_{\perp}}{2}\right)}\right]^{-1} + (1-2\alpha/N)\left(\frac{Ng_{eff\perp}^2\mu_B^2}{4k_BT}\right) \tag{42}$$

where $\alpha$ = number of pairs,

$$g_{||} = g_{\perp} = 2$$

$$g_{eff\perp} = 3g_{\perp} = 6$$

$$\beta = (k_B T)^{-1}$$

$$q = e^{-\beta\left(14J_{\perp}^2/D_c - 9J_{||}J_{\perp}^2/(2D_c^2)\right)} \tag{43}$$

$$p = e^{\beta\left(\frac{J_{||}-9J_{\perp}}{4}\right)}\left[1 + q\, e^{-\beta\left(\frac{J_{||}+9J_{\perp}}{2}\right)}\right] \tag{44}$$

N = Avogadro's number, $k_B$ = Boltzmann constant, $\mu_B$ = Bohr magneton.

The details of the perturbation calculation are given in Appendix B. The theoretical curves for $\chi_{||}$ and $\chi_{\perp}$ are superimposed on the experimental data for the single crystal in Figure 13. The $\chi_{||}$ data were obtained from the SQUID magnetometer in an applied field of 25 gauss, while the $\chi_{\perp}$ data were measured in the SQUID using a field of 2.5 gauss. The $\chi_{||}$ curve has been obtained from the computer calculation to include the 10° misalignment. The parameters used to obtain this fit are:

$$J_{||}/k_B = (+.40 \pm .03)\ \text{K}\ ;\ J_{\perp}/k_B = (-.1525 \pm .003)\ \text{K} \tag{45}$$

$$\alpha/N = .255 \pm .004 \tag{46}$$

$$D_c/k_B = 13\ \text{K}\ ,\ g_{||} = g_{\perp} = 2\ ;\ g_{eff\perp} = 3g_{\perp} = 6\ .$$

The values for $J_{||}$, $J_{\perp}$, and $\alpha/N$ result from the best fit of the theory to three different pieces of experimental data:

single crystal magnetic susceptibility, powder heat capacity, and electron spin resonance on both powder samples and a single crystal. It should be stressed that slightly different values for $J_{||}$, $J_{\perp}$, and $\alpha/N$ may give a better fit for one particular set of experimental data. However, the theoretical result for the other sets then gives bad agreement. The errors given on the values of $J_{||}$, $J_{\perp}$, and $\alpha/N$ reflect the range within which these parameters may be varied without a serious change in the fit to all of the experimental data. Figure 14 shows the effect of changing $J_{||}$, $J_{\perp}$, and $\alpha/N$ on the fit to the single crystal susceptibility data.

To ensure that there was no gross difference in purity between the FeTPPCl powder and the FeTPPCl single crystal, the "effective" powder susceptibility obtained from the single crystal runs was compared to the actual powder data. The effective powder susceptibility is given as:

$$\chi_{eff} = \frac{1}{3}\chi_{||} + \frac{2}{3}\chi_{\perp} \qquad (47)$$

which is a result of averaging over all the crystallite orientations in the powder. The 1/3 and 2/3 are a result of the cylindrical symmetry of the FeTPPCl molecule. The comparison to the actual powder data is shown in Figure 15. The agreement is quite good, thus confirming that the crystallization process did not affect the purity of the FeTPPCl. It also confirms the stability of the FeTPPCl over long periods of storage, since the powder data shown here was taken about 4 months after the first single crystal run.

Figure 14. The effect on the susceptibilities, $\chi_{||}$ and $\chi_{\perp}$, of changing the fit parameters $J_{||}$, $J_{\perp}$, and $\alpha/N$.

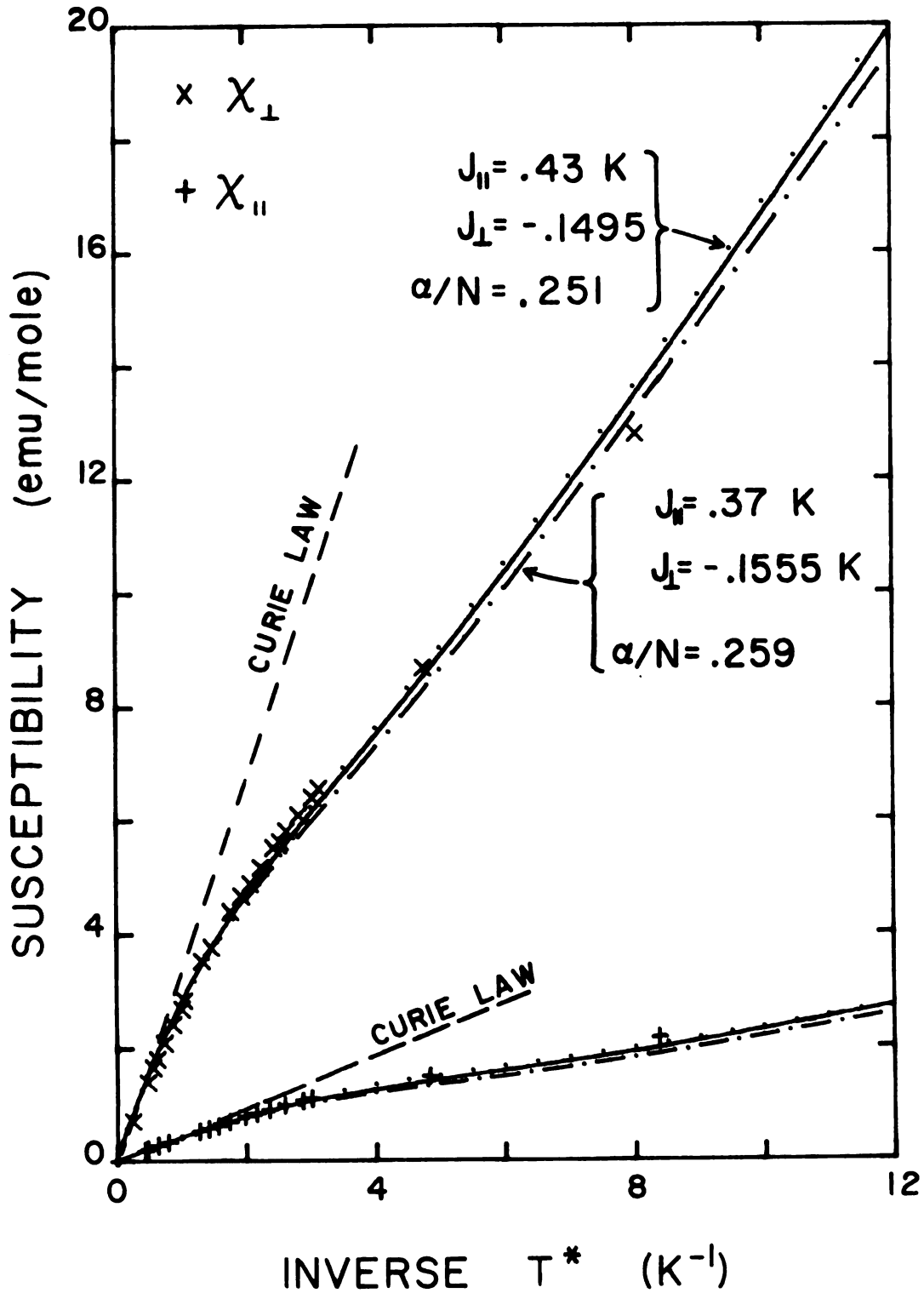
20
16
12
8
4
0
0
4
8
12
× $\chi_\perp$
+ $\chi_{11}$
$J_{11}$= .43 K
$J_\perp$= -.1495
α/N = .251
$J_{11}$= .37 K
$J_\perp$= -.1555 K
α/N= .259
CURIE LAW
CURIE LAW
SUSCEPTIBILITY (emu/mole)
INVERSE T* ($K^{-1}$)

Figure 15. Comparison of single crystal susceptibility data with the powder susceptibility data in the high temperature (.2 K - 4 K) range. The solid curves represent the theory using the best fit values of $J_{||}$, $J_{\perp}$, and $\alpha/N$ mentioned in the text.

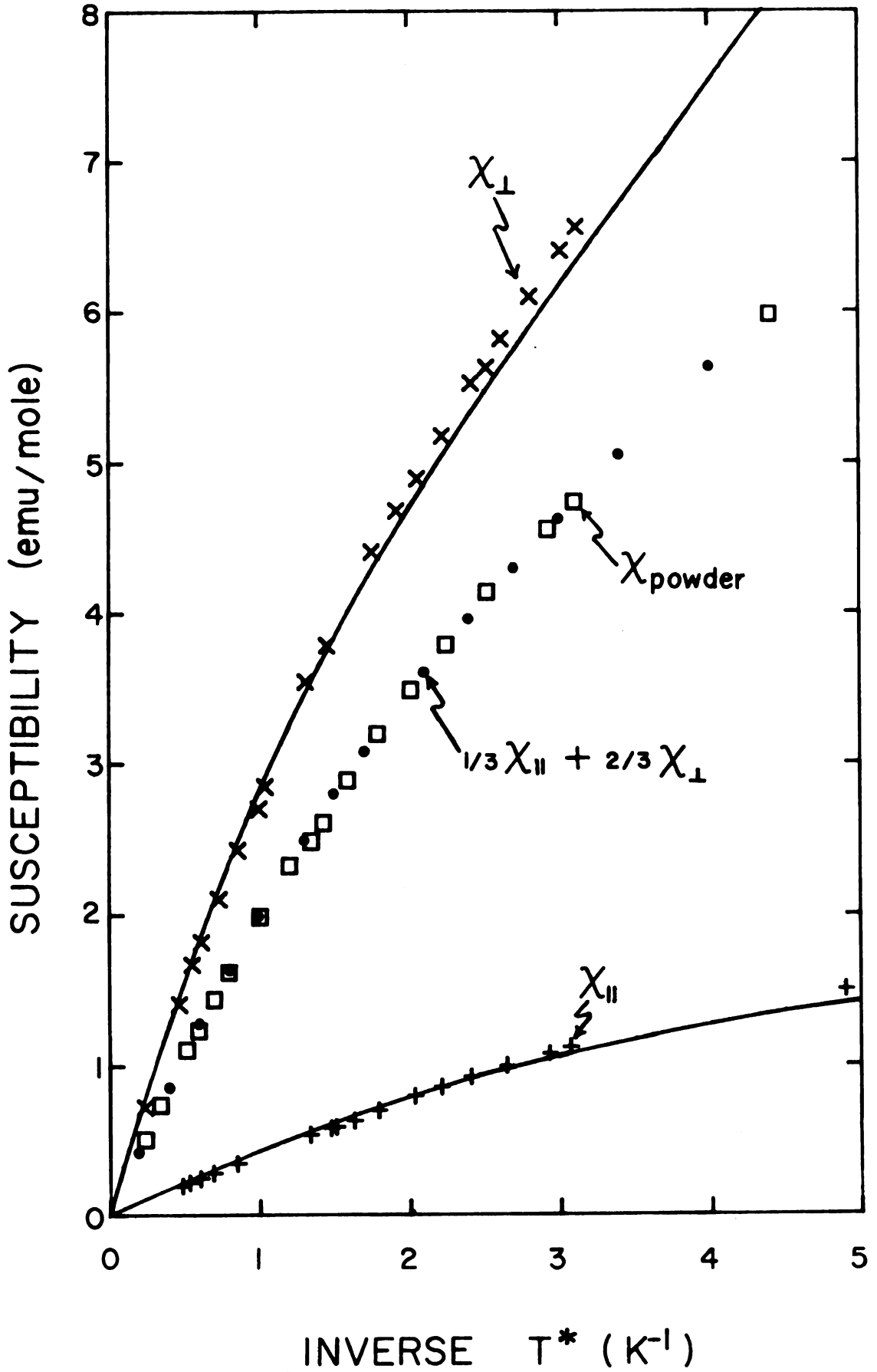
SUSCEPTIBILITY (emu/mole)
INVERSE T* (K⁻¹)
χ⊥
χpowder
1/3 χ|| + 2/3 χ⊥
χ||
0
1
2
3
4
5
6
7
8

Classical Dipolar Corrections

It should be pointed out that the effect of the classical dipole-dipole interaction within the pair is, in effect, included in the values of $J_{||}$ and $J_{\perp}$. For two ions which have parallel principal axes and which have the line joining them along the common z-axis, the dipole-dipole interaction can be written as[38]:

$$H_d = \mu_B^2 r_{ij}^{-3} [g_{\perp}^2 (S_{1x}S_{2x} + S_{1y}S_{2y}) - 2g_{||}^2 S_{1z}S_{2z}] \quad (48)$$

where $r_{ij}$ is the distance between the two interacting dipoles; $\mu_B$ is the Bohr magneton; $g_{||} = g_{\perp} = 2$; $S_{1z}$ and $S_{2z}$ are z-component spin operators which take on the values $\pm 1/2$ in the ground state configurations; and $S_{1x}$, $S_{2x}$, $S_{1y}$, $S_{2y}$ are the x and y component spin-5/2 operators for the members of the pair. Because of this simple form, the original pair Hamiltonian contains the effect of the pair dipole-dipole interaction if one merely re-defines $J_{||}$ and $J_{\perp}$ as:

$$J_{||} = J_{||}^{exch} + \frac{2g_{||}^2 \mu_B^2}{r_{12}^3} = J_{||}^{exch} + .0068 \text{ K} \quad (49)$$

$$J_{\perp} = J_{\perp}^{exch} - \frac{g_{\perp}^2 \mu_B^2}{r_{12}^3} = J_{\perp}^{exch} - .0034 \text{ K} \quad (50)$$

where $r_{12} = 9.05$ Å is the iron-iron distance between the members of the FeTPPCl pair. Thus the effect of the classical dipolar coupling within the pair is quite small compared to

the superexchange.

As indicated earlier, the lattice sums for the FeTPPCl system without the presence of pairing have been calculated so that a rough estimate of the lower temperature behavior is possible. If one were to treat the system as made up only of singles without superexchange pairing, then the Van Vleck[32] expansion given earlier would apply. Since the pair susceptibility goes to zero at the lower temperatures ($T<.1$ K), the exact method would randomly populate the $N$ lattice sites with $N-2\alpha$ magnetic dipoles (yet allowing for $2\alpha$ pair sites), and then carry out the dipole lattice sums. This exact treatment has not yet been undertaken. A rough calculation assumes that pairs do not form. Then one adds a term such as derived by Van Vleck so that the susceptibility becomes:

$$\chi_{||} \simeq \chi_{||}^{Pairs} + \chi_{||}^{Singles} + \left(\frac{C_{||}}{T}\right)^2 \left(-\frac{\Sigma_{||}}{N}\right) \tag{51}$$

$$\chi_{\perp} \simeq \chi_{\perp}^{Pairs} + \chi_{\perp}^{Singles} + \left(\frac{C_{\perp}}{T}\right)^2 \left(-\frac{\Sigma_{\perp}}{N}\right) \tag{52}$$

where $$C_{||} = \frac{Ng_{||}^2 \mu_B^2}{4k_B} \tag{53}$$

$$C_{\perp} = \frac{Ng_{eff\perp}^2 \mu_B^2}{4k_B} \tag{54}$$

and $\sum_{||} = -1.296\text{x}10^{21}$ cm$^{-3}$, $\sum_{\perp} = +6.45\text{x}10^{20}$ cm$^{-3}$ are the lattice sums for FeTPPCl.

If one uses these numbers to estimate a dipole correction to the susceptibility theory at $1/T = 10\ K^{-1}$, the result is to give almost perfect agreement to the $\chi_{\perp}$ data, and about 1/2 the difference needed for the $\chi_{||}$ data. It is important to note that the signs of the dipole sums are such that they pull the theory down in the perpendicular direction and enhance the theory in the parallel direction. This is exactly what is needed to give better agreement between the low temperature data and the theory.

## CHAPTER IV

## THE HEAT CAPACITY OF IRON TETRAPHENYLPORPHINE CHLORIDE

When the susceptibility measurements were completed, the pair formation was postulated, and the calculations were carried out as stated in Chapter III. However, it was felt that the existence of naturally occurring superexchange pairs was sufficiently unique that a measurement of another independent thermodynamic quantity would be useful. In addition, the susceptibility data pull-over is just not very striking. It was decided to attempt a measurement of the zero-field heat capacity. The heat capacity has a number of attractive features. First, if superexchange pairs were forming, there should be a peak in the heat capacity in a temperature range characteristic of the pairing energy. Second, the amplitude of such a heat capacity peak should give information concerning how many pairs were forming. Lastly, heat capacity measurements can be carried out on a powder sample, thereby by-passing the difficulties attendant to growing large single crystals. The difficulties involved were of an experimental nature. The temperature range of interest was from 0.1 K to 1 K, which is below that accessible to standard low temperature heat capacity systems. Thus, our dilution refrigerator was modified as described in Chapter I to make these measurements.

Over 120 heat capacity data points were taken in the temperature range from 1.5 K down to .052 K. There was quite a bit of scatter (approximately 5%) due to heat leaks, resulting in drifting in time of the temperature of the CR-50 thermometer. This was primarily due to the imperfection of the heat switch. Other metals have a much higher ratio of normal thermal conductivity to superconducting thermal conductivity. Unfortunately, other superconducting switches such as lead, indium, and tin also have higher critical fields. The solenoid wrapped on the coil #1 shield has only a 200 gauss capability, so that a major experimental modification would have been necessary to install a high field magnet. Consequently, the thermal isolation was not perfect. This was compensated for by running the refrigerator as close in temperature to the heat capacity sample unit as possible. This minimized the temperature gradient and any attendant heat flow to or from the sample. However, the output of the CR-50 resistor, which was monitored on a strip-chart recorder, quite often indicated a significant temperature drift in time. Enough time was allowed to elapse between data points so that the drift became a minimum. The refrigerator temperature was also adjusted to stop the temperature drift. As a result of these drifts, there is some scatter in the data. Of the original 127 data points, only 81 were judged to have a slow enough temperature drift in time to be accurate experimental points. In addition, because of the rather long thermal equilibration times at

the lower temperatures (several hours below 0.1 K), much fewer lower temperature points were taken.

Background Considerations

It should be mentioned that the heat capacity data has not been background corrected. The contributing factors to a background heat capacity are the copper resistor-mount and support foil, the zinc heat switch, platinum tabs, Evanohm heater and leads, and CR-50 resistor and leads. Excluding the CR-50 resistor, the total mass of all of these components is less than 1.2 gm with the copper contributing over 90% of this mass. Pure-copper heat capacity measurements of Franck, Manchester, and Martin[39] yield the expected linear relationship characteristic of the electronic contribution. Their values at 1 K indicate that the contribution due to the copper parts of the heat capacity tail is less than 1.5% of the measured FeTPPCℓ value at this temperature. The effect at lower temperatures becomes completely negligible due to the linear decrease with temperature of the copper heat capacity. The other sources of a background heat capacity are the Apiezon N grease and absorbed $^3$He. The heat capacity of N grease has been measured down to 0.4 K by Wun and Phillips[40]. Based on their measurements, a total mass of 0.1 gm of Apiezon N grease contributes only 0.25% of the FeTPPCℓ value at 1 K. Because of a $T^n$ dependence (n>1), its effect at lower temperatures is completely negligible. The $^3$He which might have absorbed to the graphite support tube

could have a significant effect, if some of the heat believed to be going to the sample was actually liberating some $^3$He from the graphite. The coating of the graphite with GE 7031 varnish should have minimized this problem.

## Theoretical Expression for the Heat Capacity

The heat capacity data is shown in Figure 16 along with the theoretical curve based on the pair model. The singles contribute nothing to the zero-field heat capacity since they are essentially non-interacting in the temperature range of interest. The expression for the heat capacity due to the pairs can be obtained from the zero-field energy eigenvalues and partition function:

$$C/R = (\alpha/N)(1/T)^2 e^{-\beta J'_{||}}[(J'_{||}/k_B)^2 \cosh J'_{\perp}\beta - 2(J'_{\perp}/k_B)(J'_{||}/k_B)x(\sinh J'_{\perp}\beta)+(J'_{\perp}/k_B)^2(\cosh J'_{\perp}\beta+e^{-\beta J'_{||}})] \times [1+e^{-\beta J'_{||}}\cosh J'_{\perp}\beta]^{-2} \quad (55)$$

$$\text{where } J'_{||} = J_{||}/2 + 14 J_{\perp}^2/D_C - 9J_{\perp}J_{||}/(2D_C^2) \quad (56)$$

$$J'_{\perp} = 9J_{\perp}/2 \quad (57)$$

$$\beta = (k_B T)^{-1} \quad (58)$$

$k_B$ = Boltzmann constant, R = gas constant, N = Avogadro's number.

The curve in Figure 16 is a best fit of this expression to the experimental data. It is based on the values

$$J_{||}/k_B = (+.40 \pm .03)\,K;\ J_{\perp}/k_B = (-.1525 \pm .003)\,K;\ \alpha/N = .255 \pm .004$$

Figure 16. Temperature dependence of the heat capacity from a 1.5 gm powdered sample of FeTPPCl. C is the heat capacity per mole of FeTPPCl, and R is the molar gas constant. The solid curve represents the theoretical calculation using the best-fit values of $J_{||}$, $J_{\perp}$, and $\alpha/N$ mentioned in the text.

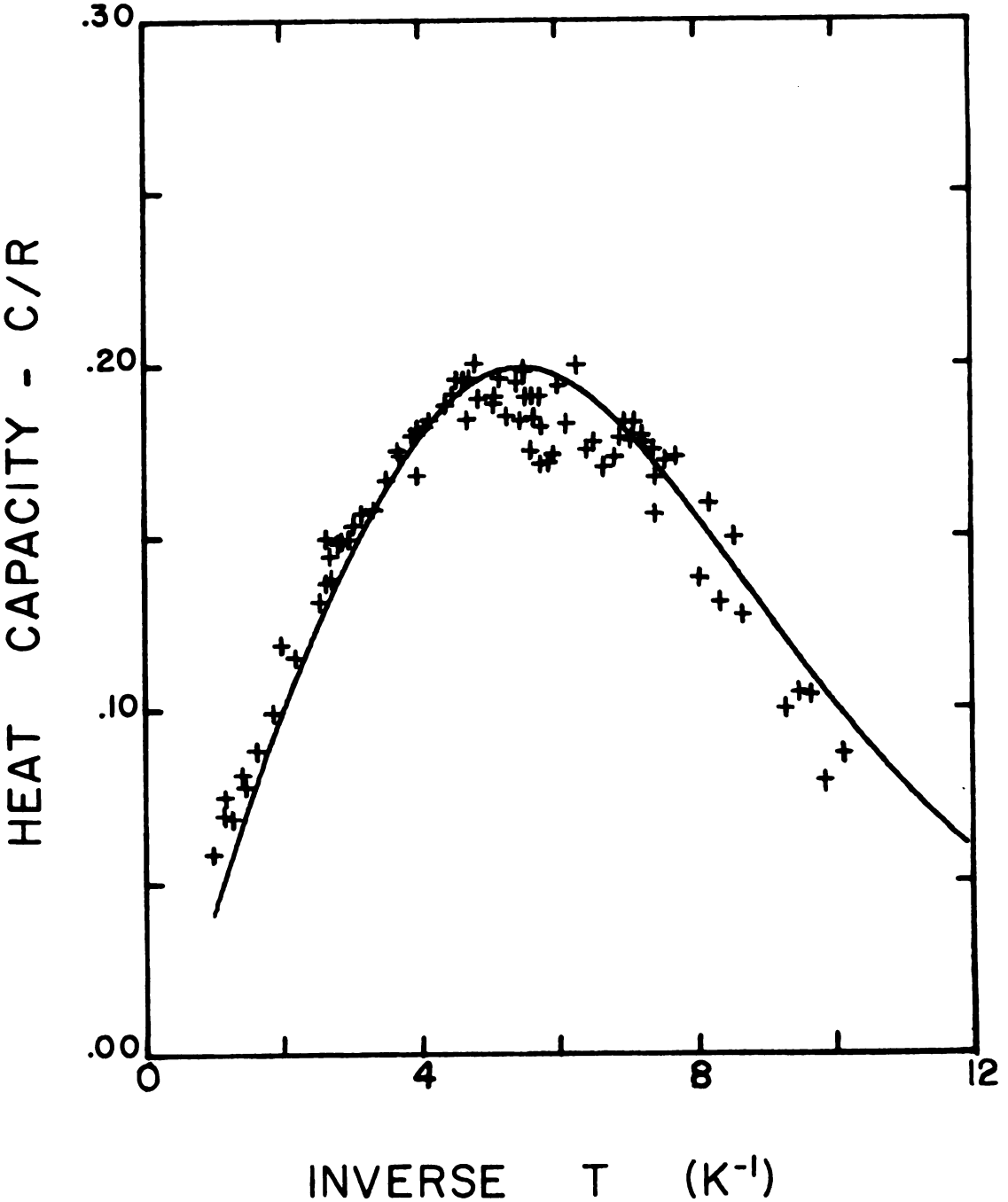
.30
.20
.10
.00
0
4
8
12
HEAT CAPACITY - C/R
INVERSE T (K⁻¹)

mentioned earlier as the susceptibility fit values. The amplitude of the heat capacity peak is a good measure of the number of pairs and is consistent with the value of $\alpha/N$ just quoted. Figure 17 gives some idea of how changing $J_{||}$, $J_{\perp}$, and $\alpha/N$ affects the heat capacity fit. The heat capacity expression is calculated for zero magnetic field.

Phonon Contribution

It should be noted that because of the $T^3$ tail of the phonon contribution to the heat capacity, the theoretical curve is not drawn for temperatures above 1 K. If one uses the Debye relation

$$C_p = \lambda T^3 \tag{59}$$

to estimate this contribution, the effect could be as large as 9% of the measured value at 1 K assuming an unrealistically large value for the constant $\lambda$. (E.g. use the largest value given in the CRC Handbook[41] for the organic material polystyrene.) However, as the temperature is lowered, even such a large value for $\lambda$ gives only a 1% contribution at 0.5 K. At temperatures lower than this, the phonon contribution is completely negligible. Thus, due to the existence of a $T^3$ phonon tail, it may not be too surprising that the high temperature data (i.e. $T>0.5$ K) fall a little above the theoretical curve.

Figure 17. The effect on the heat capacity of changing the fit parameters $J_{||}$, $J_{\perp}$, and $\alpha/N$.

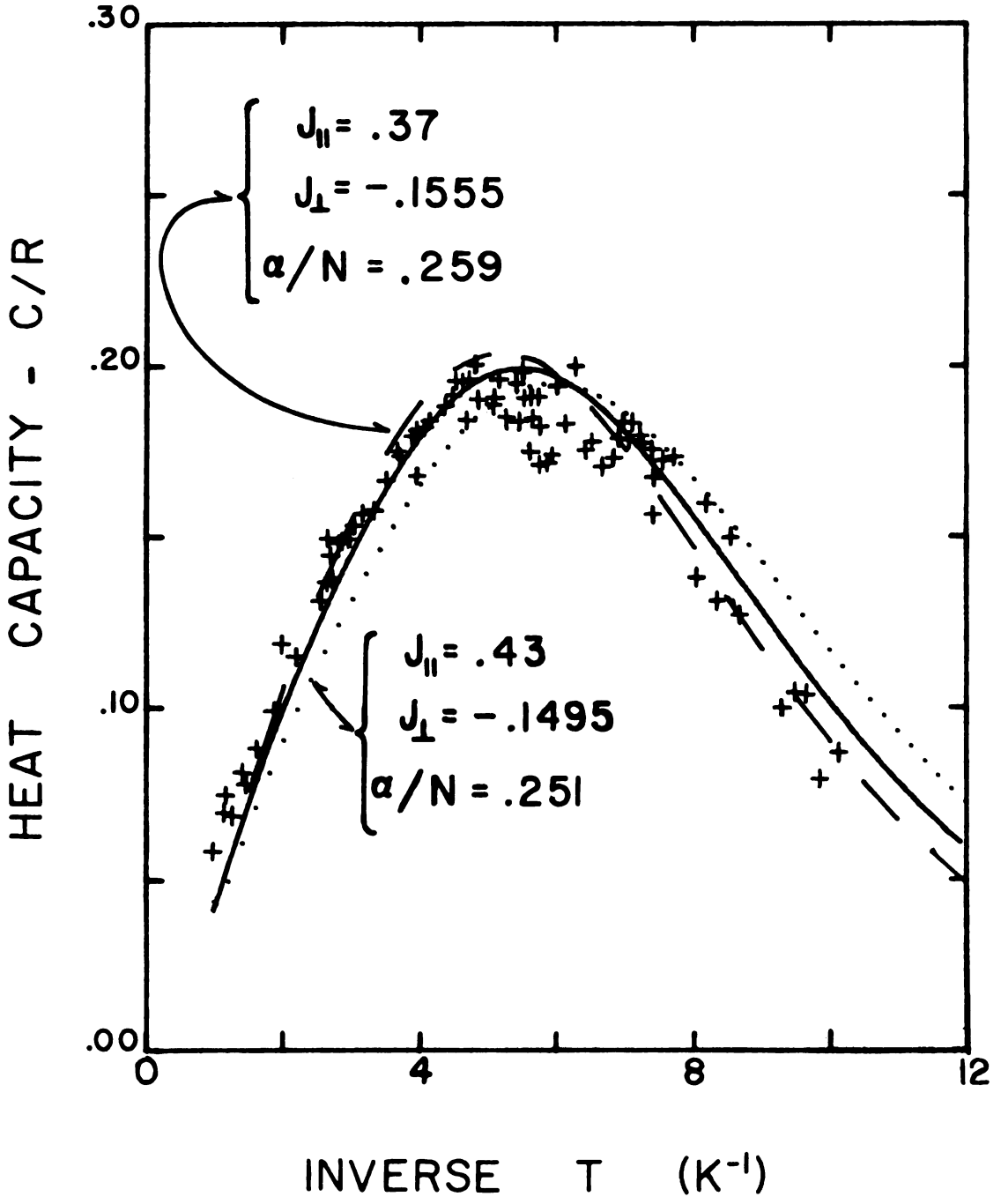
.30
.20
.10
.00
0
4
8
12
HEAT CAPACITY - C/R
INVERSE T (K⁻¹)
J∥ = .37
J⊥ = −.1555
α/N = .259
J∥ = .43
J⊥ = −.1495
α/N = .251

# CHAPTER V

## THE ELECTRON SPIN RESONANCE OF IRON TETRAPHENYLPORPHINE CHLORIDE

The heat capacity confirmation of the pairing model suggests a careful examination of the energy levels. The combination of the heat capacity and magnetic susceptibility data give stable best-fit values for $J_{||}$ and $J_{\perp}$, which, in turn, give well-defined values for the energy splittings. A check of these energy spacings reveal that they should be within the range of electron spin resonance (ESR) frequencies.

The first ESR measurements undertaken to specifically check on the pair spectra were taken on a single crystal. This single crystal was half of the 0.1 mgm single crystal from which the susceptibility data were obtained. The crystal had broken into two pieces when it was removed from the SQUID epoxy sample holder. Fortunately, the crystal broke into two well-defined halves so that the external morphology was still sufficiently recognizable. When placed under the 8X microscope, it was possible to align satisfactorily the crystal in the epoxy holder for the ESR experiment. The singles rotation diagram shown in Chapter II (figure 12) was obtained from this .05 mgm single crystal. As mentioned earlier, there was a 10° misorientation of the external field with respect to the c-axis, which is not

too surprising considering the small size of the crystal. During this single crystal run, the temperature was lowered to 1.2 K. This lower temperature gave a sufficient over-population of the pair ground state levels that a pair resonance line was observed in addition to the more intense line due to the single FeTPPCℓ molecules. The position of the center of an ESR line indicates the magnetic field at which the energy level separation is exactly equal to the energy quantum supplied by the oscillating microwave field. An actual experimental ESR trace for the single crystal run is shown in Figure 18. This derivative detection trace was taken with the DC external field, Ho, oriented at approximately 3° from the assumed position of the crystalline c-axis. The singles line, the pair line, and the DPPH marker are all clearly visible above the noise. The magnetic field scale gives the position of the lines as well as some idea of the line widths. The 10° misorientation is demonstrated by the fact that the singles line is shifted from the g = 2.004 DPPH line. Fifteen other field orientations in the assumed a-c plane were measured. The position of the center of both the pair line and the singles line could be observed to move as the field was rotated. At an angle of 30° the pair line was hidden by the singles line. At all other angles at least part of the pair line was visible so that a pair rotation diagram could be made. This diagram consists of the magnetic field at which the center of the pair resonance line was measured as a function of the angle

Figure 18. Electron spin resonance trace obtained using derivative detection at 1.2 K on a .05 mgm aligned single crystal of FeTPPCl.

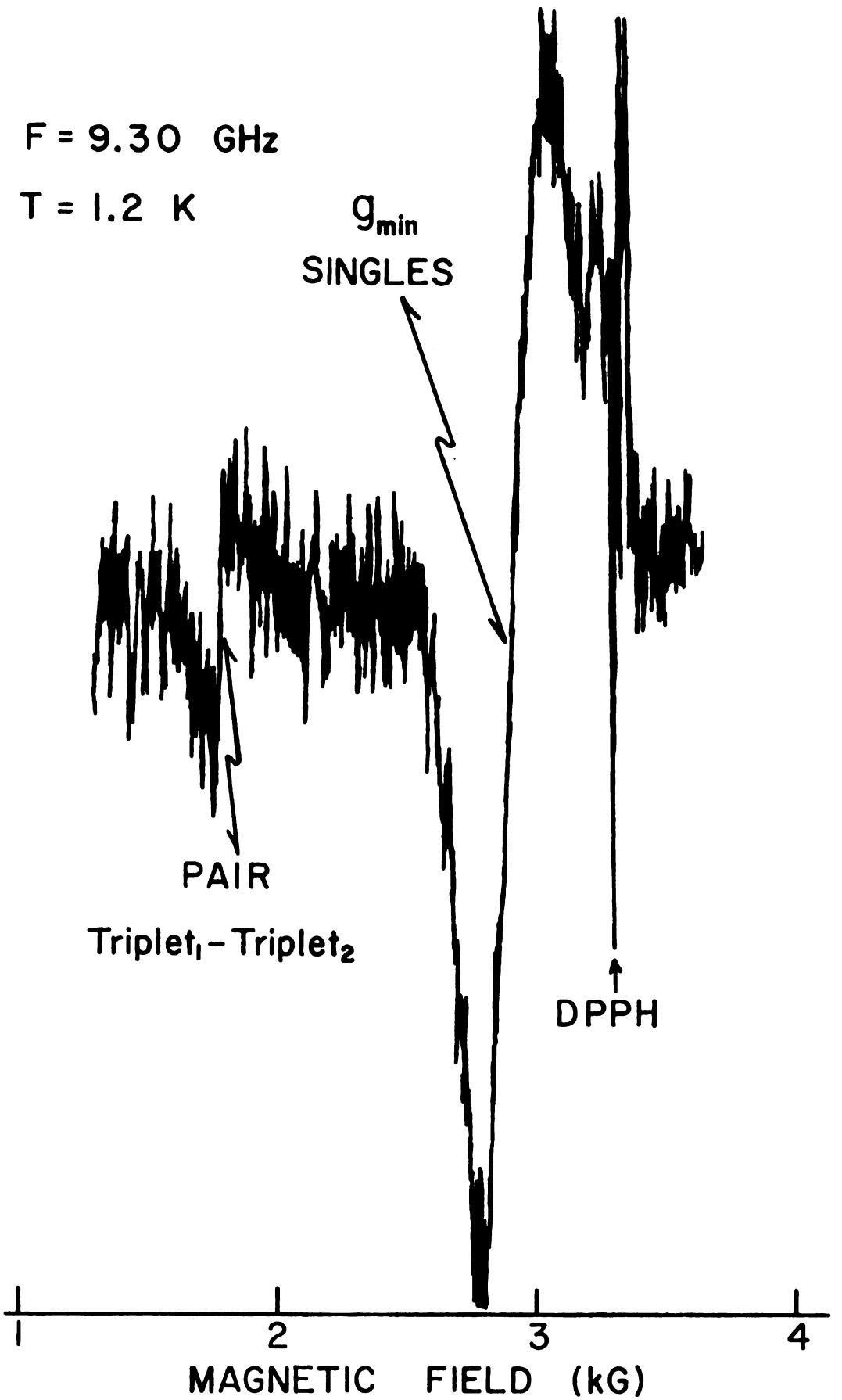
F = 9.30 GHz
T = 1.2 K
$g_{min}$
SINGLES
PAIR
$Triplet_1 - Triplet_2$
DPPH
1
2
3
4
MAGNETIC FIELD (kG)

that the field made with respect to the c-axis. This gives direct information concerning how the energy difference between the levels for this particular pair transition changes as a function of field, $H_o$, and angle, $\theta$. This pair rotation diagram is shown in Figure 19. The magnetic field values were carefully obtained by setting the magnetic field right on the center of the resonance line and then measuring the field with a rotating coil gaussmeter.

Analytic Expressions for the Pair Ground-State Energy Levels and Spin Eigenstates

To compare the ESR rotation data to the predictions of the pair model, the energy levels for all angles, including the effect of misalignment, were required. The third-order perturbation calculation for the pair ground-state energies can be solved analytically only in the $\theta=0°$, 90° cases. The analytic expressions for the pair ground-state energy levels and spin eigenstates in these limiting cases are given by:

$\vec{H}_o$ parallel to c-axis ($\theta=0°$):

$$E_o = -\frac{36}{6} D_c + J_{||}/4 + 9J_{\perp}/2 - 4J_{\perp}^2/D_c + 9J_{||}J_{\perp}^2/(4D_c^2) \quad (60)$$

$$|\phi_o\rangle = \frac{1}{\sqrt{2}} \{|-\tfrac{1}{2},\tfrac{1}{2}\rangle - |\tfrac{1}{2},-\tfrac{1}{2}\rangle\} \quad (61)$$

$$E_1 = -\frac{32}{6} D_c - J_{||}/4 - 18\, J_{\perp}^2/D_c + 27\, J_{\perp}^2 J_{||}/(4D_c^2) - (1+9J_{\perp}^2/D_c^2)h_{||} \quad (62)$$

$$|\phi_1\rangle = |-\tfrac{1}{2},-\tfrac{1}{2}\rangle \quad (63)$$

Figure 19. Angular dependence of the pair $triplet_1$-$triplet_2$ transition in a magnetic field. The abscissa represents the angle at which the magnetic field was oriented from the lab z-axis. The ordinate gives the magnetic field at which the single crystal ESR pair resonance was observed for the corresponding angular orientation. The crosses, + , represent the experimental data, and the solid curve is a result of a theoretical calculation including the effect of a 10° misalignment of the crystalline c-axis from the lab z-axis.

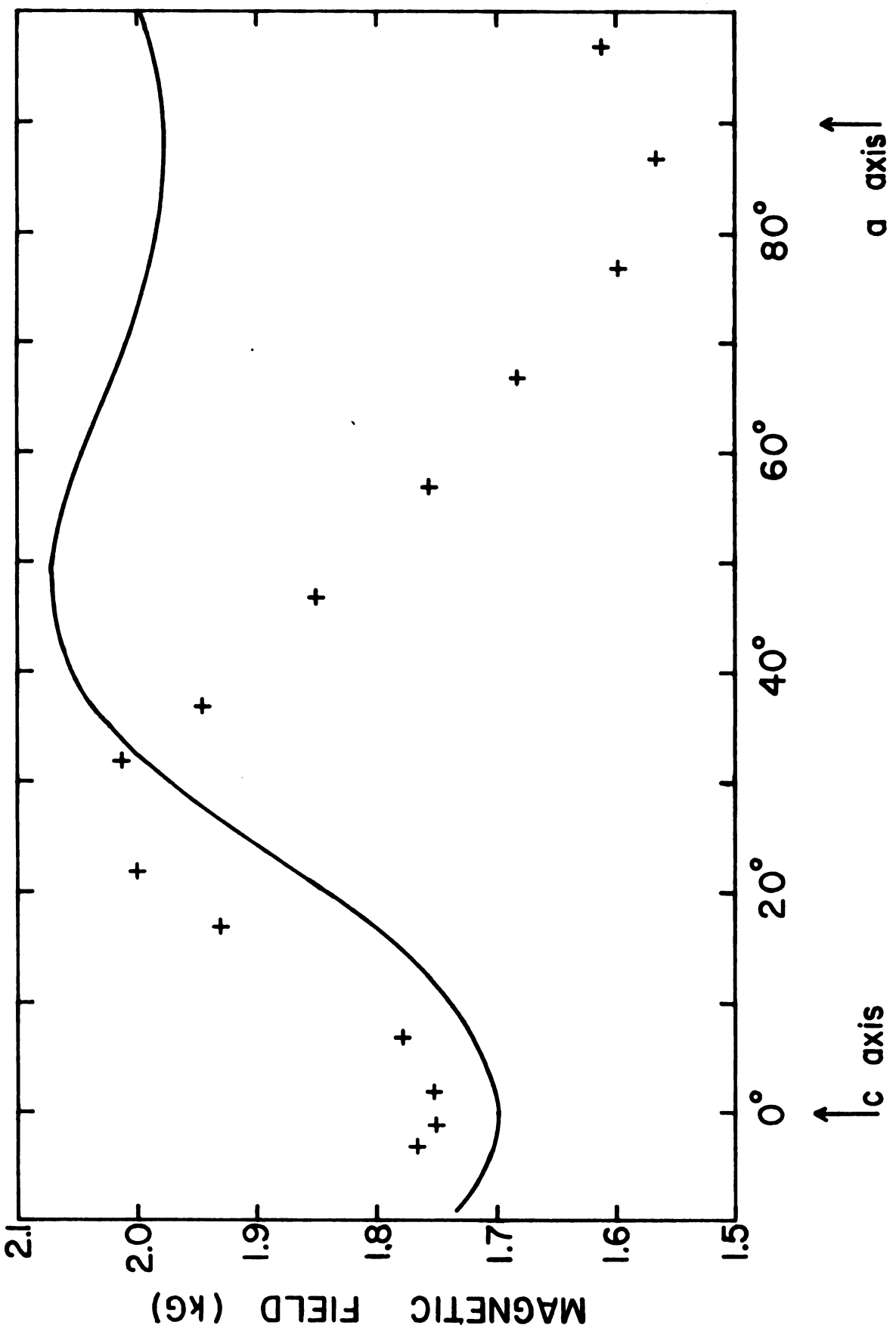
MAGNETIC FIELD (kG)
2.1
2.0
1.9
1.8
1.7
1.6
1.5
0°
20°
40°
60°
80°
c axis
a axis

$$E_2 = -\frac{32}{6} D_c - J_{||}/4 - 18 J_\perp^2/D_c + 27 J_\perp^2 J_{||}/(4D_c^2) \quad (64)$$
$$+ (1+9J_\perp^2/D_c^2)h_{||}$$

$$|\phi_2\rangle = |\tfrac{1}{2},\tfrac{1}{2}\rangle \quad (65)$$

$$E_3 = -\frac{32}{6} D_c + J_{||}/4 - 9J_\perp/2 - 4J_\perp^2/D_c + 9J_{||}J_\perp^2/(4D_c^2) \quad (66)$$

$$|\phi_3\rangle = \frac{1}{\sqrt{2}} \{|-\tfrac{1}{2},\tfrac{1}{2}\rangle + |\tfrac{1}{2},-\tfrac{1}{2}\rangle\} \quad (67)$$

where $D_c$ is the crystal field parameter; $J_{||}$ is the superexchange coupling parameter for the z-components of the spins; $J_\perp$ is the superexchange coupling parameter for the x and y components of the spins; $h_{||} = g_{||} \mu_\beta H_o$, where $g_{||} = 2$, $\mu_\beta$ is the Bohr magneton, and $H_o$ is the magnitude of the applied magnetic field.

$\vec{H}_o$ perpendicular to c-axis ($\theta$=90°):

$$E_o = -\frac{32}{6} D_c + J_{||}/4 + 9J_\perp/2 - 4J_\perp^2/D_c$$
$$+ 9J_{||}J_\perp^2/(4D_c^2) - 8h_\perp^2/D_c \quad (68)$$

$$|\phi_o\rangle = \frac{1}{\sqrt{2}} \{|-\tfrac{1}{2},\tfrac{1}{2}\rangle - |\tfrac{1}{2},-\tfrac{1}{2}\rangle\} \quad (69)$$

$$E_1 = -\frac{32}{6} D_c - 9J_\perp/4 - A/2 - (2/D_c)(h_\perp/N_3)^2(18J_\perp-2K)^2$$
$$- (4J_\perp^2/D_c)(K/N_3)^2 + (3/4)J_{||}[(18J_\perp-K)/D_c]^2(h_\perp/N_3)^2 \quad (70)$$

$$|\phi_1\rangle = \frac{1}{N_3} \{h_\perp'|\tfrac{1}{2},\tfrac{1}{2}\rangle + (K/\sqrt{2})|-\tfrac{1}{2},\tfrac{1}{2}\rangle$$
$$+ (K/\sqrt{2})|\tfrac{1}{2},-\tfrac{1}{2}\rangle + h_\perp'|-\tfrac{1}{2},-\tfrac{1}{2}\rangle\} \quad (71)$$

$$E_2 = -\frac{32}{6} D_c - J_{||}/4 - 18J_\perp^2/D_c + 27J_{||}J_\perp^2/(4D_c^2) - 8h_\perp^2/D_c \quad (72)$$

$$|\phi_2\rangle = \frac{1}{\sqrt{2}} \{|\tfrac{1}{2},\tfrac{1}{2}\rangle - |-\tfrac{1}{2},-\tfrac{1}{2}\rangle\} \quad (73)$$

$$E_3 = -\frac{32}{6} D_c - 9J_\perp/4 + A/2 - (4J_\perp^2/D_c)(B/N_2)^2$$
$$+ [9J_{||}J_\perp^2/(4D_c^2)](B/N_2)^2 - (2/D_c)(h_\perp/N_2)^2(18J_\perp - 2B)^2 \quad (74)$$

$$|\phi_3\rangle = \frac{1}{N_2}\{h'_\perp|\tfrac{1}{2},\tfrac{1}{2}\rangle + (B/\sqrt{2})|-\tfrac{1}{2},\tfrac{1}{2}\rangle + (B/\sqrt{2})|\tfrac{1}{2},-\tfrac{1}{2}\rangle$$
$$+ h'_\perp|-\tfrac{1}{2},-\tfrac{1}{2}\rangle\} \quad (75)$$

where $h'_\perp = 3\sqrt{2}h_\perp$; $h_\perp = \frac{1}{2}g_\perp\mu_\beta H_o$, $g_\perp = 2.0$; (76)

$$A = [(J_{||} - 9J_\perp)^2/4 + (6\,\mu_\beta\, g_\perp H_o)^2]^{1/2} \quad (77)$$

$$B = (J_{||} - 9J_\perp)/4 + A/2 \quad (78)$$

$$K = (J_{||} - 9J_\perp)/4 - A/2 \quad (79)$$

$$N_2 = [72h_\perp^2 + (J_{||} - 9J_\perp)^2/8 + (A/4)(J_{||} - 9J_\perp)]^{1/2} \quad (80)$$

$$N_3 = [72h_\perp^2 + (J_{||} - 9J_\perp)^2/8 - (A/4)(J_{||} - 9J_\perp)]^{1/2} \quad (81)$$

It should be noted that a state such as $|+\frac{1}{2},-\frac{1}{2}\rangle$ is a combination state specifying that iron ion #1 of the pair is in the $S_{1z} = +1/2$ state and iron ion #2 of the pair is in the $S_{2z} = -1/2$ state. In addition, the spin eigenstates listed above are only the adapted eigenstates which diagonalize the 4x4 subspace of the perturbed Hamiltonian for $S_{1z} = \pm 1/2$, $S_{2z} = \pm 1/2$ as shown in Appendix B. They are not the third-order perturbed eigenstates.

These basis states have been written in such a way to emphasize their singlet-triplet nature under interchange of the spins. That is, the ground state of the exchange split quartet is a spin singlet (i.e., it is an odd function under interchange of the spins). The three higher states form a zero-field-split triplet as indicated

in Figure 20. The subscript notation 0, 1, 2, 3 used in equations 60-75 classifies the singlet as 0 state, and the triplet into a 1, 2, and 3 state in order of increasing energy when the best-fit values of $J_{||}$, $J_{\perp}$, and $D_c$ are used. The energy level diagram in Figure 20 has the singlet level defined as the arbitrary zero of energy with the triplet levels lying above it. The vertical scale is labelled in degrees Kelvin so that the energies are actually $E_i/k_\beta$. Since the pair rotation diagram requires a more general treatment, the computer program was used to diagonalize the 36x36 matrix to obtain the 4 ground state pair energies for any arbitrary field, angle, and misalignment. Using the values $D_c/k_\beta$ = 13 K, $J_{\perp}/k_\beta$ = -.1525 K, $J_{||}/k_\beta$ = +.40 K, the energy levels for the $\theta$=0°, 90° limiting cases, as shown in Figure 20, result. The small curved arrows indicate how the levels change as the field is rotated. The single-line vertical arrow indicates the position of the pair resonance line shown in the trace of Figure 18. This line also points up the fact that the observed single-crystal pair resonance is due to the $\text{triplet}_1$ - $\text{triplet}_2$ transition shown. Thus the rotation diagram gives only the relative changes of these two pair levels as a function of field and angle. The double-line vertical arrows indicate the positions of observed transitions from powdered samples in other ESR runs. These powder transitions are obtained from direct absorption ESR signals as shown in Figures 21, 22, and 23.

Figure 20. Energy-level diagram for the superexchange-coupled pairs at 0° and 90° orientations of the c-axis with respect to an external magnetic field. The lowest lying state (singlet) in zero magnetic field is arbitrarily defined as the zero of energy. The short curved arrows indicate the direction that these energy levels shift as the field is rotated from 0° to 90°. The double-line vertical arrows indicate the positions of observed powder transitions. The single-line vertical arrow indicates the position of one of the observed single crystal transitions.

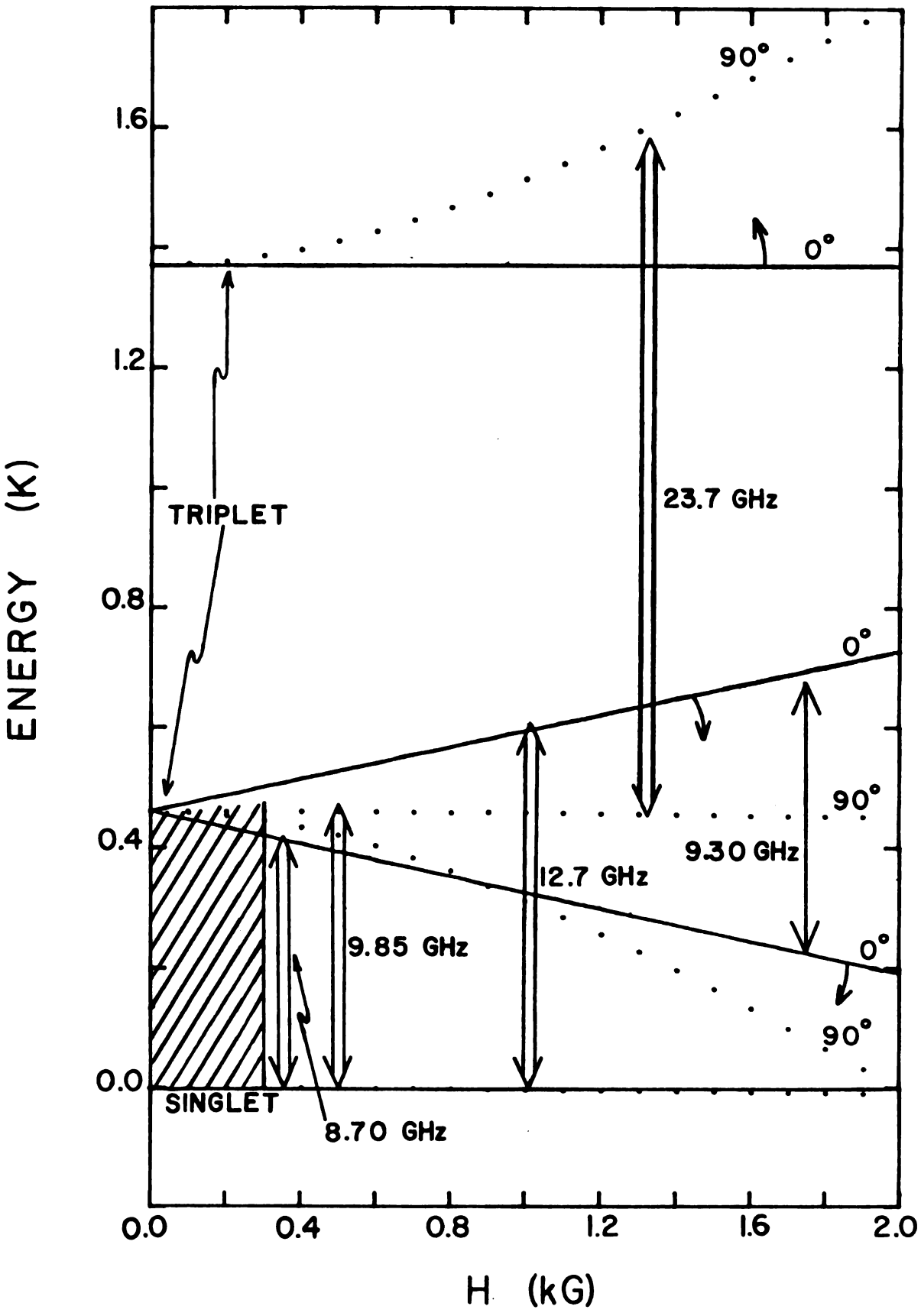
90°
0°
1.6
1.2
0.8
0.4
0.0
TRIPLET
23.7 GHz
0°
90°
9.30 GHz
12.7 GHz
9.85 GHz
0°
90°
SINGLET
8.70 GHz
ENERGY (K)
0.0
0.4
0.8
1.2
1.6
2.0
H (kG)

Figure 21. Electron spin resonance trace using direct detection from an 8.8 mgm powder sample of FeTPPCl. The upper trace was obtained with the external DC field oriented perpendicular to the oscillating microwave field. The lower trace was obtained with the DC magnetic field parallel to the oscillating microwave field, showing only the low-field forbidden singlet-triplet transition.

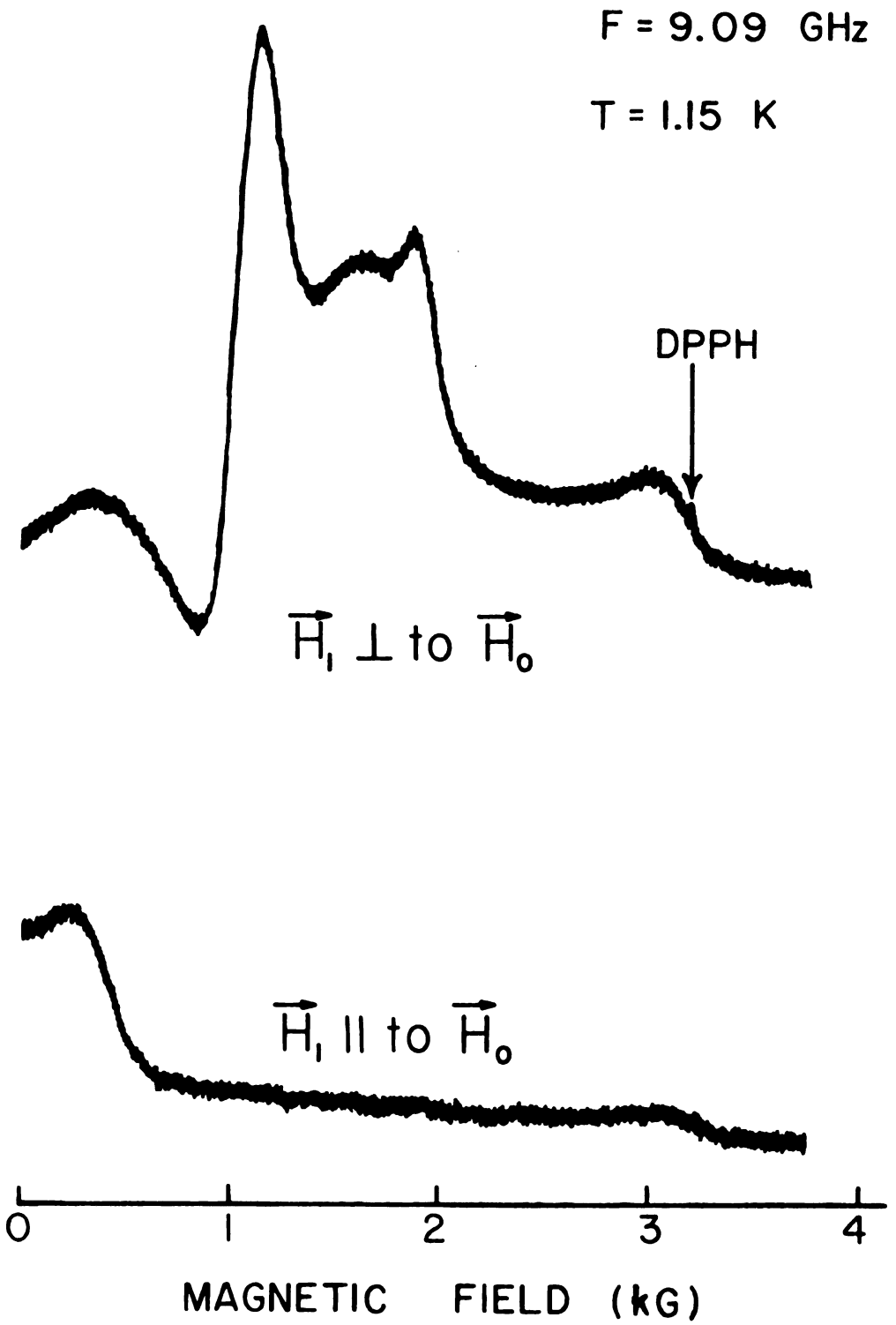
F = 9.09 GHz
T = 1.15 K
DPPH
$\vec{H}_1 \perp$ to $\vec{H}_0$
$\vec{H}_1$ II to $\vec{H}_0$
0
1
2
3
4
MAGNETIC FIELD (kG)

Figure 22. Electron spin resonance trace using direct detection from an 8.8 mgm powder sample of FeTPPCl. The singlet-triplet$_2$ transition at approximately 1000 gauss confirms how the separation between these levels increases as the magnetic field is increased. This is evident since now the microwave quantum of energy is larger (12.7 GHz), and hence the low-field transition shown in Figure 21 has moved out to higher magnetic field values.

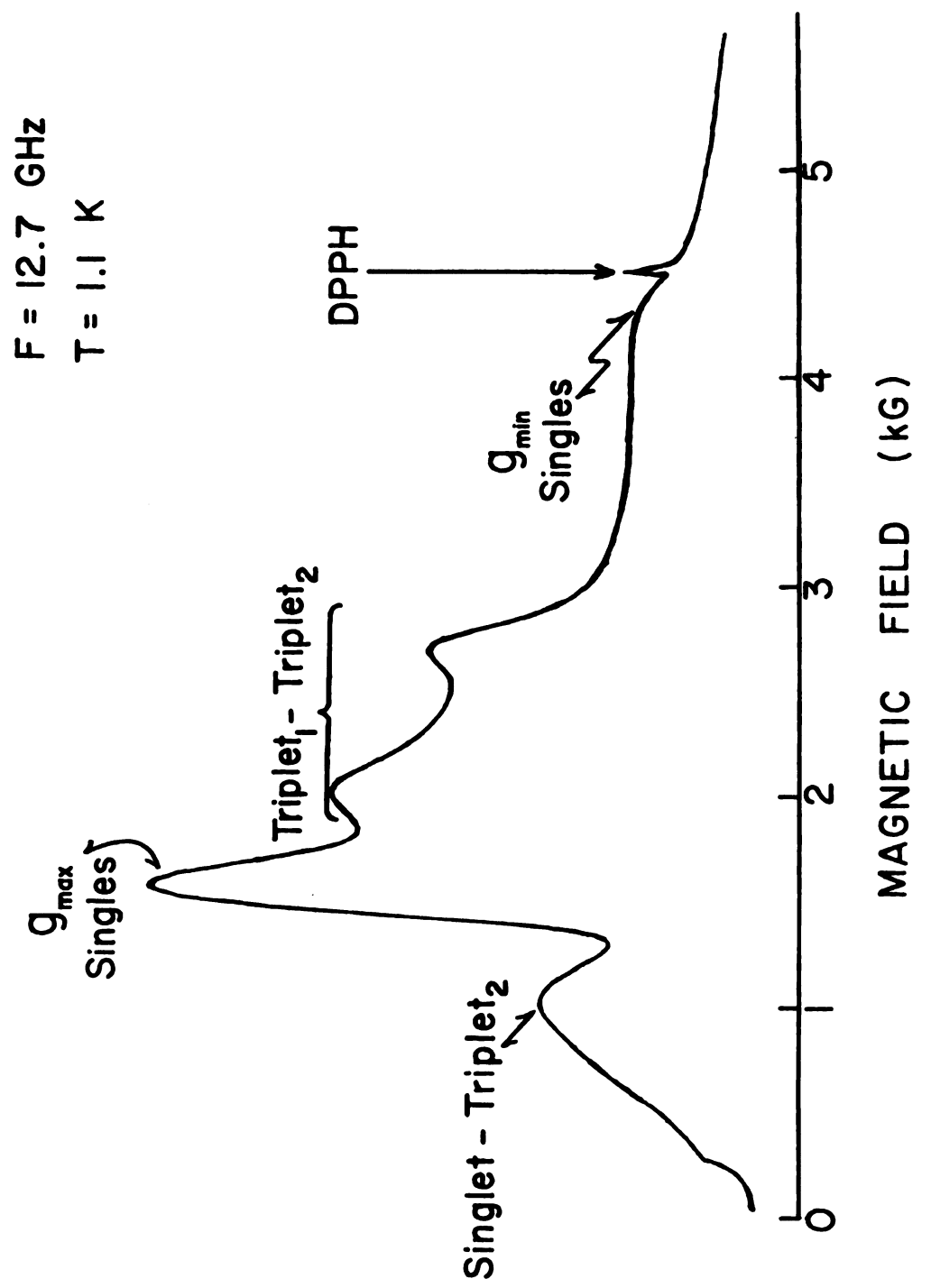
F = 12.7 GHz
T = 1.1 K
DPPH
$g_{min}$ Singles
Triplet$_1$ - Triplet$_2$
$g_{max}$ Singles
Singlet - Triplet$_2$
0
1
2
3
4
5
MAGNETIC FIELD (kG)

Figure 23. Electron spin resonance trace using direct detection from a 20 mgm powder sample of FeTPPCl. The upper trace was obtained with the external DC magnetic field oriented perpendicular to the oscillating microwave field. The lower trace was obtained with the DC magnetic field oriented almost parallel to the microwave field. The electronic gains in the detection system for the lower trace were greater by at least a factor of 2 than in the upper trace. The presence of the $triplet_2$-$triplet_3$ transition at approximately 1300 gauss is quite evident from this technique.

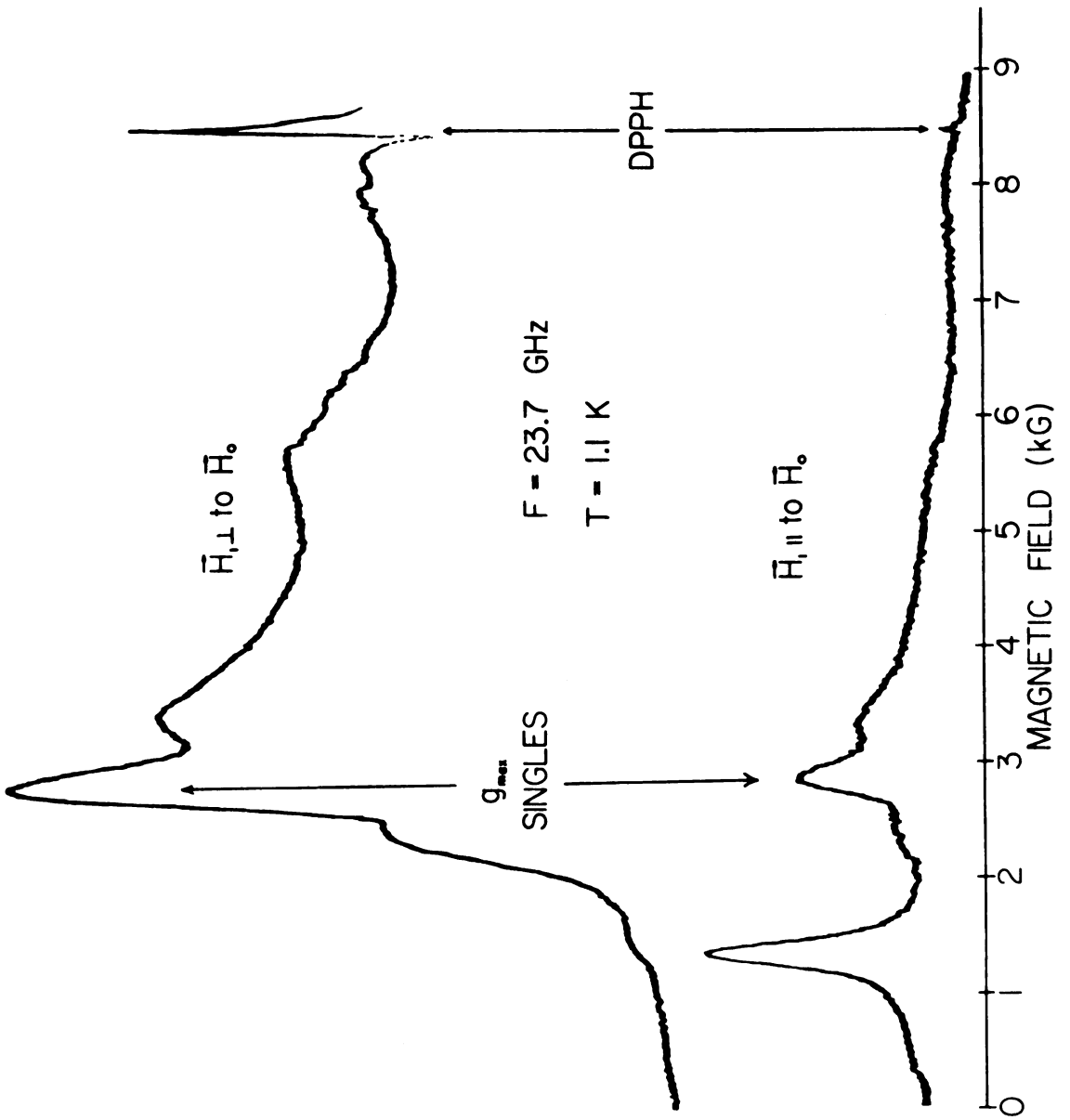
$\vec{H}, \perp$ to $\vec{H}_o$
$g_{max}$
SINGLES
F = 23.7 GHz
T = 1.1 K
DPPH
$\vec{H}, \parallel$ to $\vec{H}_o$
0
1
2
3
4
5
6
7
8
9
MAGNETIC FIELD (kG)

Note that the signal maxima are used to define the fields at which the double arrows in Figure 20 are plotted. From the complete set of energy levels obtained from the computer print-out, the theoretical rotation curve shown in Figure 19 is obtained. The agreement between the theory and the data for lower angles (e.g. $\theta<30°$) is acceptable; but as the field is rotated into the porphyrin plane, there is rather poor agreement. The cause of this disagreement is not known, but points out the most serious failure of the simple anisotropic Heisenberg model to fit the experimental data.

ESR Transition Rate Analysis

Based on the spin eigenstates, it is possible to calculate which transitions should be observable. The position of the transition in magnetic field gives information about the spacing of the energy levels, and the intensity of the line gives information regarding the matrix elements connecting these energy levels. These matrix elements will now be discussed.

In ESR measurements an oscillating microwave magnetic field, $\underset{\sim}{H}_1 e^{i\omega t}$, is applied to the sample. This microwave field can induce transitions between the eigenstates of the system. The transition probability per unit time between energy levels $E_i$ and $E_j$ is given by the "Golden-Rule" expression[38]:

$$w_{ij} = \frac{\pi H_1^2}{2\hbar^2} |\mu_{ij}|^2 f(\omega) \qquad (82)$$

where $H_1$ is the amplitude of the microwave field. The matrix element $\mu_{ij}$ can be expressed as:

$$\mu_{ij} = \frac{1}{H_1} \langle E_i | \underset{\sim}{\mu} \cdot \underset{\sim}{H}_1 | E_j \rangle \tag{83}$$

where $\underset{\sim}{\mu}$ is the magnetic moment for the ion of interest. The shape factor $f(\omega)$ represents the resonance line shape and has a maximum when $\hbar\omega = E_i - E_j$. The important factor in equation 82 is the matrix element $\mu_{ij}$. For the single crystal measurements, the linearly polarized oscillatory field is applied perpendicular to the DC field, $H_o$, which is rotated in the a-c plane at an angle $\theta$ with respect to the c-axis. The total spin Hamiltonian for the pair becomes:

$$\begin{aligned} H = {} & D_c[S_{1z}^2 + S_{2z}^2 - \tfrac{1}{3}S_1(S_1+1) - \tfrac{1}{3}S_2(S_2+1)] - J_{||} S_{1z}S_{2z} - \tfrac{1}{2}J_{\perp}(S_1^+S_2^- \\ & + S_1^-S_2^+) + g_{||}\mu_\beta H_o \cos\theta(S_{1z}+S_{2z}) + \tfrac{1}{2}g_{\perp}\mu_\beta H_o \sin\theta(S_1^+ + S_1^- + S_2^+ + S_2^-) \\ & + g_{\perp}\mu_\beta H_1 e^{i\omega t}(S_{1y}+S_{2y}) \end{aligned} \tag{84}$$

where the last term on the right represents the time dependent perturbation introducted by the oscillatory field. Thus the dipole matrix element governing the transition rate becomes:

$$\mu_{ij} = \frac{g_{\perp}\mu_\beta}{2i} \langle \phi_i(H_o,\theta) | S_1^+ - S_1^- + S_2^+ - S_2^- | \phi_j(H_o,\theta) \rangle \tag{85}$$

$$\text{where } S_{1y} = \frac{1}{2i}(S_1^+ - S_1^-), \quad S_{2y} = \frac{1}{2i}(S_2^+ - S_2^-) \tag{86}$$

and $S^+$, $S^-$ are the spin-5/2 raising and lowering operators. The strongest pair transition for the 9.30 GHz microwave quantum of the single crystal ESR run is the $\text{triplet}_1$ - $\text{triplet}_2$ transition characterized by $\mu_{12}$ using the subscript

notation mentioned previously. This matrix element was calculated for each angle and field using the computer. The result is a finite transition probability for all angles except $\theta=0°$. At $\theta=0°$, the matrix element is zero. However, the crystal was never aligned well enough to satisfy the $\theta=0°$ condition, so that a resonance line was always observed. The $\theta=90°$ calculation can be done analytically by substituting equations 71 and 73 into equation 85. The result is a non-zero transition rate.

For the powder runs the situation is much more difficult, since all crystallite orientations are possible. This necessitates an averaging over all angles that the c-axis of an individual crystallite might make with respect to the external DC field and the microwave field. For example, in the single crystal run the DC field was fixed to lie in the a-c plane which specifies the z and x component spin operators in the DC Zeeman term. Then the y component spin operator appears in the perpendicular perturbation term. In the powder, however, the microwave field may be perpendicular to the DC field yet still have perturbation components in both the x and z directions for a given crystallite. A detailed calculation of the powder transition rates, including the problem of averaging in the perpendicular plane has not been carried out. (This powder line shape analysis is the next phase of this problem to be attempted.) Instead of the transition calculations, the theoretical energy levels given by the

computer have been checked. It is found that the observed powder transitions occur in exactly the magnetic field ranges where the energy level spacings correspond to the appropriate microwave energy. This is also shown in Figure 20.

There is another possible orientation for the oscillatory field. This is parallel to the large DC magnetic field. It can be shown[42] that, for the standard dipole transitions $M_S \rightarrow M_S \pm 1$, this orientation of the oscillatory field to the DC field gives a zero transition rate. This is true for single ion states of the form $|\pm 1/2\rangle$, $|\pm 3/2\rangle$, etc. However, in the pair system, there is a substantial mixing of the two-ion combination states, especially in the directions away from the z-axis. Thus an oscillatory field along the DC field may still cause a transition. This technique is especially valuable when the presence of other ESR lines may "hide" the existence of an expected transition. In the FeTPPCℓ system, these other lines correspond to the single molecules which exhibit the anisotropic g behavior and are not superexchange coupled. When the DC field is rotated to lie along the oscillatory field, these singles lines disappear leaving only the transitions between mixed states, as well as any forbidden transitions. This is achieved experimentally using a rectangular cavity arrangement where the linearly polarized oscillatory field lies in the same plane in which the DC field can be rotated. (For single crystal rotation studies, a cylindrical cavity is used so that the microwave field is

always perpendicular to the plane in which the DC field is rotated.) The above parallel field technique was used on the FeTPPCℓ system to great advantage to elucidate two transitions. One of these was the low field $singlet_0$-$triplet_{1,2}$ forbidden transition indicated by the shaded region in Figure 20. (The shading indicates that a rather broad absorption peak was seen in the region from 0 to 300 gauss for frequencies in the 9-10 GHz range.) The other transition was the higher $triplet_2$-$triplet_3$ transition which was observed at a K-band frequency of 23.7 GHz. The effect on the ESR spectrum of rotating the DC field parallel to the microwave field is shown in Figure 21 for the low-field singlet-triplet transition and in Figure 23 for the 23.7 GHz triplet-triplet transition. In the case of the 23.7 GHz trace, the fields were never oriented exactly parallel to each other so that the other resonance peaks did not go completely to zero.

Forbidden Singlet-Triplet Transition

Probably the most interesting result of the transition matrix-element analysis is that the singlet-triplet transition should be forbidden regardless of the orientation of the oscillatory field to the DC field. This is a result of the invariance of the pair Hamiltonian to an interchange of the two spins. Because of this invariance, the singlet and triplet states have definite, but opposite, spin parity. The singlet state is odd under interchange of the spins, while the triplet state is even. This is obvious from a quick glance at equations 61-75. Thus, any

even operator will be unable to connect the singlet and triplet states. The oscillatory field which induces the transitions can give rise to perturbation terms of the form:

$$H_{1y}e^{i\omega t}(S_{1y}+S_{2y}),\ H_{1x}e^{i\omega t}(S_{1x}+S_{2x}),\ H_{1z}e^{i\omega t}(S_{1z}+S_{2z}). \quad (87)$$

All of these operators are even under an interchange of the spins and hence will not connect the singlet-triplet states of opposite parity. The fact that an apparent singlet-triplet transition was observed suggests an additional term in the Hamiltonian which breaks the interchange invariance. Such a term is given by the antisymmetric Dzialoshinsky[36]-Moriya[37] term mentioned earlier:

$$\vec{C} \cdot (\vec{S}_1 \times \vec{S}_2) \quad (88)$$

This term is the result of the combined effect of spin-orbit coupling and the superexchange interaction. The constant coupling vector, $\vec{C}$, is strongly dependent on the site symmetry of the superexchange ions. Moriya gives the general rule that $\vec{C}=0$ if a center of inversion symmetry is located midway between the two ions. If one considers an isolated superexchange pair of FeTPPCℓ molecules, the point midway between the adjacent chlorines seems to be an inversion center to the limits of the x-ray determination. However, if one considers the other FeTPPCℓ molecules in the lattice, such inversion symmetry disappears. Thus, the fact that each member of the pair sees a slightly

different field due to the classical dipole-dipole field from neighboring FeTPPCℓ molecules may be sufficient to destroy the interchange invariance between the super-exchange-coupled spins. The Dzialoshinsky-Moriya term was added to the anisotropic Heisenberg term and a non-zero transition probability for the singlet-triplet transition was calculated. This occurs because now the eigenstates are so affected that they are no longer purely antisymmetric and symmetric under an interchange of the spins. Since there is a 4-fold rotation axis along the line joining the superexchange-coupled ions, the constant coupling vector, $\underset{\sim}{C}$ , was chosen to point along this axis (crystalline c-axis) in accordance with the symmetry rules given by Moriya[37]. (This assumes that the interchange invariance has somehow been broken.) The effect on the exchange parameters, $J_{||}$ and $J_{\perp}$, is minimal, resulting in only a re-definition of $J_{\perp}$:

$$J_{\perp}' = (J_{\perp}^2 + C^2)^{\frac{1}{2}} \tag{89}$$

Thus, the Dzialoshinsky-Moriya term has the appeal of explaining the observed singlet-triplet transition without affecting significantly the best-fit parameters to the experimental data. However, the existence of such a term implies a lack of interchange symmetry within the pair.

# CHAPTER VI

## SUMMARY AND CONCLUSIONS

The unique structure of FeTPPCl gives rise to a system composed of superexchange-coupled pairs plus isolated single paramagnetic molecules (neglecting the weak classical dipolar coupling). 50% of the molecules form pairs. The dominant term in the single-ion spin Hamiltonian is the second order spin-orbit coupling via the crystal-field-split orbital states. This gives rise to the large single ion anisotropy in the Lande g factor. The resultant crystal field coupling parameter, $D_c/k_B$, is approximately 13 K, and is the dominant term at low temperatures (e.g. $T < 4$ K). In addition to this single ion interaction, the pairs have a superexchange splitting of the pair ground state which is much smaller than the crystal electric field parameter, $D_c$. Also, the origins of the large single ion anisotropy may be responsible for the large anisotropy in the superexchange parameters. The z-component of the exchange coupling, $J_{||}$, is opposite in sign to the perpendicular component, $J_{\perp}$. This system appears to have one of the most anisotropic exchange couplings ever seen. Such a large anisotropy is especially unusual for S-state ions. In addition, the small values

for $J_{||}$ and $J_{\perp}$ (<0.5 K) cause the superexchange split energies to have values such that transitions between these levels fall within the microwave energy spectrum. ESR transitions have been observed and confirm the anisotropic Heisenberg model chosen. A consequence of the pairing is the classification of the exchange-split ground-state energies into a singlet and a zero-field-split triplet. The transition between the singlet and the triplet states should be forbidden due to the invariance of the spin Hamiltonian under an interchange of the spins. However, the singlet-triplet transition in very low fields has been observed at just the microwave energies predicted by the best-fit values of $J_{||}$ and $J_{\perp}$. The presence of this forbidden transition suggests an additional term in the Hamiltonian is needed to break the spin-interchange invariance. The Dzialoshinsky-Moriya antisymmetric exchange has this property, but dictates that the point midway between the elements of the pair cannot be a center of inversion. The presence of the long range classical dipole fields due to the neighboring single ions may be the cause for the breaking of the interchange invariance; but, as yet, no calculations have been done to substantiate this possibility.

Due to the simple pairs-singles combination structure, there are no long range correlations (neglecting weak dipole-dipole effects) so that a straightforward theoretical solution is possible. Using an anisotropic Heisenberg exchange term as a perturbation on the crystal field term,

an analytic solution for the ground state pair energies is obtained. These energy eigenvalues allow for the calculation of all the relevant thermodynamic quantities, particularly the magnetic susceptibility and the heat capacity. The magnetic susceptibility was measured in both the parallel and perpendicular directions to the crystalline c-axis and agrees well with the theory when best fit values for $J_{||}$ , $J_{\perp}$ , and $\alpha/N$ (the fraction of pairs) are used. The heat capacity was also measured and agrees with the theory based on the same best fit values. These values give rise to energy levels which have been verified by direct ESR measurements. The best fit values for these quantities are:

$$J_{||}/k_B = (+0.40 \pm .03)\,K$$

$$J_{\perp}/k_B = (-.1525 \pm .003)\,K$$

$$\alpha/N = .255 \pm .004$$

where the error bars indicate the range within which the comparison of theory with data yields a reasonable fit.

The only rather disappointing aspect of these measurements is the poor fit of the $triplet_1$-$triplet_2$ ESR rotation data to the theory. The energy levels given by the computer diagonalization yield a reasonable fit at the angles when the field is oriented near the c-axis ($\theta < 30°$), but give a poor fit for the larger angles. The implication is that the $triplet_1$-$triplet_2$ energy levels have a different curvature as a function of magnetic field at the larger angles

than is predicted by the simple model. Another possibility is that the 1-2 components of the triplet may be split in zero field by a rhombic distortion term on each ion, such as $E_c(S_x^2-S_y^2)$. (The ratio $E_c/D_c$ has been chosen as large as .03 to interpret the ESR spectra of some heme complexes.[22]) For example, a value of $E_c/D_c$ of .004 gives a zero-field energy-splitting of .04 K between the $triplet_1$-$triplet_2$ levels for FeTPPCl. However, the original x-ray work is unable to confirm such a distortion. This leads one to the conclusion that there may be higher order exchange terms needed to explain the pair rotation diagram. Also, the inclusion of fourth-order crystal-field terms in the single-ion Hamiltonian may be necessary. Marathe and Mitra[43] pointed out that such terms could explain the discrepancy between the value for $D_c(10\ K)$ obtained by Richards and co-workers[23] for hemin from infrared absorption data and the value for $D_c(17\ K)$ obtained by Maricondi et.al.[44] from susceptibility data. It is clear that more accurate ESR measurements on large single crystals (e.g. 1 mgm or larger) should yield better information on the field dependence of all four of the pair ground state levels.

The superexchange coupling is highly anisotropic and can be expressed in an isotropic-plus-pseudodipolar form:

$$J_\perp(S_{1x}S_{2x}+S_{1y}S_{2y})+J_{||}\,S_{1z}S_{2z} = J(S_1\cdot S_2)+D_e(3S_{1z}S_{2z}-S_1\cdot S_2) \quad (90)$$

where $$J = \frac{1}{3}(2J_\perp+J_{||}) \quad (91)$$

is the isotropic coupling parameter and $$D_e = \frac{1}{3}(J_{||}-J_\perp) \quad (92)$$

is the pseudodipolar parameter.

Using the best fit values for $J_{||}$ and $J_{\perp}$, these new coupling coefficients have the values: $J/k_B = (+.03 \pm .01)$ K, and $D_e/k_B = (+.184 \pm .01)$ K. The classical interaction energy of two point magnetic dipoles $\underset{\sim}{\mu}_1$ and $\underset{\sim}{\mu}_2$ may be expressed as

$$H_d = \frac{1}{r^3}\left[\underset{\sim}{\mu}_1 \cdot \underset{\sim}{\mu}_2 - (3/r^2)(\underset{\sim}{\mu}_1 \cdot \underset{\sim}{r})(\underset{\sim}{\mu}_2 \cdot \underset{\sim}{r})\right] \tag{93}$$

where $\underset{\sim}{r}$ is the vector joining the two dipoles. For FeTPPCl this equation can be written in the form:

$$H_d = D_d(3S_{1z}S_{2z} - \underset{\sim}{S}_1 \cdot \underset{\sim}{S}_2) \tag{94}$$

where $D_d = -g^2 \mu_B^2/r^3$ ; and $z$ is along the line joining the dipoles. Hence the name pseudodipolar is applied to the anisotropic part of the superexchange Hamiltonian in equation 90, since it can be cast in this form. The classical dipole-dipole coupling between the iron ions within the pair is small. The value for the dipole coupling parameter is $D_d/k_B = -.003$ K for the 9.05 Å distance between the two $Fe^{3+}$ ions of the pair. Thus the superexchange coupling is primarily pseudodipolar in nature. As originally pointed out by Van Vleck[45], pseudodipolar exchange can arise from spin-orbit effects. Since spin-orbit coupling to a rather low lying excited state of the $Fe^{3+}$ ion is responsible for the large crystal-field parameter, $D_c$, it is possible that such spin-orbit coupling may be the origin of this pseudodipolar exchange.

In conclusion, the major contribution of this work is to provide some accurately determined superexchange coupling parameters, $J_{||}$ and $J_{\perp}$, which can be compared to a theoretical calculation of the superexchange mechanism. The lack of long range correlations due to the isolation of the pairs makes the FeTPPCl system a relatively simple one for such a calculation. It is suggested that a starting point of such a calculation should consider the excited orbital states on the iron ions as possible intermediate states for the superexchange electrons. In addition, it should be pointed out that there are iodide and bromide forms of the high-spin $Fe^{3+}$ tetraphenylporphyrins. Although their crystal structures are not known, certainly the possibility of spin pairing exists. The superexchange coupling for these compounds would probably be different due to the larger ionic radii of the halogen ligands.

# LIST OF REFERENCES

## LIST OF REFERENCES


1. J. L. Hoard, Science 174, 1295 (1971).
2. J. E. Falk, Porphyrins and Metalloporphyrins (Elsevier Publishing Company, 1964).
3. J. L. Imes, G. L. Neiheisel and W. P. Pratt, Jr., Phys. Letters 49A, 351 (1974).
4. J. H. Bishop et.al., J. Low Temp. Phys. 10, 379 (1973).
5. J. Owen and E. A. Harris, in Electron Paramagnetic Resonance, ed. by S. Geschwind (Plenum Press, New York-London, 1972), p. 427; and references therein.
6. Ph.D. thesis, J. L. Imes, Michigan State University, 1974.
7. J. C. Wheatley, Am. J. Phys. 36, 181 (1968).
8. A. C. Mota, Rev. of Sci. Instr. 42, 1541 (1971).
9. A. C. Anderson, R. E. Peterson and J. E. Robichaux, Rev. of Sci. Instr. 41, 4 (1970).
10. Airco Central Research Laboratories, Murray Hill, New Jersey.
11. B. D. Josephson, Phys. Letters 1, 251 (1962).
12. J. Lambe, A. H. Silver, J. E. Mercereau and R. C. Jaklevic, Phys. Letters 11, 16 (1964).
13. R. P. Giffard, R. A. Webb and J. C. Wheatley, J. Low Temp. Phys. 6, 533 (1972).
14. S. H. E. Corporation, 3422 Tripp Court, Suite B, San Diego, California, 92121.
15. Wilbur B. Driver Co., Newark, New Jersey.
16. Apiezon Products Ltd., London, England.

17. Handbook of Chemistry and Physics (The Chemical Rubber Co., Cleveland, Ohio), 46th Edition (1965-66), p. E-68.

18. CR-50 $^{3}$He gas-filled germanium resistor. Cryo Cal Inc., P.O. Box 10176, 1371 Avenue "E", Riviera Beach, Florida, 33404.

19. CR-100 $^{3}$He gas-filled germanium resistor. Cryo Cal Inc., see reference 18 for address.

20. P. S. Han, T. P. Das and M. F. Rettig, J. Chem. Phys. 56, 3861 (1972).

21. R. M. White, Quantum Theory of Magnetism (McGraw Hill Book Co., 1970), p. 57.

22. C. P. Scholes, J. Chem. Phys. 52, 4890 (1970); and references therein.

23. P. L. Richards, W. S. Caughey, H. Eberspacher, G. Feher and M. Malley, J. Chem. Phys. 47, 1187 (1967).

24. E. B. Fleischer, C. K. Miller, and L. E. Webb, J. Am. Chem. Soc. 86, 2342 (1964).

25. J. L. Hoard, C. H. Cohen, and M. D. Glick, J. Am. Chem. Soc. 89, 1992 (1967).

26. H. E. Megaw, Crystal Structures: A Working Approach (W. B. Saunders Publishing Co., 1973), pp 26-27.

27. C. Butterfield and E. H. Carlson, J. Chem. Phys. 56, 4907 (1972).

28. Strem Chemicals Inc., 150 Andover St., Danvers, Mass. 01923.

29. J. A. Ibers and J. D. Swallen, Phys. Rev. 127, 1914 (1962).

30. P. R. Bevington, Data Reduction and Error Analysis for the Physical Sciences (McGraw-Hill Book Co., 1969), p 52.

31. H. Morimoto and M. Kotani, Biochim. Biophys. Acta 126, 176 (1966).

32. J. H. Van Vleck, J. Chem. Phys. 5, 320 (1937).

33. J. M. Daniels, Proc. Phys. Soc. A66, 673 (1953).

34. J. R. Peverley, J. Computational Physics 7, 83 (1971).

35. P. W. Anderson, in Solid State Physics Vol. 14, F. Seitz and D. Turnbull, editors (Academic Press, New York, 1963), p. 99.

36. I. Dzialoshinsky, J. Phys. Chem. Solids 4, 241 (1958).

37. T. Moriya, Phys. Rev. 120, 91 (1960).

38. A. Abragam and B. Bleaney, Electron Paramagnetic Resonance of Transition Ions (Clarendon Press, Oxford, 1970), p. 493.

39. J. P. Franck, F. D. Manchester, and D. L. Martin, Proc. Roy. Soc. (London), Ser. A 263, 494 (1961).

40. M. Wun and J. E. Phillips, Cryogenics 15, 36 (1975).

41. Handbook of Chemistry and Physics, op. cit., p. D-86.

42. A. Abragam and B. Bleaney, op. cit., pp. 136-137.

43. V. R. Marathe and S. Mitra, Chem. Phys. Letters 19, 140 (1973).

44. C. Maricondi, W. Swift and D. K. Straub, J. Am. Chem. Soc. 91, 5205 (1969).

45. J. H. Van Vleck, Phys. Rev. 52, 1178 (1937).

# APPENDIX A

# APPENDIX A

## Tabulation of Experimental Data

The magnetic susceptibility data for an aligned single crystal and for a powdered sample of FeTPPCℓ are presented. The zero-field heat capacity data are given. In addition, the calibration data for the CR-50 resistor used in the heat capacity measurements are listed.

Table A.1. Calibration Data for CR-50 Germanium Resistor.

| Resistance (ohms) | Inverse T ($K^{-1}$) | Resistance (ohms) | Inverse T ($K^{-1}$) |
|---|---|---|---|
| 53.2 | .238 | 158.3 | 1.299 |
| 54.1 | .249 | 185.8 | 1.534 |
| 56.1 | .262 | 208.7 | 1.727 |
| 58.8 | .286 | 214.5 | 1.764 |
| 61.1 | .309 | 218.5 | 1.815 |
| 63.6 | .334 | 240.7 | 1.988 |
| 66.6 | .361 | 250.7 | 2.053 |
| 73.0 | .428 | 259.7 | 2.110 |
| 75.7 | .452 | 265.7 | 2.165 |
| 80.0 | .501 | 276.6 | 2.242 |
| 89.9 | .596 | 281.7 | 2.273 |
| 92.3 | .628 | 284.7 | 2.299 |
| 93.7 | .652 | 300.0 | 2.403 |
| 96.8 | .684 | 309.7 | 2.463 |
| 105.0 | .765 | 321.0 | 2.544 |
| 108.8 | .801 | 350.6 | 2.714 |
| 112.9 | .845 | 405.6 | 3.031 |
| 118.9 | .912 | 453.9 | 3.278 |
| 128.6 | 1.010 | 461.9 | 3.313 |
| 136.3 | 1.085 | 489.0 | 3.444 |
| 136.6 | 1.091 | 520.8 | 3.613 |
| 148.4 | 1.202 | 605.0 | 3.945 |
| 150.4 | 1.224 | 668.0 | 4.191 |
| 153.0 | 1.245 | 767.0 | 4.548 |

Table A.1. (continued)

| Resistance (ohms) | Inverse T ($K^{-1}$) | Resistance (ohms) | Inverse T ($K^{-1}$) |
|---|---|---|---|
| 827.0 | 4.735 | 2736.0 | 8.310 |
| 877.0 | 4.900 | 2975.0 | 8.617 |
| 1005.0 | 5.243 | 3215.0 | 8.884 |
| 1080.0 | 5.429 | 3725.0 | 9.416 |
| 1171.0 | 5.652 | 4836.0 | 10.370 |
| 1331.0 | 6.004 | 4907.0 | 10.458 |
| 1468.0 | 6.329 | 5082.0 | 10.563 |
| 1626.0 | 6.664 | 7302.0 | 12.063 |
| 2036.0 | 7.345 | 9950.0 | 13.379 |
| 2185.0 | 7.599 | 12,100.0 | 14.080 |
| 2372.0 | 7.825 | 28,020.0 | 18.603 |
| 2566.0 | 8.074 | 53,060.0 | 22.416 |

Table A.2. The magnetic susceptibility data for a .1875 gm powdered sample of FeTPPCℓ.

| $\chi_{powder}$ (emu/mole) | Inverse T* ($K^{-1}$) | $\chi_{powder}$ (emu/mole) | Inverse T* ($K^{-1}$) |
|---|---|---|---|
| .506 | .238 | 4.690 | 3.061 |
| .573 | .268 | 4.730 | 3.098 |
| .737 | .339 | 4.737 | 3.111 |
| .828 | .388 | 5.597 | 4.066 |
| 1.101 | .515 | 5.975 | 4.400 |
| 1.230 | .593 | 5.992 | 4.417 |
| 1.437 | .694 | 9.032 | 7.825 |
| 1.614 | .794 | 14.596 | 14.662 |
| 1.783 | .888 | 19.880 | 22.445 |
| 1.985 | 1.000 | 23.161 | 28.405 |
| 2.147 | 1.063 | 26.741 | 35.347 |
| 2.320 | 1.196 | 32.237 | 49.511 |
| 2.481 | 1.341 | 36.057 | 62.553 |
| 2.600 | 1.422 | 39.091 | 75.736 |
| 2.882 | 1.584 | 42.141 | 92.527 |
| 3.190 | 1.784 | 44.186 | 106.607 |
| 3.481 | 2.009 | 44.335 | 107.839 |
| 3.764 | 2.234 | 47.334 | 133.324 |
| 3.782 | 2.244 | 51.515 | 183.132 |
| 4.135 | 2.518 | 53.543 | 212.420 |
| 4.550 | 2.922 | 54.456 | 226.595 |

Table A.3. The magnetic susceptibility data for a 0.1 mgm single crystal of FeTPPCℓ oriented with the applied DC magnetic field at an angle of 10° from the crystalline c-axis.

| $\chi_{\|\|}$ (emu/mole) | Inverse T* ($K^{-1}$) | $\chi_{\|\|}$ (emu/mole) | Inverse T* ($K^{-1}$) |
|---|---|---|---|
| .196 | .487 | 1.118 | 3.067 |
| .218 | .533 | 1.498 | 4.901 |
| .246 | .604 | 2.187 | 8.437 |
| .281 | .693 | 3.998 | 17.504 |
| .344 | .850 | 5.720 | 26.953 |
| .534 | 1.332 | 7.088 | 35.882 |
| .581 | 1.473 | 9.443 | 53.464 |
| .587 | 1.508 | 11.486 | 74.050 |
| .628 | 1.628 | 12.714 | 93.160 |
| .699 | 1.790 | 12.737 | 93.438 |
| .795 | 2.033 | 12.748 | 93.612 |
| .855 | 2.210 | 13.438 | 109.039 |
| .920 | 2.408 | 13.478 | 110.143 |
| .996 | 2.649 | 14.335 | 154.739 |
| 1.077 | 2.928 | 14.723 | 187.752 |

Table A.4. The magnetic susceptibility data for a 0.1 mgm single crystal of FeTPPCℓ oriented with the applied DC magnetic field perpendicular to the crystalline c-axis.

| $\chi_{\perp}$ (emu/mole) | Inverse T* ($K^{-1}$) | $\chi_{\perp}$ (emu/mole) | Inverse T* ($K^{-1}$) |
|---|---|---|---|
| .722 | .238 | 6.400 | 3.012 |
| 1.406 | .465 | 6.558 | 3.116 |
| 1.669 | .550 | 8.680 | 4.730 |
| 1.677 | .553 | 12.798 | 8.022 |
| 1.818 | .612 | 24.585 | 18.265 |
| 2.100 | .728 | 34.985 | 28.997 |
| 2.424 | .855 | 41.292 | 38.262 |
| 2.696 | .996 | 47.622 | 48.924 |
| 2.844 | 1.038 | 53.150 | 63.327 |
| 3.539 | 1.309 | 56.587 | 75.562 |
| 3.781 | 1.450 | 59.309 | 88.338 |
| 4.405 | 1.750 | 60.706 | 95.042 |
| 4.677 | 1.915 | 63.696 | 114.900 |
| 4.890 | 2.055 | 63.670 | 115.430 |
| 5.173 | 2.223 | 68.878 | 174.634 |
| 5.522 | 2.416 | 69.074 | 190.786 |
| 5.626 | 2.521 | 68.681 | 202.032 |
| 5.814 | 2.616 | 68.950 | 217.145 |
| 6.094 | 2.808 | | |

Table A.5. The zero-field heat capacity data for FeTPPCℓ. The data presented here are the molar heat capacities, $C = (\Delta Q/\Delta T)(\frac{M}{m})$, divided by the molar gas constant, R. The inverse temperatures are the average values for the interval before and after the application of the heat pulse.

| C/R | $(\text{Inverse T})_{AVG}$ ($K^{-1}$) | C/R | $(\text{Inverse T})_{AVG}$ ($K^{-1}$) |
|---|---|---|---|
| .0585 | .974 | .1571 | 3.140 |
| .0700 | 1.133 | .1581 | 3.320 |
| .0751 | 1.158 | .1667 | 3.490 |
| .0689 | 1.253 | .1754 | 3.662 |
| .0814 | 1.406 | .1738 | 3.696 |
| .0781 | 1.449 | .1680 | 3.942 |
| .0885 | 1.604 | .1797 | 3.876 |
| .0995 | 1.858 | .1814 | 3.941 |
| .1190 | 1.969 | .1823 | 4.059 |
| .1153 | 2.182 | .1841 | 4.124 |
| .1315 | 2.538 | .1885 | 4.358 |
| .1369 | 2.637 | .1916 | 4.468 |
| .1499 | 2.642 | .1960 | 4.518 |
| .1447 | 2.686 | .1956 | 4.611 |
| .1382 | 2.706 | .1842 | 4.671 |
| .1483 | 2.805 | .1963 | 4.711 |
| .1490 | 2.857 | .2007 | 4.793 |
| .1495 | 2.952 | .1905 | 4.839 |
| .1536 | 3.024 | .1890 | 5.056 |
| .1910 | 5.073 | .1791 | 6.890 |

Table A.5. (continued)

| C/R | (Inverse T)$_{AVG}$ ($K^{-1}$) | C/R | (Inverse T)$_{AVG}$ ($K^{-1}$) |
|---|---|---|---|
| .1964 | 5.147 | .1839 | 6.951 |
| .1852 | 5.253 | .1784 | 7.052 |
| .1851 | 5.404 | .1836 | 7.097 |
| .1840 | 5.459 | .1799 | 7.208 |
| .1984 | 5.490 | .1777 | 7.257 |
| .1909 | 5.524 | .1758 | 7.380 |
| .1752 | 5.596 | .1567 | 7.393 |
| .1912 | 5.618 | .1676 | 7.404 |
| .1849 | 5.643 | .1724 | 7.549 |
| .1911 | 5.728 | .1734 | 7.702 |
| .1825 | 5.747 | .1383 | 8.029 |
| .1713 | 5.754 | .1599 | 8.169 |
| .1718 | 5.864 | .1312 | 8.330 |
| .1740 | 5.926 | .1500 | 8.531 |
| .1943 | 6.002 | .1273 | 8.652 |
| .1832 | 6.121 | .1002 | 9.257 |
| .2002 | 6.269 | .1047 | 9.465 |
| .1756 | 6.413 | .1041 | 9.638 |
| .1780 | 6.506 | .0794 | 9.830 |
| .1705 | 6.658 | .0872 | 10.105 |
| .1732 | 6.818 | | |

# APPENDIX B

## APPENDIX B

## THEORETICAL CALCULATION OF THE PAIR GROUND-STATE SUPEREXCHANGE-SPLIT ENERGY LEVELS

The case with the external DC magnetic field oriented perpendicular to the crystalline c-axis will be treated since it represents a more difficult calculation than the parallel case. The spin Hamiltonian for the pair of interest is given by:

$$H_{pair} = D_c(S_{1z}^2+S_{2z}^2) - J_{||} S_{1z}S_{2z} - J_{\perp}(S_{1x}S_{2x} + S_{1y}S_{2y}) + g_{\perp}\mu_B H_o (S_{1x}+S_{2x}) \qquad (B1)$$

where the field $H_o$ has been chosen to lie along the x-axis. (Because of the 4-fold rotational symmetry about the c-axis, the result is the same regardless of where the field is oriented in the x-y plane.) It should be noted that the terms $\frac{1}{3} S_1 (S_1+1)D_c + \frac{1}{3} S_2(S_2+1)D_c$ have been omitted since they represent an additive constant. This Hamiltonian can be re-written using the raising and lowering operators $S^+ = S_x + iS_y$ , $S^- = S_x - iS_y$ as:

$$H_{pair} = D_c(S_{1z}^2+S_{2z}^2)-J_{||} S_{1z}S_{2z} - \frac{1}{2} J_{\perp}(S_1^+S_2^- + S_1^-S_2^+)$$
$$+ h_{\perp}(S_1^++S_1^- + S_2^++S_2^-) \qquad \text{(B2)}$$

$$\text{where} \quad h_{\perp} = \frac{1}{2} g_{\perp}\mu_B H_o \ , \quad g_{\perp} = 2.00 \ . \qquad \text{(B3)}$$

Since the crystal-field spin-orbit term characterized by the crystal-field parameter, $D_c$ , represents the largest interaction in the spin Hamiltonian at low temperatures ($k_BT << 2\ D_c$) , we shall treat this term as the unperturbed Hamiltonian. Thus the c-crystalline axis represents the axis of spin quantization, and the resulting unperturbed spin eigenstates are:

$$|\tfrac{1}{2},\tfrac{1}{2}>,\ |\tfrac{1}{2},-\tfrac{1}{2}>,\ |-\tfrac{1}{2},\tfrac{1}{2}>,\ |-\tfrac{1}{2},-\tfrac{1}{2}>,$$
$$|\tfrac{1}{2}\ \tfrac{3}{2}>,\ |\tfrac{1}{2},-\tfrac{3}{2}>,\ |-\tfrac{1}{2},\tfrac{3}{2}>,\ |-\tfrac{1}{2},-\tfrac{3}{2}>, \text{ etc.} \qquad \text{(B4)}$$

Since the spin on each iron ion in the pair is 5/2, there are 36 such states. However, since the crystal-field parameter, $D_c$ , is positive definite, the ground state will result from combinations of the first four states in equation B4. Thus

$$H_o = D_c(S_{1z}^2 + S_{2z}^2) \ , \qquad \text{(B5)}$$

and the unperturbed energies, $E_i^{(0)}$, are given by:

$$D_c(S_{1z}^2+S_{2z}^2) = \frac{1}{2} D_c \quad \text{for} \quad S_{1z} = \pm \frac{1}{2} , \; S_{2z} = \pm \frac{1}{2} \tag{B6}$$

$$D_c(S_{1z}^2+S_{2z}^2) = \frac{5}{2} D_c \quad \text{for} \quad S_{1z} = \pm \frac{1}{2} , \; S_{2z} = \pm \frac{3}{2} \tag{B7}$$

$$D_c(S_{1z}^2+S_{2z}^2) = \frac{5}{2} D_c \quad \text{for} \quad S_{1z} = \pm \frac{3}{2} , \; S_{2z} = \pm \frac{1}{2} \tag{B8}$$

$$D_c(S_{1z}^2+S_{2z}^2) = \frac{9}{2} D_c \quad \text{for} \quad S_{1z} = \pm \frac{3}{2} , \; S_{2z} = \pm \frac{3}{2} \tag{B9}$$

etc.

The perturbation is then given by the exchange plus Zeeman terms:

$$H'_{\perp} = -J_{||} S_{1z}S_{2z} - \frac{1}{2} J_{\perp}(S_1^+S_2^- + S_1^-S_2^+) + h_{\perp}(S_1^++S_1^- + S_2^++S_2^-) \tag{B10}$$

where $S_{1z}$, $S_{2z}$, $S_1^+$, $S_1^-$, $S_2^+$, $S_2^-$ are spin 5/2 operators.

Using the first four states in equation B4, the 4x4 ground state subspace of $H'_{\perp}$ is given by:

| $H'_{\perp}$ | $\lvert\frac{1}{2},\frac{1}{2}\rangle$ | $\lvert-\frac{1}{2},-\frac{1}{2}\rangle$ | $\lvert\frac{1}{2},-\frac{1}{2}\rangle$ | $\lvert-\frac{1}{2},\frac{1}{2}\rangle$ |
|---|---|---|---|---|
| $\langle\frac{1}{2},\frac{1}{2}\rvert$ | $-\frac{J_{||}}{4}$ | 0 | $3h_{\perp}$ | $3h_{\perp}$ |
| $\langle-\frac{1}{2},-\frac{1}{2}\rvert$ | 0 | $-\frac{J_{||}}{4}$ | $3h_{\perp}$ | $3h_{\perp}$ |
| $\langle\frac{1}{2},-\frac{1}{2}\rvert$ | $3h_{\perp}$ | $3h_{\perp}$ | $\frac{J_{||}}{4}$ | $-\frac{9J_{\perp}}{2}$ |
| $\langle-\frac{1}{2},\frac{1}{2}\rvert$ | $3h_{\perp}$ | $3h_{\perp}$ | $-\frac{9J_{\perp}}{2}$ | $\frac{J_{||}}{4}$ |

(B11)

Now this 4x4 matrix can be easily solved if a new set of basis states are chosen. Because of the effective spin=1 nature of this 4x4 subspace, these new basis states are chosen as a singlet and three triplet states:

SINGLET: $$|\psi_o\rangle = \frac{1}{\sqrt{2}} \{|-\tfrac{1}{2},\tfrac{1}{2}\rangle - |\tfrac{1}{2},-\tfrac{1}{2}\rangle\} \quad \text{(B12)}$$

$$|\psi_1\rangle = |\tfrac{1}{2},\tfrac{1}{2}\rangle \quad \text{(B13)}$$

TRIPLET: $$|\psi_2\rangle = |-\tfrac{1}{2},-\tfrac{1}{2}\rangle \quad \text{(B14)}$$

$$|\psi_3\rangle = \frac{1}{\sqrt{2}} \{|-\tfrac{1}{2},\tfrac{1}{2}\rangle + |\tfrac{1}{2},-\tfrac{1}{2}\rangle\} \quad \text{(B15)}$$

The perturbed Hamiltonian can now be written as:

$H'_\perp$

| | $\|\psi_o\rangle$ | $\|\psi_1\rangle$ | $\|\psi_2\rangle$ | $\|\psi_3\rangle$ |
|---|---|---|---|---|
| $\langle\psi_o\|$ | $\frac{J_\parallel}{4} + \frac{9J_\perp}{2}$ | 0 | 0 | 0 |
| $\langle\psi_1\|$ | 0 | $-\frac{J_\parallel}{4}$ | 0 | $3\sqrt{2}\, h_\perp$ |
| $\langle\psi_2\|$ | 0 | 0 | $-\frac{J_\parallel}{4}$ | $3\sqrt{2}\, h_\perp$ |
| $\langle\psi_3\|$ | 0 | $3\sqrt{2}h_\perp$ | $3\sqrt{2}h_\perp$ | $\frac{J_\parallel}{4} - \frac{9J_\perp}{2}$ |

(B16)

This formulation immediately yields the singlet energy shift and eigenstate to first order as:

$$\Delta E_o^{(1)} = \frac{J_\parallel}{4} + \frac{9J_\perp}{2} \Longrightarrow E_o^{(1)} = \frac{D_c}{2} + \frac{J_\parallel}{4} + \frac{9J_\perp}{2} \quad \text{(B17)}$$

$$|\phi_o\rangle = |\psi_o\rangle = \frac{1}{\sqrt{2}} \{|-\tfrac{1}{2},\tfrac{1}{2}\rangle - |\tfrac{1}{2},-\tfrac{1}{2}\rangle\} \quad \text{(B18)}$$

The remaining 3x3 subspace of $|\psi_1\rangle$, $|\psi_2\rangle$, and $|\psi_3\rangle$ yields a secular equation which factors into a linear term multiplying a quadratic term. This is easily solved to yield the first-order triplet energy shifts as:

$$\Delta E_1^{(1)} = -\frac{9J_\perp}{4} - \frac{A}{2} \Rightarrow E_1^{(1)} = \frac{D_c}{2} - \frac{9J_\perp}{4} - \frac{A}{2} \tag{B19}$$

$$\Delta E_2^{(1)} = -\frac{J_\parallel}{4} \Rightarrow E_2^{(1)} = \frac{D_c}{2} - \frac{J_\parallel}{4} \tag{B20}$$

$$\Delta E_3^{(1)} = -\frac{9J_\perp}{4} + \frac{A}{2} \Rightarrow E_3^{(1)} = \frac{D_c}{2} - \frac{9J_\perp}{4} + \frac{A}{2} \tag{B21}$$

$$\text{where} \quad A = \left[ (J_\parallel - 9J_\perp)^2/4 + (12\, h_\perp)^2 \right]^{\frac{1}{2}} \tag{B22}$$

and the adapted eigenstates which diagonalize the 3x3 subspace are given in Chapter V by equations 71, 73, and 75. The same notation of $|\phi_1\rangle$, $|\phi_2\rangle$, and $|\phi_3\rangle$ will be used to refer to these eigenstates.

Now to obtain the second and third-order energy shifts it is necessary to label all the pertinent states. The following notation will be used:

$|\phi_o\rangle$, $|\phi_1\rangle$, $|\phi_2\rangle$, $|\phi_3\rangle$ as given in Chapter V,

$$|\mu_5\rangle = |\tfrac{1}{2},\tfrac{3}{2}\rangle \quad , \quad |\mu_6\rangle = |\tfrac{1}{2},-\tfrac{3}{2}\rangle \tag{B23}$$

$$|\mu_7\rangle = |-\tfrac{1}{2},\tfrac{3}{2}\rangle \quad , \quad |\mu_8\rangle = |-\tfrac{1}{2},-\tfrac{3}{2}\rangle \tag{B24}$$

$$|\mu_9\rangle = |\tfrac{3}{2},\tfrac{1}{2}\rangle \quad , \quad |\mu_{10}\rangle = |\tfrac{3}{2},-\tfrac{1}{2}\rangle \tag{B25}$$

$$|\mu_{11}\rangle = |-\tfrac{3}{2},\tfrac{1}{2}\rangle \quad , \quad |\mu_{12}\rangle = |-\tfrac{3}{2},-\tfrac{1}{2}\rangle \tag{B26}$$

$$|\mu_{13}\rangle = |\tfrac{3}{2},-\tfrac{3}{2}\rangle \quad , \quad |\mu_{14}\rangle = |-\tfrac{3}{2},\tfrac{3}{2}\rangle \quad .$$

These are the only states from the total of 36 which give matrix elements contributing to the pair ground state levels when 2nd and 3rd order perturbation theory is used.

For the singlet state, the second-order energy shift is given by

$$\Delta E_o^{(2)} = \sum_{i=5}^{14} \frac{|\langle \phi_o | H_\perp' | \mu_i \rangle|^2}{E_o^{(o)} - E_i^{(o)}} \tag{B28}$$

where $$E_o^{(o)} = \frac{1}{2} D_c \tag{B29}$$

and $$E_i^{(o)} = \frac{5}{2} D_c \quad \text{for} \quad i = 5,12 \tag{B30}$$

$$E_i^{(o)} = \frac{9}{2} D_c \quad \text{for} \quad i = 13,14 \tag{B31}$$

are the unperturbed energies. The third-order shift is given by the expression:

$$\Delta E_o^{(3)} = \sum_{i=5}^{14} \sum_{j=5}^{14} \frac{\langle \phi_o | H_\perp' | \mu_i \rangle \langle \mu_i | H_\perp' | \mu_j \rangle \langle \mu_j | H_\perp' | \phi_o \rangle}{(E_o^{(o)} - E_i^{(o)})(E_o^{(o)} - E_j^{(o)})} \tag{B32}$$

Since $\underset{\approx}{H}'_{\perp}$ is a real symmetric matrix, only half of the off-diagonal terms will be presented. To fit all the terms on a page, the 14x14 matrix will be given in two parts:

| $H'_{\perp}$ | $\lvert\phi_o\rangle$ | $\lvert\phi_1\rangle$ | $\lvert\phi_2\rangle$ | $\lvert\phi_3\rangle$ | $\lvert\mu_5\rangle$ | $\lvert\mu_6\rangle$ | $\lvert\mu_7\rangle$ |
|---|---|---|---|---|---|---|---|
| $\langle\phi_o\rvert$ | $\frac{J_{\parallel}}{4}+\frac{9J_{\perp}}{2}$ | | | | | | |
| $\langle\phi_1\rvert$ | 0 | $-\frac{9J_{\perp}}{4}-\frac{A}{2}$ | | | | | |
| $\langle\phi_2\rvert$ | 0 | 0 | $-\frac{J_{\parallel}}{4}$ | | | | |
| $\langle\phi_3\rvert$ | 0 | 0 | 0 | $-\frac{9J_{\perp}}{4}+\frac{A}{2}$ | | | |
| $\langle\mu_5\rvert$ | 0 | a | $2h_{\perp}$ | q | $-\frac{3}{4}J_{\parallel}$ | | |
| $\langle\mu_6\rvert$ | $-2h_{\perp}$ | -c | $3J_{\perp}$ | -b | 0 | $\frac{3}{4}J_{\parallel}$ | |
| $\langle\mu_7\rvert$ | $+2h_{\perp}$ | -c | $-3J_{\perp}$ | -b | $3h_{\perp}$ | 0 | $\frac{3}{4}J_{\parallel}$ |
| $\langle\mu_8\rvert$ | 0 | a | $-2h_{\perp}$ | q | 0 | $3h_{\perp}$ | 0 |
| $\langle\mu_9\rvert$ | 0 | a | $2h_{\perp}$ | q | $-4J_{\perp}$ | 0 | 0 |
| $\langle\mu_{10}\rvert$ | $-2h_{\perp}$ | -c | $-3J_{\perp}$ | -b | 0 | 0 | 0 |
| $\langle\mu_{11}\rvert$ | $+2h_{\perp}$ | -c | $3J_{\perp}$ | -b | 0 | 0 | 0 |
| $\langle\mu_{12}\rvert$ | 0 | a | $-2h_{\perp}$ | q | 0 | 0 | 0 |
| $\langle\mu_{13}\rvert$ | j | e | 0 | d | 0 | $2\sqrt{2}\,h_{\perp}$ | 0 |
| $\langle\mu_{14}\rvert$ | -j | e | 0 | d | 0 | 0 | $2\sqrt{2}\,h_{\perp}$ |

(B33)

| $H'_{\perp}$ | $\lvert\mu_8\rangle$ | $\lvert\mu_9\rangle$ | $\lvert\mu_{10}\rangle$ | $\lvert\mu_{11}\rangle$ | $\lvert\mu_{12}\rangle$ | $\lvert\mu_{13}\rangle$ | $\lvert\mu_{14}\rangle$ |
|---|---|---|---|---|---|---|---|
| $\langle\mu_8\rvert$ | $-\frac{3}{4}J_{\parallel}$ | | | | | | |
| $\langle\mu_9\rvert$ | 0 | $-\frac{3}{4}J_{\parallel}$ | | | | | |
| $\langle\mu_{10}\rvert$ | 0 | $3h_{\perp}$ | $\frac{3}{4}J_{\parallel}$ | | | | |
| $\langle\mu_{11}\rvert$ | 0 | 0 | 0 | $\frac{3}{4}J_{\parallel}$ | | | |
| $\langle\mu_{12}\rvert$ | $-4J_{\perp}$ | 0 | 0 | $3h_{\perp}$ | $-\frac{3}{4}J_{\parallel}$ | | |
| $\langle\mu_{13}\rvert$ | 0 | 0 | $2\sqrt{2}\,h_{\perp}$ | 0 | 0 | $\frac{9}{4}J_{\parallel}$ | |
| $\langle\mu_{14}\rvert$ | 0 | 0 | 0 | $2\sqrt{2}\,h_{\perp}$ | 0 | 0 | $\frac{9}{4}J_{\parallel}$ |

(B33)

where $a = 12\,\frac{h_{\perp}^2}{N_3}$ , $q = 12\,\frac{h_{\perp}^2}{N_2}$ (B34)

$$b = \frac{h_{\perp}}{N_2}(18J_{\perp}-2B) \tag{B35}$$

$$c = \frac{h_{\perp}}{N_3}(18J_{\perp}-2K) \tag{B36}$$

$$d = -\frac{2\sqrt{2}\,BJ_{\perp}}{N_2} \tag{B37}$$

$$e = -\frac{2\sqrt{2}\,KJ_{\perp}}{N_3} \tag{B38}$$

$$j = 2\sqrt{2}\,J_{\perp} \tag{B39}$$

and B, K, $N_2$, $N_3$ are defined in Chapter V. Now, using equations B28 and B32 with the matrix elements just given, the resulting energies to third-order in the energy shifts are:

$$E_o^{(3)} = \frac{D_c}{2} + \frac{J_{||}}{4} + \frac{9J_\perp}{2} - \frac{4J_\perp^2}{D_c} + \frac{9}{4}\cdot\frac{J_{||}J_\perp^2}{D_c^2} - 8\cdot\frac{h_\perp^2}{D_c} \tag{B40}$$

$$E_1^{(3)} = \frac{D_c}{2} - \frac{9J_\perp}{4} - \frac{A}{2} - 2\cdot\frac{(18J_\perp - 2K)^2}{D_c}\cdot\left(\frac{h_\perp}{N_3}\right)^2 - 4\frac{J_\perp^2}{D_c}\cdot\left(\frac{K}{N_3}\right)^2 + (3/4)J_{||}[(18J_\perp - K)/D_c]^2(h_\perp/N_3)^2 \tag{B41}$$

$$E_2^{(3)} = \frac{D_c}{2} - \frac{J_{||}}{4} - \frac{18J_\perp^2}{D_c} + \frac{27}{4}\cdot\frac{J_\perp^2 J_{||}}{D_c^2} - 8\cdot\frac{h_\perp^2}{D_c} \tag{B42}$$

$$E_3^{(3)} = \frac{D_c}{2} - \frac{9J_\perp}{4} + \frac{A}{2} - 4\cdot\left(\frac{B}{N_2}\right)^2\cdot\frac{J_\perp^2}{D_c} + \frac{9}{4}\cdot\left(\frac{B}{N_2}\right)^2\cdot\frac{J_{||}J_\perp^2}{D_c^2} - 2\cdot\frac{(18J_\perp - 2B)^2}{D_c}\cdot\left(\frac{h_\perp}{N_2}\right)^2 \tag{B43}$$

where all terms of order $\left(\frac{h_\perp}{D_c}\right)^2$ and higher have been omitted. For comparison to the zero-field energy levels it is convenient to evaluate the following limits:

$$\lim_{h_\perp \to o} \frac{B}{N_2} = 1 \quad , \quad \lim_{h_\perp \to o} N_2 = \frac{J_{||} - 9J_\perp}{2} \quad , \quad \lim_{h_\perp \to o} B = \frac{J_{||} - 9J_\perp}{2} \tag{B44}$$

$$\lim_{h_\perp \to o} \frac{K}{N_3} = 0 \quad , \quad \lim_{h_\perp \to o} K = 0 \quad , \quad \lim_{h_\perp \to o} N_3 = 0 \tag{B45}$$

$$\lim_{h_\perp \to o} \frac{h_\perp}{N_3} = \frac{1}{6} \quad , \quad \lim_{h_\perp \to o} A = \frac{J_{||} - 9J_\perp}{2} \tag{B46}$$

To evaluate the small-field partition function and then the zero-field susceptibility, only the terms linear in $h_\perp$ need be kept. Thus, the small-field energy levels now become:

$$E_o = \frac{D_c}{2} + \frac{J_{||}}{4} + \frac{9J_{\perp}}{2} - \frac{4J_{\perp}^2}{D_c} + \frac{9}{4}\frac{J_{||}J_{\perp}^2}{D_c^2} \tag{B47}$$

$$E_1 = \frac{D_c}{2} - \frac{9J_{\perp}}{4} - \frac{A}{2} - 18\frac{J_{\perp}^2}{D_c} + \frac{27}{4}\frac{J_{||}J_{\perp}^2}{D_c^2} \tag{B48}$$

$$E_2 = \frac{D_c}{2} - \frac{J_{||}}{4} - 18\frac{J_{\perp}^2}{D_c} + \frac{27}{4}\frac{J_{||}J_{\perp}^2}{D_c^2} \tag{B49}$$

$$E_3 = \frac{D_c}{2} - \frac{9J_{\perp}}{4} + \frac{A}{2} - 4\frac{J_{\perp}^2}{D_c} + \frac{9}{4}\frac{J_{||}J_{\perp}^2}{D_c^2} \tag{B50}$$

where the field dependence is contained within $A$ as seen from equation B22.